ABSTRACT

Title of Dissertation: COMPREHENSIVE ELECTRICAL/OPTICAL/THERMAL CHARACTERIZATIONS OF HIGH POWER LIGHT EMITTING DIODES AND LASER DIODES

Dae-Suk Kim, Doctor of Philosophy, 2016

Dissertation directed by: Professor Bongtae Han
Department of Mechanical Engineering

Thermal characterizations of high power light emitting diodes (LEDs) and laser diodes (LDs) are one of the most critical issues to achieve optimal performance such as center wavelength, spectrum, power efficiency, and reliability. Unique electrical/optical/thermal characterizations are proposed to analyze the complex thermal issues of high power LEDs and LDs.

First, an advanced inverse approach, based on the transient junction temperature behavior, is proposed and implemented to quantify the resistance of the die-attach thermal interface (DTI) in high power LEDs. A hybrid analytical/numerical model is utilized to determine an approximate transient junction temperature behavior, which is governed predominantly by the resistance of the DTI. Then, an accurate value of the

resistance of the DTI is determined inversely from the experimental data over the predetermined transient time domain using numerical modeling.

Secondly, the effect of junction temperature on heat dissipation of high power LEDs is investigated. The theoretical aspect of junction temperature dependency of two major parameters – the forward voltage and the radiant flux – on heat dissipation is reviewed. Actual measurements of the heat dissipation over a wide range of junction temperatures are followed to quantify the effect of the parameters using commercially available LEDs. An empirical model of heat dissipation is proposed for applications in practice.

Finally, a hybrid experimental/numerical method is proposed to predict the junction temperature distribution of a high power LD bar. A commercial water-cooled LD bar is used to present the proposed method. A unique experimental setup is developed and implemented to measure the average junction temperatures of the LD bar. After measuring the heat dissipation of the LD bar, the effective heat transfer coefficient of the cooling system is determined inversely. The characterized properties are used to predict the junction temperature distribution over the LD bar under high operating currents. The results are presented in conjunction with the wall-plug efficiency and the center wavelength shift.

COMPREHENSIVE ELECTRICAL/OPTICAL/THERMAL CHARACTERIZATIONS OF HIGH POWER LIGHT EMITTING DIODES AND LASER DIODES

By

Dae-Suk Kim

Dissertation submitted to the Faculty of the Graduate School of the
University of Maryland, College Park, in partial fulfillment
of the requirements for the degree of
Doctor of Philosophy
2016

Advisory Committee:
Professor Bongtae Han, Chair/Advisor
Professor Avram Bar-Cohen
Professor F. Patrick McCluskey
Research Professor Yunho Hwang
Professor Mario Dagenais, Dean's Representative

© Copyright by
Dae-Suk Kim
2016

Dedication

This dissertation is dedicated to my parents, my parents-in-law, Dae Jung, Areum, Sujin, Jiwon for their support and sacrifice.

Acknowledgements

First and foremost, I would like to express my sincere gratitude to my advisor, Prof. Bongtae Han, for his support, patience, guidance, and invaluable advice in both personal and professional matters. He was the best advisor and mentor in my life, and it was a blessing to be able to learn from him. I strongly believe that his teachings will stay with me for the rest of my life and will influence my future professional career in a positive way. It was my honor to have Prof. Bar-Cohen, Prof. McCluskey, Prof. Hwang, and Prof. Dagenais as my committee members, and I gratefully acknowledge their critical comments in the completion of this dissertation.

I have been incredibly fortunate to work with amazing LOMSS members: Dr. Song, Dr. Oh, Yejin, David, Stephen, Kenny, Yong, Bulong, Hsiu-Ping, Hyun-Seop, and Byung Yub. I appreciate all of your support and help. I am also especially grateful to Dr. Gromala in BOSCH for giving me the wonderful project and internship opportunity. My wife and I will never forget the wonderful time spent in Germany. Furthermore, I thank the Korean students in the mechanical engineering department for their support and encouragement. I also like to gratefully acknowledge the prayers and encouragement sent from my Bible study group friends.

Finally, my family. All of this could not have been possible without the unconditional support, trust, and love from my parents and my parents-in-law. I am also grateful to Dae Jung and Areum for your support and encouragement. I am sincerely grateful to my dear wife, Jiwon, and my daughter, Sujin, for your sacrifice, support, and love. I love you all dearly.

Table of Contents

List of Tables vi

List of Figures vii

List of Symbols x

Chapter 1: Introduction 1

1.1. Motivations and Objectives 1

1.1.1. Characterization of Die-Attach Thermal Interface of High Power LEDs 2

1.1.2. Investigation of Junction Temperature Effect on Heat Dissipation of High Power LEDs 3

1.1.3. Prediction of Junction Temperature Distribution of High Power LD Bar 4

1.2. Organization of Dissertation 5

Chapter 2: Characterization of Die-Attach Thermal Interface of High Power Light Emitting Diodes: An Inverse Approach 7

2.1. Introduction 7

2.2. Transient Behavior of LED Junction Temperature 9

2.2.1. Transient Voltage Behavior of LED 9

2.2.2. Measurement of Transient LED Junction Temperature 11

2.3. Transient Domain for Inverse Approach 18

2.3.1. Hybrid Analytical/Numerical Model 18

2.3.2. DTI Dominant Domain 23

2.4. Inverse Approach to Determine the Resistance of DTI 27

2.5. Validity of DTI Resistance 29

2.6. Conclusion 33

Chapter 3: Effect of Junction Temperature on Heat Dissipation of High Power Light Emitting Diodes 34

3.1. Introduction 34

3.2. Background: Junction Temperature Dependent Forward Voltage and Radiant Flux 35

3.2.1. Forward Voltage 36

3.2.2. Radiant Flux ... 37
3.3. Measurement of Heat Dissipation ... 39
3.3.1. Specimen and Test Procedure ... 39
3.3.2. Junction Temperature Measurement ... 41
3.3.3. Heat Dissipation Measurement ... 46
3.4. Junction Temperature Dependency ... 52
3.5. Empirical Heat Dissipation Model ... 55
3.5.1. Practical Consideration ... 56
3.5.2. Empirical Model ... 59
3.6. Conclusion ... 61

Chapter 4: Hybrid Experimental/Numerical Method to Predict Junction Temperature Distribution of High Power Laser Diode Bar ... 62
4.1. Introduction ... 62
4.2. Laser Diode System ... 63
4.2.1. LD Bar Description ... 63
4.2.2. Calibration Curve ... 66
4.2.3. Electrical Resistance of Single Emitter ... 68
4.3. Junction Temperature Measurement ... 69
4.3.1. Test Setup ... 70
4.3.2. Average Junction Temperature ... 71
4.3.3. Average Junction Temperature Measurement ... 74
4.4. Heat Dissipation and Microcooler Effective heat transfer Coefficient 79
4.4.1. Measurement of Heat Dissipation ... 79
4.4.2. Effective Heat Transfer Coefficient ... 81
4.5. Numerical Prediction of Junction Temperature Distribution ... 83
4.5.1. Temperature Distribution in LD Bar ... 84
4.5.2. Wall-plug Efficiency and Center Wavelength Shift ... 88
4.6. Conclusions ... 90

Chapter 5: Contributions and Future Works ... 92
5.1. Thesis Contributions ... 92
5.2. Future Works ... 93

Reference ... 95

List of Tables

Table 2.1. Experimental data of blue LED using the AuSn Solder die-attach 17

Table 2.2. Material properties used in the numerical model and the analytical solution [71-76] 22

Table 2.3. Thermal resistance, thermal capacitance, and time constant used in the hybrid analytical numerical solution 23

Table 2.4. Experimental data of blue LED using the AuSn Solder and Ag paste die-attach 32

Table 4.1. Junction temperature error at different probe currents 68

Table 4.2. Material properties, thickness, and calculated time constant used in the analytical solution [100, 101] 78

Table 4.3. Average junction temperature and thermal resistance estimations at different forward currents at 20 °C of the inlet water temperature 81

Table 4.4. Heat dissipation at 80A under different inlet water temperatures 84

List of Figures

Figure 2.1. Schematicillustration of (1) the RC delay, (2) the thermal delay, and (3) the combined behavior of the forward voltage from the high operating current to the low probe current 10

Figure 2.2. Schematic illustration of the measurement setup 11

Figure 2.3. Cross-section image of the high power blue LED 12

Figure 2.4. SEM image of the epitaxial layer, the die-attach, and the LED package. 13

Figure 2.5. Calibration curve of the blue LED 14

Figure 2.6. Transient voltage behaviors under four different operating currents in (a) the total history and (b) the zoomed-in view.. 15

Figure 2.7. SPDs under the different operating currents at T_j^{Ap}= 75 °C 16

Figure 2.8. Transient junction temperature behavior at T_j^{Ap}= 75 °C 17

Figure 2.9. Schematic illustration of the hybrid analytical/numerical model............. 19

Figure 2.10. (a) 3D model and (b) temperature distribution at the steady state 21

Figure 2.11. Transient behavior of ΔT for (a) 30,000 ms in the log scale and for (b) 3 ms in the linear scale 24

Figure 2.12. Normalized transient behavior of ΔT under the different thermal resistance of (a) second layer and (b) third layer 26

Figure 2.13. Temperature distribution at (a) 0 ms and (b) 2 ms 27

Figure 2.14. Experimental data is compared with numerical prediction after the iteration.. 29

Figure 2.15. Predicted transient behavior of AuSn die-attach at different forward currents is compared with experimental data, where the DTI resistance obtained from Figure 2.14 is used in the numerical simulation. 30

Figure 2.16. Cross-section image of the AuSn die-attach layer at (a) 200X and (b) 1000X magnification.. 31

Figure 2.17. Predicted transient behavior of AuSn and Ag paste die-attach at different forward currents is compared with experimental data, where the DTI

resistance obtained from the 1000 mA case is used in the numerical simulation 32

Figure 3.1. Relative radiant flux changes as a function of temperature at the characteristic temperatures of 79 K and 1639 K 39

Figure 3.2. Cross-section image of a high power blue LED 40

Figure 3.3. Schematic illustration of the measurement setup 41

Figure 3.4. Calibration curve of LED1 and LED2 42

Figure 3.5. (a) Transient voltage behavior of LED1 after the probe current is applied and (b) enlarged view of the region marked by a dashed box 44

Figure 3.6. Junction temperatures obtained from the voltage of Zone 3 is plotted in the square root time scale; the linear extrapolation provides the estimated junction temperature at the operating current 45

Figure 3.7. SPDs of LED1 at the forward current of (a) 250 mA and (b) 1000 mA 47

Figure 3.8. SPDs of LED2 at the forward current of (a) 250 mA and (b) 1000 mA 48

Figure 3.9. Radiant fluxes as a function of junction temperature 49

Figure 3.10. Forward voltage as a function of junction temperature 50

Figure 3.11. Heat dissipations as a function of junction temperature at (a) 250 mA and (b) 1000 mA 51

Figure 3.12. Percent changes of (a) electrical input powers, (b) optical output powers, and (c) heat dissipations as a function of junction temperature 54

Figure 3.13. Power efficiency as a function of junction temperature 55

Figure 3.14. Heat dissipation of (a) CW-LED3 and (b) WW-LED4 as a function of junction temperature 58

Figure 3.15. (a) Heat dissipation of CW-LED3 and WW-LED4 predicted by the empirical model and (b) difference between predicted values and measured values 60

Figure 4.1. (a) LD bar with water-cooled microchannel [102] and (b) side view of the LD bar 65

Figure 4.2. Forward voltage as a function of junction temperature 67

Figure 4.3. Electrical resistance of the single emitter as a function of junction temperature at $I_{probe} = 120$ mA... 69

Figure 4.4. Schematic illustration of junction temperature measurement setup......... 71

Figure 4.5. Deviation of the measured junction temperature of LD bar from the average junction temperature of LD bar with a linearly changing temperature of ΔT from the edge to the center.. 73

Figure 4.6. Transient voltage behavior of the LD bar obtained after blocking the operating current of 80 A 74

Figure 4.7. (a) Enlarged view of the region marked by a dashed box in Figure 4.6 and (b) Average junction temperature in the square root time scale; the linear extrapolation provides the estimated average junction temperature at the operating current 77

Figure 4.8. Average junction temperature at different forward currents 78

Figure 4.9. (a) Forward voltage and (b) electrical input power, radiant flux, and heat dissipation as a function of forward currents 80

Figure 4.10. 3D model 82

Figure 4.11. Temperature distribution of the LD bar at (a) 80 A and (b) 160 A 86

Figure 4.12. Average junction temperature of each emitter 87

Figure 4.13. Junction temperature variations along the emitter................................. 88

Figure 4.14. Normalized SPD at 160 A [102] 89

List of Symbols

Symbol	Explanation	Unit
A	cross-section area	m^2
A_e	Shockley-Read-Hall	s^{-1}
A_f	variable for an exponential function	-
B_e	radiative coefficients	m^3/s
B_f	variable for an exponential function	-
c_p	specific heat	J/(kg·K)
C	electrical capacitance	F
C_e	Auger coefficients	m^6/s
C_s	combined temperature independent parameter	-
C_{th}	thermal capacitance	J/K
d	thickness along a heat transfer direction	m
e	elementary charge	C
$E_{g,300}$	bandgap at 300 K	eV
k	Boltzmann constant	J/K
K_s	thermal conductivity	W/(m·K)
I_f	forward current	A
I_{probe}	probe current	A
n	carrier concentration	m^{-3}
n_{ideal}	diode ideality factor	-
N	number of the emitter	-
N_A	acceptor concentrations	m^{-3}
N_C	effective density of states at the conduction band	m^{-3}
N_D	donor concentrations	m^{-3}
N_V	effective density of states at the valence band edges	m^{-3}
P_e	electrical input power	W
P_h	heat dissipation	W
P_o	optical output power	W
ppm	parts per million	-
R	electrical resistance	Ω

R^2	coefficient of determination	-
R_{th}	thermal resistance	K/W
$R(T_j^{ave})$	electrical resistance at an average junction temperature of a laser diode bar	Ω
t	time	s
T_{center}	average temperature in a center emitter	°C
T_{ch}	characteristic temperature	K
T_{edge}	average temperature in an edge emitter	°C
T_{inlet}	inlet water temperature	°C
T_j	junction temperature	°C
T_j^{ave}	average junction temperature of a laser diode bar	°C
T_j^{Ap}	apparent junction temperature	°C
T_{ref}	reference temperature	K
T_s	surface temperature of a thermoelectric cooler	°C
V_f	forward voltage	V
V_f^{ave}	forward voltage at an average junction temperature of a laser diode bar	V
$V_f^{measured}$	measured forward voltage of a laser diode bar	V
α	thermal diffusivity	m^2/s
α_V	Varshni parameter	eV/K
α'	fitting parameters for bad gap energy	eV/K
β_V	Varshni parameter	K
δT_j	deviation of a measured junction temperature from an average junction temperature of a laser diode bar	°C
ΔT	temperature differences	°C
η_{ext}	external quantum efficiency	%
$\eta_{extraction}$	extraction efficiency	%
η_i	internal quantum efficiency	%
η_p	power efficiency	%
ρ	volumetric mass density	kg/m^3
τ_{th}	thermal time constant	s
Φ	radiant flux	W

Chapter 1: Introduction

1.1. Motivations and Objectives

Direct band gap materials, which emit photons by recombination of electrons and holes, have been used for high power light emitting diodes (LEDs) and laser diodes (LDs) [1]. High power LEDs have emerged as a new and revolutionary general light source as they surpass conventional light sources in terms of energy efficiency, lifetime, and light quality [1-4]. High power LDs have been accepted as the most promising pumping sources for solid state lasers and fiber lasers and for a variety of applications in communication, cosmetic and medical applications, material surface treatment, joining technologies, cutting technologies, and defense applications [5-11].

Thermal performance of high power LEDs and LDs affects center wavelength, spectrum, power efficiency, and reliability [12-19]. Thus, thermal analyses are critical to the design of packaging as well as the diode itself.

Unlike other heat generation sources, unique electrical/optical/thermal characterizations are required for the thermal analyses of the high power LEDs and LDs. This dissertation investigates three complex thermal issues by understanding the unique characteristics of high power LEDs and LDs. The motivation for and objective of each issue are described in the following section.

1.1.1. Characterization of Die-Attach Thermal Interface of High Power LEDs

A die-attach layer often creates the most significant resistance to the flow of heat from the junction to the heat spreader in high power LEDs [20-23]. Thus, characterization of the die-attach thermal interface (DTI) in high power LEDs is one of the most important tasks for assessing performance range and reliability.

The thermal resistance of the die-attach layer is governed by the bond line thickness (BLT), the thermal conductivity of the die-attach material, and the contact resistance at the die-attach interfaces [24]. In addition, the existence of undesired but inevitable voids created by the die bonding processes serves to increase the thermal resistance between the die and the substrate, and thus gives rise to a further junction temperature increase [25-29].

It is well known that interfacial thermal resistance can be evaluated using the transient behavior of the device junction temperature, which can be expressed analytically using a model based on the thermal resistance and the thermal capacitance by proceeding carefully through a series of empirical steps (called a differential structural function) [14, 20, 21, 30-35]. This approach does not require the thermal properties of the materials used in the device, which is a very attractive advantage in practice. Yet, the mathematically complex process used in this approach (i.e., differentiation and deconvolution) can lead to considerable measurement uncertainties, especially for the thermal resistance of the die-attach layers [36]. Moreover, it is worth noting that the lateral heat spreading resistance in a high power LED is significant, and not easily captured by a 1-D model, as used in this approach [37, 38].

The first objective is, thus, to propose and implement an advanced inverse approach to more accurately determine the effective DTI resistance of high power LEDs.

1.1.2. Investigation of Junction Temperature Effect on Heat Dissipation of High Power LEDs

The heat dissipation of the high power LEDs is one of the most critical parameters for analytical, experimental, and/or numerical analyses [39-43]. The heat dissipation of an LED operated at a given forward current can be calculated by subtracting the optical output power from the electrical input power [44]. The electrical input power is the product of the forward current and the forward voltage. The optical output power is the radiant flux.

The electrical input power, the optical output power, and the heat dissipation are altered by the junction temperature. It has been well-known that the forward voltage decreases as the junction temperature increases because of the reduction of band gap energy at higher junction temperatures [4, 45-47]. Consequently, the electrical input power will decrease as the junction temperature increases, which helps reduce the heat dissipation.

It has also been well-known that the radiant flux decreases as the junction temperature increases because the non-radiative recombination increases with higher junction temperatures [48, 49]. As a result, the optical output power will also decrease as the junction temperature increases, which gives rise to the heat dissipation. The net

results of this opposite effect on the final heat dissipation have not been clearly understood.

The second objective is, thus, to investigate quantitatively the effect of junction temperature on heat dissipation.

1.1.3. Prediction of Junction Temperature Distribution of High Power LD Bar

A junction temperature of a high power LD is one of the most important parameters to achieve optimal performance such as center wavelength, spectrum, wall-plug efficiency, and reliability [15-19]. The junction temperature measurement is critical for the diode itself as well as the packaging design.

As higher optical power is demanded for advanced applications, more closely-spaced emitters with higher forward current are used in LD bars. As a result, the junction temperatures of adjacent emitters may have large variations, which can lead to different center wavelength and wall-plug efficiency of each emitter, and result in low pumping efficiency and reliability, respectively.

Several junction temperature measurement methods for low power LDs or LEDs have been proposed; they include thermal resistance [50], wavelength-shift [51, 52], optical power output [51], and forward-voltage method [46, 47, 51, 53-58]. These methods are applicable only when the junction temperature is uniform. The micro-Raman spectroscopy [59-61] can be used to measure the junction temperature distribution by measuring multiple local temperatures. However, it has limited

accuracy and requires a complicated experimental setup [59-61]. As a result, it is challenging to measure the junction temperature distribution of the high power LD bar using the existing methods.

The third objective is, thus, to propose a hybrid experimental/numerical method to predict the junction temperature distribution of the high power LD bar.

1.2. Organization of Dissertation

This first chapter describes the motivations and three main objectives of the dissertation. These three objectives are addressed in the subsequent chapters.

Chapter 2 presents the inverse approach to characterize the DTI of the high power LEDs. The transient junction temperature behavior of an LED is first measured by the well-known forward voltage method [31, 62-64]. Then, the transient time domain governed predominantly by the resistance of the DTI is selected using a hybrid analytical/numerical solution. An accurate value of the DTI resistance is determined inversely from the experimental data using numerical modeling. Supplementary experiments are conducted at various forward currents to verify the validity of the proposed method. The validity is further confirmed by measuring the actual voids in the die-attach layer. This chapter has been published in the *IEEE Transactions on Components, Packaging, and Manufacturing Technology* [65].

Chapter 3 is devoted to investigating the effect of junction temperature on heat dissipation. The theoretical aspect of junction temperature dependency of two major parameters – the forward voltage and the radian flux – is reviewed first. Actual

measurements of heat dissipation over a wide range of the junction temperatures are followed to quantify the opposite effect of the two parameters using commercially available LEDs. An empirical model of heat dissipation is proposed for applications in practice. The results are presented and the practical implications are discussed. This chapter has been published in the *Journal of Applied Physics* [66].

Chapter 4 focuses on the hybrid experimental/numerical method to predict the junction temperature distribution of the high power LD bar. A commercial water-cooled LD bar with multiple emitters is investigated to present the proposed method. After introducing the LD bar system, an experimental setup that is developed uniquely to measure the average junction temperatures of the LD bar is described. Two parameters critical to thermal analysis – heat dissipation and effective heat transfer coefficient – are determined and subsequently used to predict the junction temperature distribution over the LD bar under high operating currents. This chapter has been prepared to be submitted as a journal paper.

Chapter 5 contains a summary of the contributions and a discussion of future works that can be extended from this work.

Chapter 2: Characterization of Die-Attach Thermal Interface of High Power Light Emitting Diodes: An Inverse Approach

2.1. Introduction

Under a given operating current, the light output as well as the lifetime of high power LEDs decreases as the junction temperature increases [12-14]. A die-attach layer often creates the most significant resistance to the flow of heat from the junction to the heat spreader in high power LEDs [20-23]. Thus, characterization of the die-attach thermal interface (DTI) in high power LEDs is one of the most important tasks for assessing performance range and reliability.

The thermal resistance of the die-attach layer is governed by the bond line thickness (BLT), the thermal conductivity of the die-attach material, and the contact resistance at the die-attach interfaces [24]. In addition, the existence of undesired but inevitable voids created by the die bonding processes serves to increase the thermal resistance between the die and the substrate, and thus gives rise to a further junction temperature increase [25-29].

It is well known that interfacial thermal resistance can be evaluated using the transient behavior of the device junction temperature [14, 20, 21, 30-35], which can be expressed analytically using a model based on the thermal resistance and the thermal capacitance by proceeding carefully through a series of empirical steps. In the approach, the transient junction thermal behavior is determined first from the forward

voltage measured during the transient period [31, 62-64]. Next, the thermal impedance curve is obtained by dividing the transient junction temperature change by the heat dissipation. The spectral distribution of the observed thermal time constants is, then, extracted from the thermal impedance curve by numerical differentiation and deconvolution. As a next step, the LED structural function is obtained from the one-dimensional Cauer network, by discretizing the time constant spectrum into 100-200 peaks [34], and the thermal capacitance is calculated by dividing the thermal resistance from the time constants at each peak. The sum of the thermal capacitances can then be plotted as a function of the sum of the thermal resistances, which is the cumulative structure function, and the interfacial thermal resistance can be determined from the differential structural function.

Commercial equipment utilizing this principle is available and has been actively used to compare relative changes of the thermal resistance produced by different die-attach materials and/or thicknesses [20, 32, 67]. This approach does not require the thermal properties of the materials used in the device, which is a very attractive advantage in practice. Yet, the mathematically complex process used in this approach (i.e., differentiation and deconvolution) can lead to considerable measurement uncertainties, especially for the thermal resistance of the die-attach layers [36]. Moreover, it is worth noting that the lateral heat spreading resistance in a high power LED is significant, and not easily captured by a 1-D model, as used in this approach [37, 38].

In this chapter, an advanced inverse approach is proposed and implemented to more accurately determine the effective DTI resistance of high power LEDs. A hybrid

analytical/numerical model is first used to determine the approximate transient junction temperature behavior, which is governed predominantly by the resistance of the DTI. Then, a more accurate value of the DTI resistance is determined inversely from the experimental data using numerical modeling.

2.2. Transient Behavior of LED Junction Temperature

The junction temperature of an LED can be measured by the well-known forward voltage method [31, 62-64]. The method is based on the theory that the forward voltage of a semiconductor device has a negative linear relationship with the junction temperature. This negative linear relationship (called a calibration curve) is obtained at a very low probe current to avoid any undesired junction temperature increase while obtaining the calibration curve. In the actual measurements, the probe current is suddenly applied after an LED reaches the steady state condition under high operating currents. This section is devoted to describing the unique transient behavior of a high power LED during the application of the probe current.

2.2.1. Transient Voltage Behavior of LED

During the transition period (when the forward current changes from the high operating current to the low probe current), the forward voltage, V_f, shows the combined behavior of "diode delay" and "thermal delay". This is illustrated schematically in Figure 2.1. When the probe current is applied, the ideal diode voltage shows a behavior known as the "RC delay" due to the resistance of an LED and the

capacitance of a current source (the blue dotted line (1)). At the same time, the junction temperature starts to decrease due to the small probe current. This gradual reduction of the junction temperature causes the voltage to increase since the junction temperature has the negative linear relationship with the forward voltage (the red dotted line (2)).

In actual voltage measurements, the combined effect is observed (the black line (3)). The forward voltage decreases first but starts to increase after the thermal effect overrides the RC delay effect. After the RC delay effect diminishes, the voltage represents the thermal behavior only and it can be used to measure the resistance of the DTI.

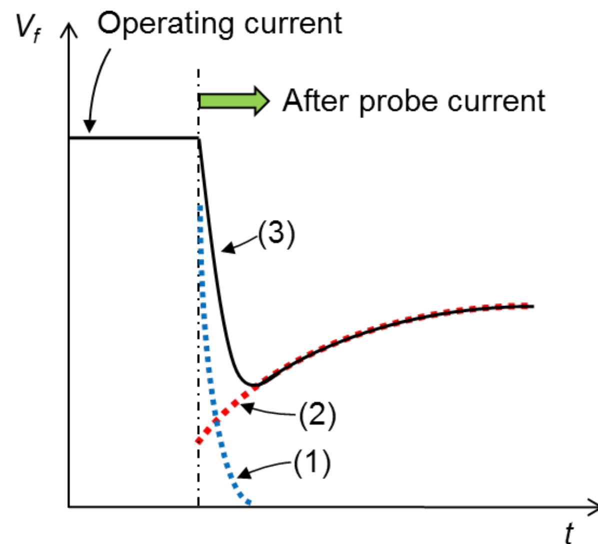

Figure 2.1. Schematicillustration of (1) the RC delay, (2) the thermal delay, and (3) the combined behavior of the forward voltage from the high operating current to the low probe current

2.2.2. Measurement of Transient LED Junction Temperature

Figure 2.2 shows the schematic illustration of a measurement setup. The junction temperature of the LED was controlled by a high power thermoelectric cooler (TEC) (LB320: Silicon Thermal), which had a temperature control resolution of ±0.1 °C. When a desired junction temperature was reached, the spectral power distribution (SPD) was measured by an integrating sphere equipped with a spectrometer (SMS–500: SphereOptics). The LED was operated by a sourcemeter (2401: Keithley Instruments). A data acquisition (DAQ) module (USB-6212: National Instruments) measured the forward voltage of the LED at the resolution of 16-bits. In order to control the TEC, the source meter, and the DAQ simultaneously, the control routines were integrated by a LabVIEW program.

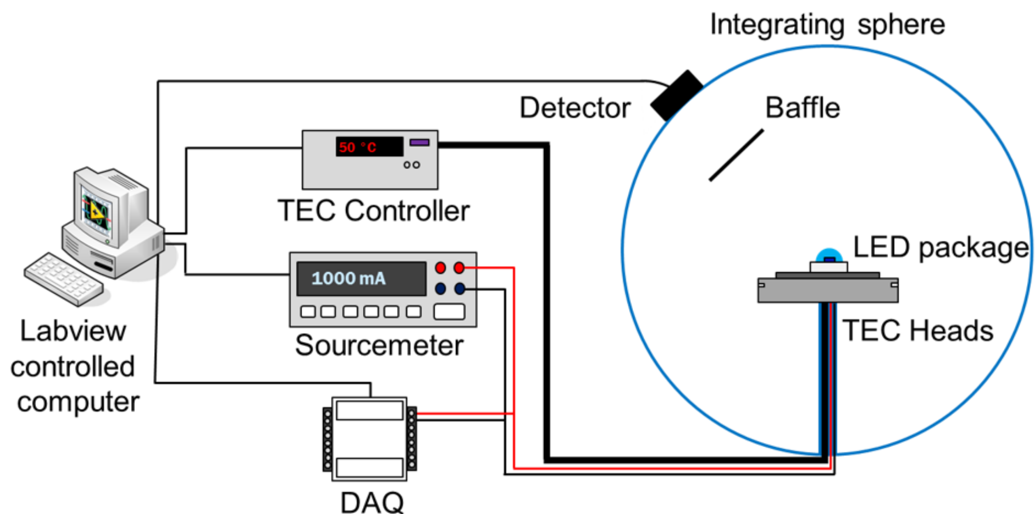

Figure 2.2. Schematic illustration of the measurement setup

A cross-section image of a high power blue LED tested in the study is shown in Figure 2.3. It is a typical high power LED with a DTI for lighting applications, which has a total thermal resistance of 10 K/W. The high power blue LED chip is mounted on a ceramic substrate to form a package, which is subsequently mounted on a metal core printed circuit board (MCPCB) using solder connections. Figure 2.4 also shows the SEM picture of a region marked by a dashed ellipse in Figure 2.3, containing the epitaxial layer, the die-attach, and the ceramic substrate. There is virtually no defect in the epitaxial layer, but many voids appear in the interfacial region between the silicon substrate and the die-attach.

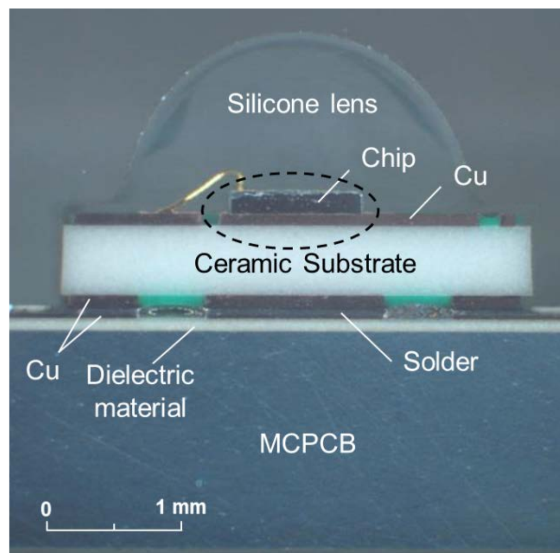

Figure 2.3. Cross-section image of the high power blue LED

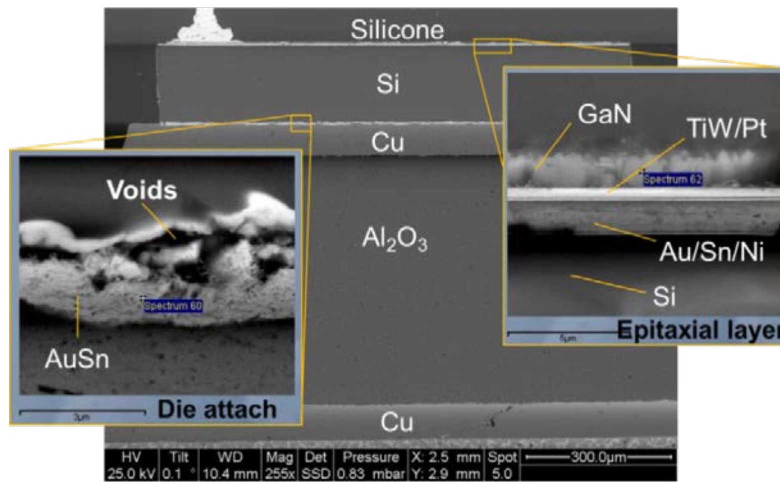

Figure 2.4. SEM image of the epitaxial layer, the die-attach, and the LED package

The calibration curve was obtained by measuring the forward voltage under a low injection current of 10 mA, which showed the highest R^2 value (0.999), at different temperatures. The low current was applied only for 10 ms to ensure that the effect of the heat generated by the current on the junction temperature was negligible. The results are shown in Figure 2.5, from which the slope and the y-intercept were determined to be −1.36 mV/K and 2.6559 V, respectively, which is close to the theoretical slope of GaN (−1.7 mV/K) [62].

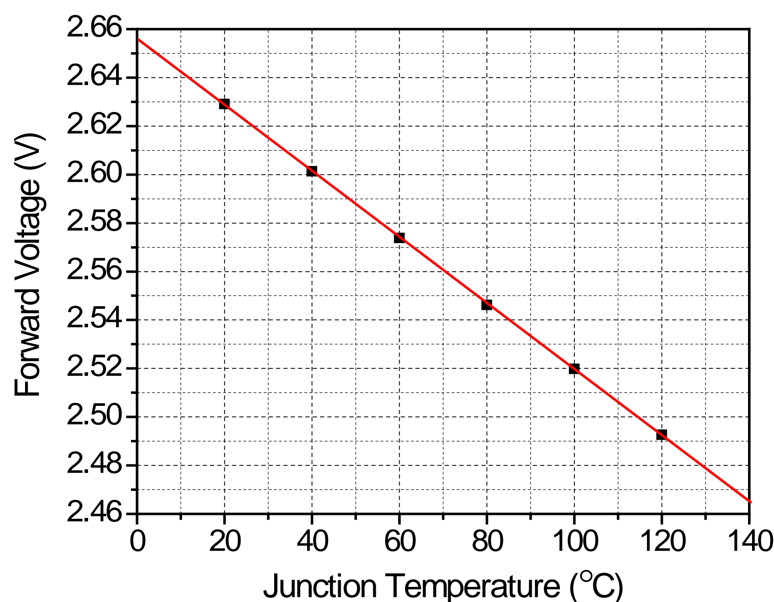

Figure 2.5. Calibration curve of the blue LED

The transient voltage behavior, under four different operating currents, is shown in Figure 2.6. The TEC was controlled to produce the same minimum voltage value (2.5539 V) for all four operating currents, which corresponded to 75°C in the calibration curve. This temperature will be referred to as the "apparent junction temperature (T_j^{Ap})". The well-known Savitzky-Golay smoothing filter was employed to reduce the random noise of the experimental data. The experimental data have repeatability within 0.14 mV (corresponding to 0.1 °C). The total history is shown in Figure 2.6a and the zoomed-in view containing the minimum voltage is shown in Figure 2.6b.

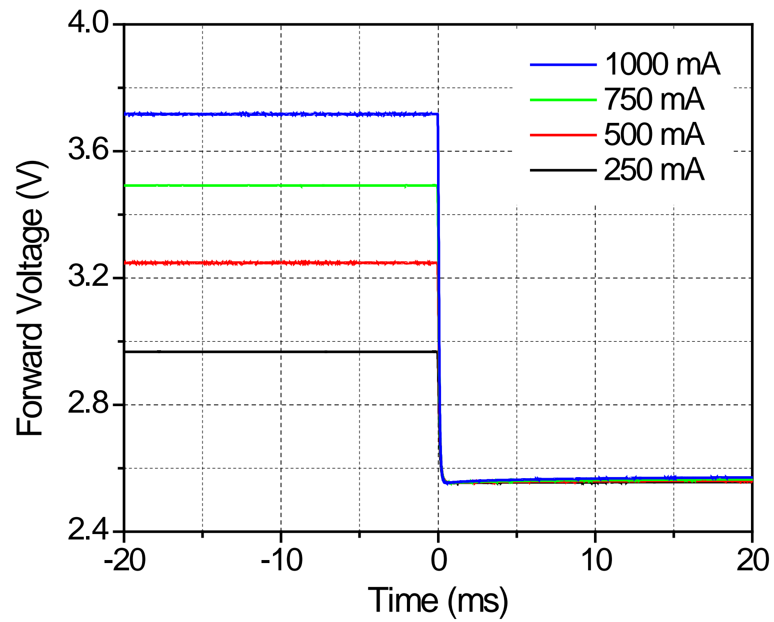

(a)

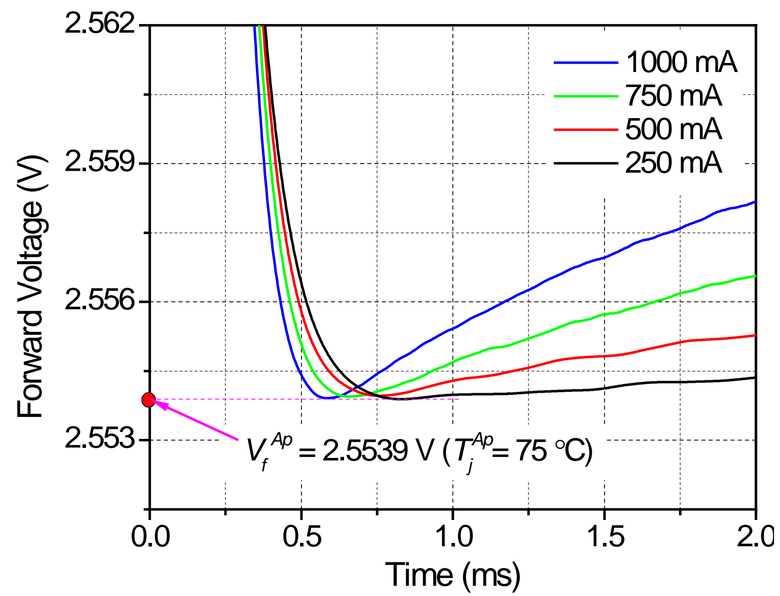

(b)

Figure 2.6. Transient voltage behaviors under four different operating currents in (a) the total history and (b) the zoomed-in view

The heat dissipation at each current can be determined from the following equation:

$$P_h = I_f V_f - \Phi \tag{1}$$

where P_h is the heat dissipation [W], I_f is the forward current [A], V_f is the forward voltage [V], and Φ is the radiant flux [W] [68]. Equation (1) requires the forward voltage and current, as well as radiated light power, to yield the heat dissipation at each current.

The SPDs obtained at the four operating currents are shown in Figure 2.7. The emitted light power was determined from the SPDs and it was subtracted from the total electrical power to calculate the heat dissipation. The electrical power, the radiant flux, the heat dissipation, and the surface temperature of the TEC (T_s) are summarized in Table 2.1.

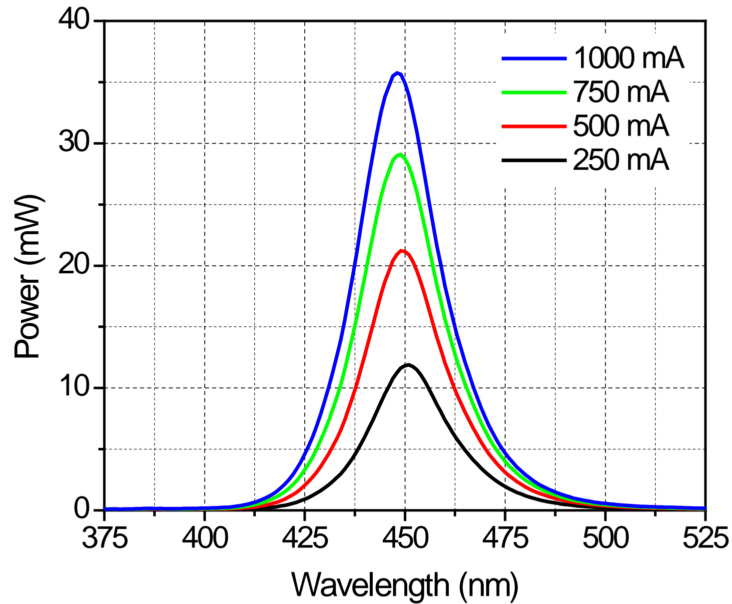

Figure 2.7. SPDs under the different operating currents at T_j^{Ap}= 75 °C

Table 2.1. Experimental data of blue LED using the AuSn Solder die-attach

I_f (mA)	V_f (V)	Electrical power (W)	Radiant flux (W)	Heat dissipation (W)	T_s (°C)
250	2.934	0.733	0.316	0.417	69.6
500	3.194	1.597	0.593	1.004	63.8
750	3.428	2.571	0.835	1.736	57.5
1000	3.648	3.648	1.009	2.639	49.8

The transient junction temperature behavior can be obtained from the transient voltage behavior using the calibration curve. The transient junction temperature behavior is shown in Figure 2.8.

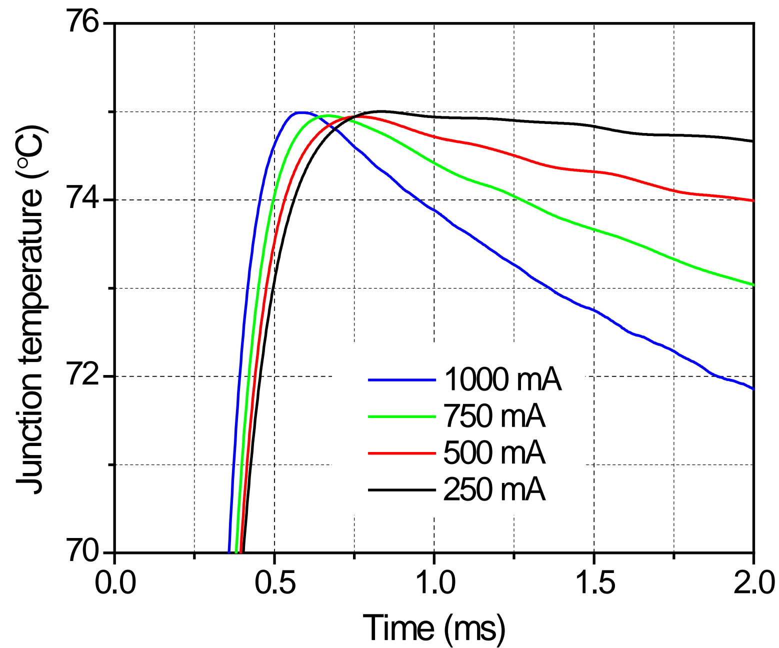

Figure 2.8. Transient junction temperature behavior at T_j^{Ap}= 75 °C

2.3. Transient Domain for Inverse Approach

The transient thermal behavior is affected by various layers in the LED device. In order to determine the DTI resistance accurately, it is first necessary to define the transient domain that is governed predominantly by the resistance of the DTI. This section describes a hybrid analytical/numerical model of multiple conduction thermal time constants that is utilized to determine the DTI dominant region.

2.3.1. Hybrid Analytical/Numerical Model

The hybrid analytical/numerical model used in the analysis is shown in Figure 2.9. The model consists of three main layers: the layers produce temperature differences (1) between the junction and the bottom surface of the die-attach (ΔT_1); (2) between the bottom surface of the die-attach and the bottom surface of the solder (ΔT_2); and (3) between the bottom surface of the solder and the bottom surface of the thermal paste (ΔT_3). Only the heat transfer in the downward conduction is considered in the model because the upward heat transfer through the lens, as well as the thermal radiation and convection, is assumed to be negligible (less than 1% of the total heat transfer) [69].

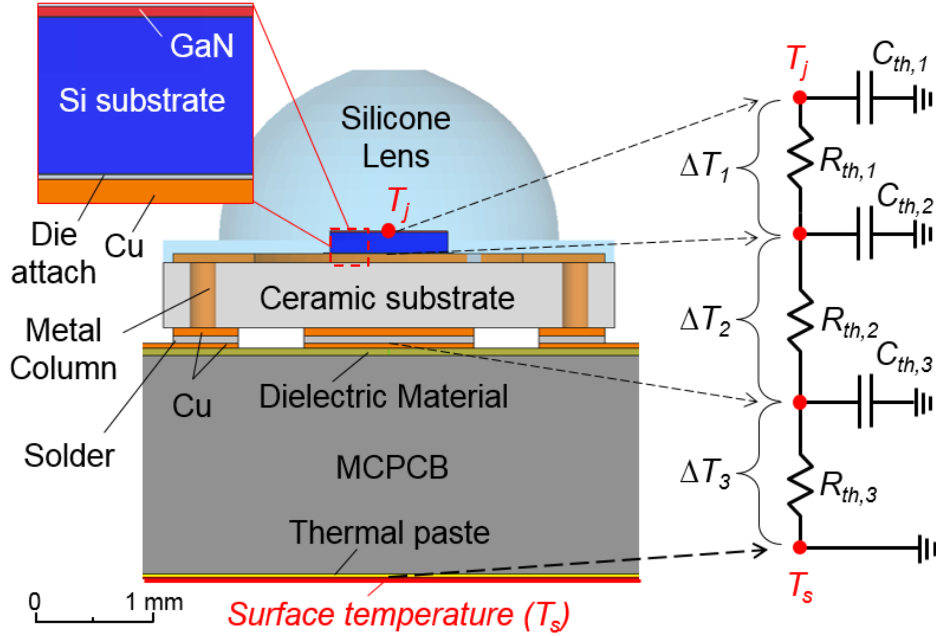

Figure 2.9. Schematic illustration of the hybrid analytical/numerical model

The thermal resistance and the thermal capacitance of each layer can be expressed as [31, 34]:

$$R_{th} = \frac{d}{k_s A} \tag{2}$$

$$C_{th} = c_p \rho A d \tag{3}$$

where R_{th} and C_{th} are the thermal resistance [K/W] and the thermal capacitance [J/K], d is the thickness along the heat transfer direction [m], A is the cross-section area [m^2], K_s is the thermal conductivity [W/(m·K)], c_p is the specific heat [J/(kg·K)], and ρ is the volumetric mass density [kg/m^3].

The product of the thermal resistance and the thermal capacitance is called thermal time constant, τ_{th} [s], which is defined as the heating or cooling time required

to produce a temperature change equal to 63.2% of the total temperature difference between the initial and the final body temperature. It can be expressed as [31, 34]:

$$\tau_{th} = R_{th}C_{th} = \frac{c_p \rho}{k_s} d^2 = \frac{d^2}{\alpha} \tag{4}$$

where α is the thermal diffusivity [m^2/s].

The equations (2) and (4) are valid only when the heat generated at the junction conducts along one dominant path. In an LED structure, however, additional heat spreading paths exist due to the large lateral dimensions of the heat generation layer and package layers, and thus, one-dimensional conduction, as represented in (2) and (4), is not directly applicable [70].

A supplementary numerical analysis was conducted to more accurately determine the LED thermal resistances, including the spreading resistances in various layers. The numerical model (ANSYS Icepak 15.0) used in the analysis is shown in Figure 2.10a. In the model, the epitaxial layers, typically just 1 μm thick, were modeled as a single effective layer to reduce the element count in the numerical model. The volume fraction and the mass fraction were used to determine the effective volumetric mass density and the effective specific heat, respectively, while the thermal resistance network equation was used to obtain the effective thermal conductivity of this layer. The effective volumetric mass density, specific heat, and conductivity used in the model are summarized in Table 2.2. The experimentally determined heat dissipation of 2.639 W at 1 A (Table 2.1) was used in the analysis.

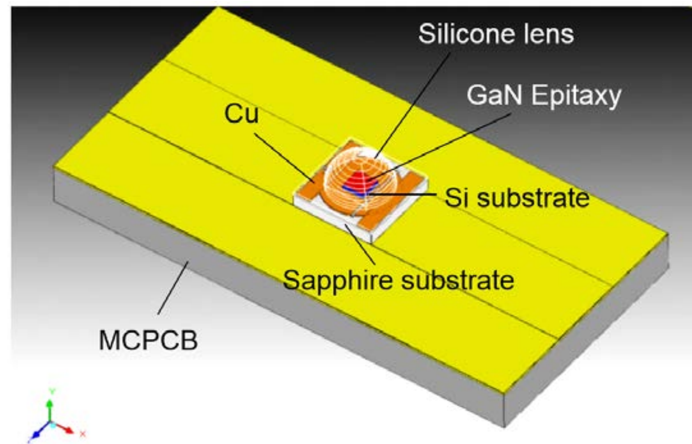

(a)

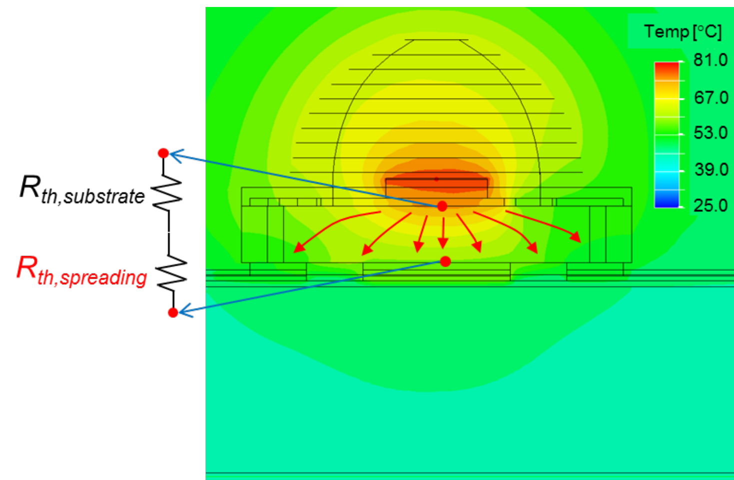

(b)

Figure 2.10. (a) 3D model and (b) temperature distribution at the steady state

Table 2.2. Material properties used in the numerical model and the analytical solution [71-76]

Name and materials	Volumetric mass density (kg/m^3)	Specific heat (J/kg·K)	Conductivity (W/m·K)
Silicone Lens (DOW OE6630)	1170	1512	0.2
Metal column (W, Mo)	14750	176	150
MCPCB (Solder Mask)	1250	1300	0.4
Effective Epi (GaN)	10494	261	70
Chip substrate (Si)	2330	713	124
Die-attach (AuSn)	14500	150	52
Die-attach (Ag)	1820	882	2.3
Cu layers	8933	385	401
Ceramic Substrate (Al_2O_3)	3960	880	22.3
Solder (PbSnIn)	8690	239	56.9
MCPCB (Dielectric material)	1900	795	2
MCPCB (Al)	2710	900	140
Thermal paste	2270	1000	2.3

Temperature distribution obtained at the steady state condition is shown in Figure 2.10b, where the ambient temperature is 25°C. The effective thermal resistances, including the spreading resistances, were calculated by

$$R_{th,i} = \frac{\Delta T_i}{P_h} \quad \text{for } i = 1, 2, 3 \tag{5}$$

where ΔT_i and $R_{th,i}$ are the temperature difference and the corresponding effective thermal resistance of each layer, respectively. The corresponding thermal capacitance, $C_{th,i}$, and thermal time constant, $\tau_{th,i}$, were calculated from Eqs. (3) and (4); the values are summarized in Table 2.3.

Table 2.3. Thermal resistance, thermal capacitance, and time constant used in the hybrid analytical numerical solution

Layer	Thermal resistance (K/W)	Thermal capacitance (mJ/K)	Time constant (ms)
1st layer	1.40	0.26	0.37
2nd layer	6.77	42.30	286.24
3rd layer	4.64	1683.02	7809.83

2.3.2. DTI Dominant Domain

The transient total junction temperature rise relative to the surface temperature, ΔT_j, can be described by a multiple exponential function with the π network (Cauer network) [31, 34], which can be expressed as:

$$\Delta T_j(t) = P_h\left[\sum_{i=1}^{3} R_{th,i}\cdot\exp\left(-t/\tau_{th,i}\right)\right] = \sum_{i=1}^{3}\Delta T_i\cdot\exp\left(-t/\tau_{th,i}\right) \text{ for } i = 1, 2, 3 \quad (6)$$

where $R_{th,i}$ and $\tau_{th,i}$ are the thermal resistance and the thermal time constant of the ith layer, respectively. Each ΔT_i is calculated simply by multiplying the heat dissipation and the thermal resistance of the ith layer.

The transient junction temperature behavior of the LED operated at the maximum allowable forward current (1A) is plotted in Figure 2.11a. The y-axis shows the temperature difference between the top and bottom of each layer, and the x-axis shows the time in a log scale. The sum of all three differences is equal to the temperature difference between the junction and surface temperatures; it is denoted as "Total ΔT_j" in the plot (the black line).

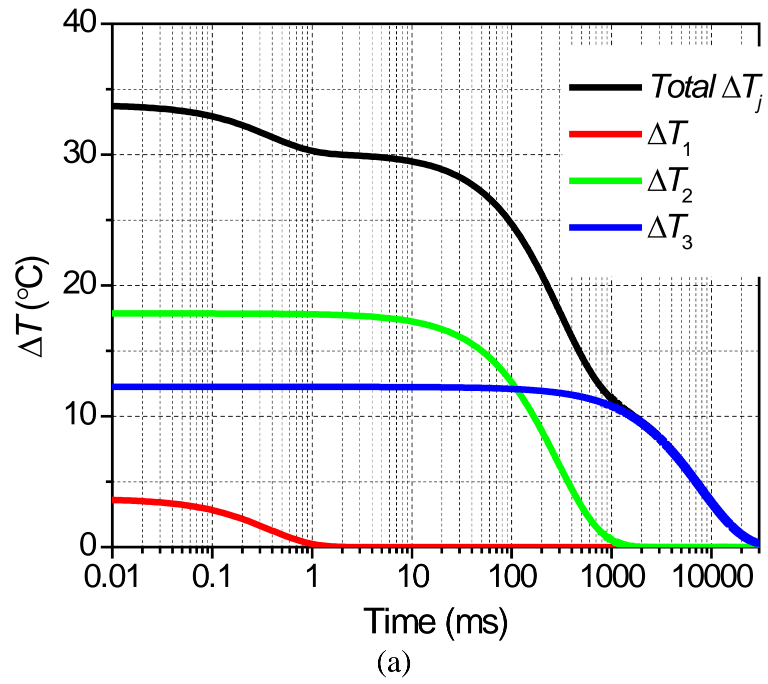

(a)

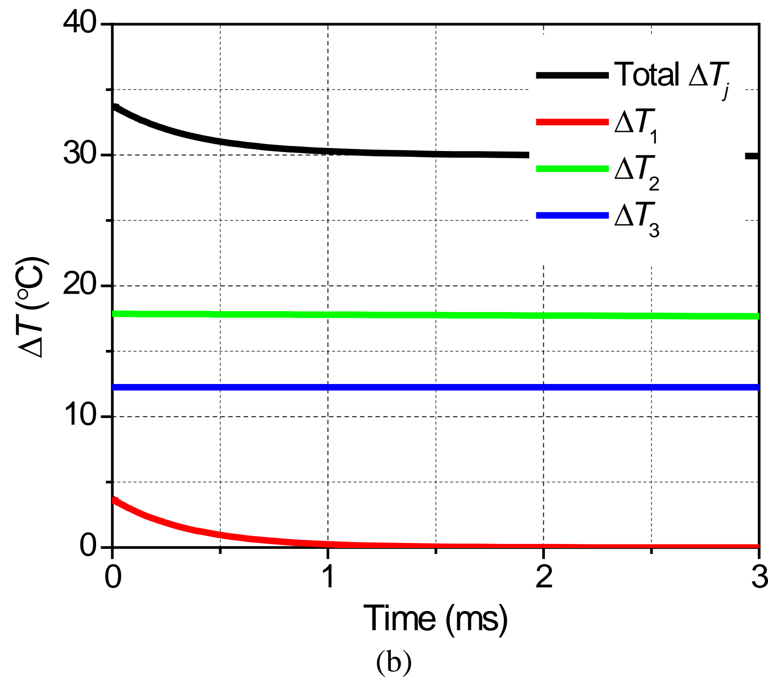

(b)

Figure 2.11. Transient behavior of ΔT for (a) 30,000 ms in the log scale and for (b) 3 ms in the linear scale

As expected from the extremely small value of the first layer's thermal time constant (Table 2.3), the transient behavior of the LED is governed only by the first layer for the first few milliseconds ($\approx 5 \cdot \tau_{th,1}$). This is illustrated in Figure 2.11b, where the transient behavior of each layer is plotted in the linear scale only for the first three milliseconds. The effect of the 2nd and the 3rd layer on the transient behavior of the total ΔT_j was also investigated. The thermal resistance of the 2nd and the 3rd layer was altered by $\pm 10\%$. The normalized ΔT_2 and ΔT_3 is plotted in Figure 2.12. As expected, the normalized temperatures are virtually unchanged for the first 3 ms due to the large time constants. This confirms that the transient behavior over $\approx 5 \cdot \tau_{th,1}$ can be used effectively to characterize the DTI. Considering the range of the thermal resistance of the DTI, the DTI dominant transient time domain was chosen as 2.0 ms and it will be used for the following analysis.

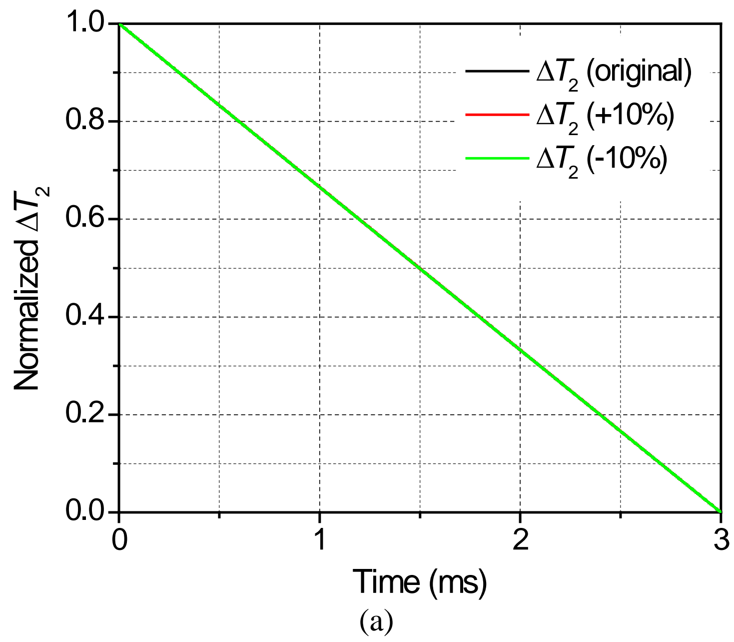

(a)

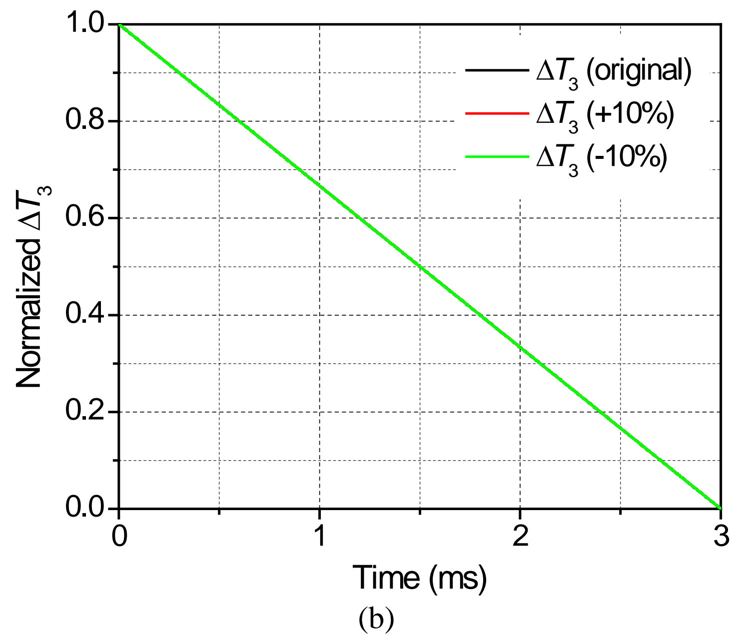

(b)

Figure 2.12. Normalized transient behavior of ΔT under the different thermal resistance of (a) second layer and (b) third layer

2.4. Inverse Approach to Determine the Resistance of DTI

In Step 1, a numerical simulation is conducted to determine the steady-state temperature distribution under an operating current. In Step 2, a transient numerical simulation is conducted after switching the heat dissipation from the operating condition to the probing condition (determined from Eq. (1)) while using the results from the previous analysis as the initial condition. The result of Step 2 provides the transient junction temperature behavior. The steady-state temperature distribution under an operating current of 1A is shown in Figure 2.13a (Step 1), and the corresponding transient temperature distribution at t = 2 ms is shown in Figure 2.13b (Step 2).

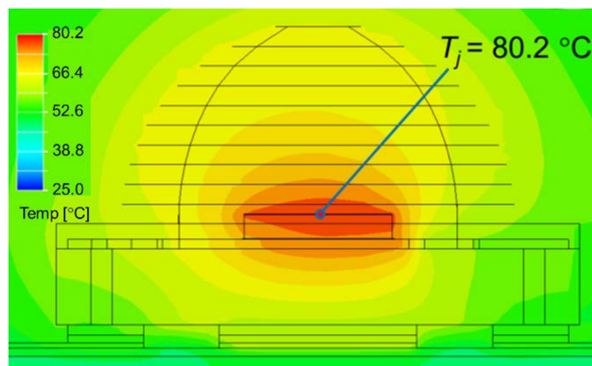

(a)

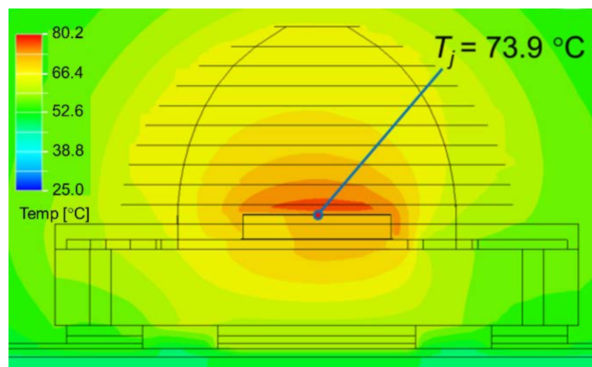

(b)

Figure 2.13. Temperature distribution at (a) 0 ms and (b) 2 ms

The next step is an iteration process, in which a small resistance that takes account of the DTI is continuously added to the bulk property of the die-attach material until the numerical results match the experimental data.

It is important to note that the bulk thermal conductivities of the packaging materials were not known accurately, which affected the junction temperature at $t = 0$. Before the iteration process began, the bulk thermal conductivities were adjusted until the numerical prediction matched to the experimental value at the end of the DTI dominant transient time domain, i.e., $t = 2$ ms. The temperature dependent properties did not have to be considered because the transient behavior of the junction temperature in the DTI dominant region was not affected by the bulk thermal conductivities and the chip temperature was nearly constant (around 75 °C).

The iteration was conducted in a two-step process: (1) a coarse increment of 0.1 K/W, and (2) a finer increment of 0.01 K/W. The final result after the iteration is shown graphically in Figure 2.14, where the zone affected by the RC-delay is marked as a shaded area. The DTI resistance was determined to be 0.32 K/W.

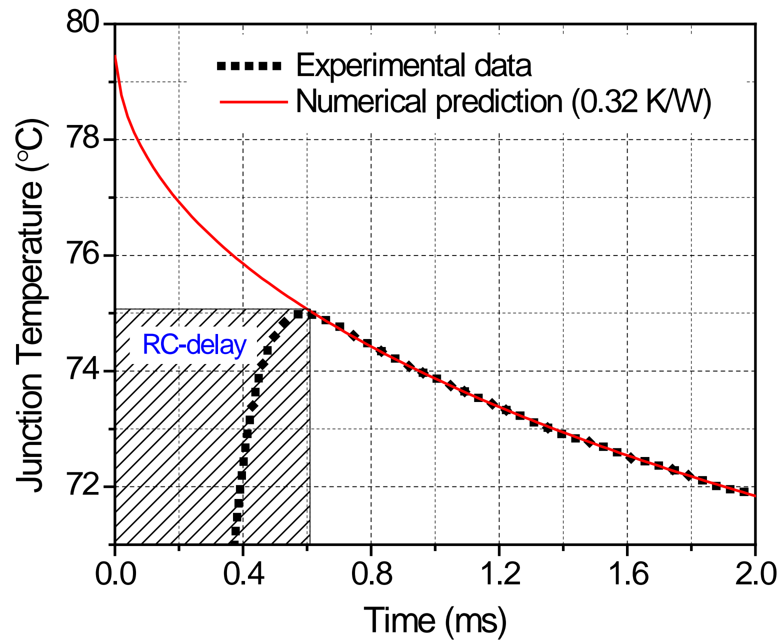

Figure 2.14. Experimental data is compared with numerical prediction after the iteration

2.5. Validity of DTI Resistance

The same LED used in Section 2.4 was tested under three other operating currents (250 mA, 500 mA and 750 mA) to validate the DTI resistance obtained from the inverse approach. For each case, the heat dissipation and the TEC surface temperature required for the apparent temperature of 75 °C were determined first. The values for the three operating currents are also summarized in Table 2.1.

The experimental results are compared with the modeling results obtained with the DTI resistance of 0.32 K/W in Figure 2.15. They match each other very well with the temperature difference within 0.05 °C in the calibration region, which is a clear indication that the DTI resistance determined by the proposed inverse approach is valid.

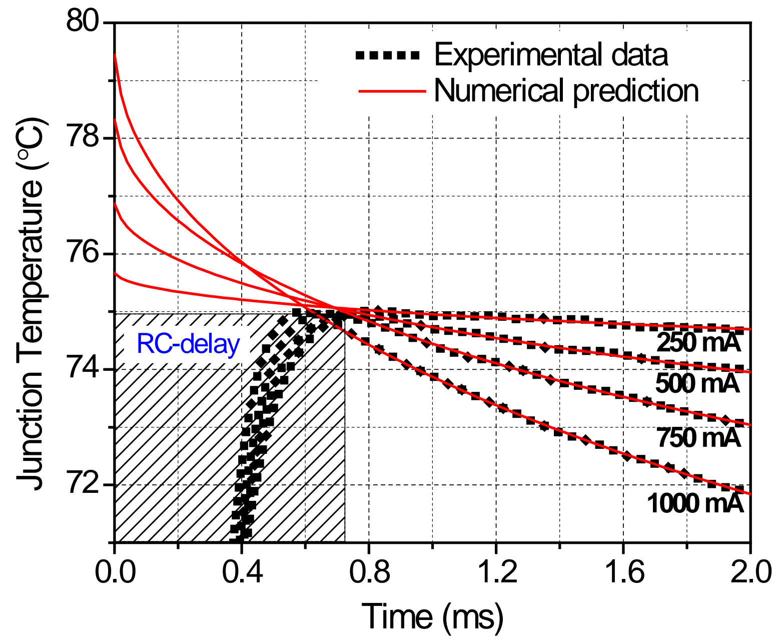

Figure 2.15. Predicted transient behavior of AuSn die-attach at different forward currents is compared with experimental data, where the DTI resistance obtained from Figure 2.14 is used in the numerical simulation.

The representative cross-section images of the AuSn die-attach layer are shown in Figure 2.16, which were taken at (a) 200X and (b) 1000X magnification. The random and contiguous void area in the die-attach (more than 50% of the total die-attach area) is evident. It is worth noting that the measured DTI resistance was 3.5 times larger than the thermal resistance calculated from the bulk property available in the literature (0.09 K/W). The large void area was attributed to the increase in the DTI resistance.

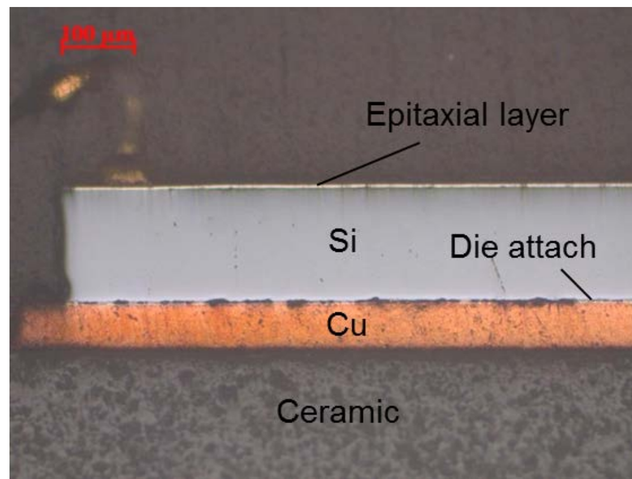

(a)

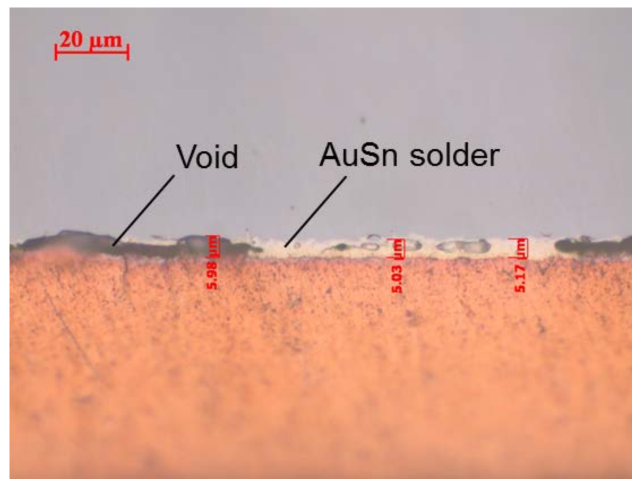

(b)

Figure 2.16. Cross-section image of the AuSn die-attach layer at (a) 200X and (b) 1000X magnification

The same procedure was implemented for a different die-attach material. It consisted of silver paste and AuSn solder. The nominal thickness of the die-attach was about 10 μm. The electrical power, the radiant flux, the heat generation rate, and the TEC surface temperature are summarized in Table 2.4.

Table 2.4. Experimental data of blue LED using the AuSn Solder and Ag paste die-attach

I_f (mA)	V_f (V)	Electrical power (W)	Radiant flux (W)	Heat generation rate (W)	T_s (°C)
250	2.891	0.723	0.300	0.423	67.5
500	3.139	1.569	0.550	1.020	58.9
750	3.358	2.519	0.788	1.731	48.8
1000	3.563	3.563	0.988	2.575	36.5

The DTI resistance was determined using the data obtained under an operating current of 1 A. It was 0.22 K/W and its accuracy was validated under three other operating currents (250 mA, 500 mA and 750 mA). The results are shown in Figure 2.17. The excellent agreement between the experimental data and the prediction not only proves the validity of the measurements but also supports a fact that the proposed scheme can be used for a wide range of die-attach materials.

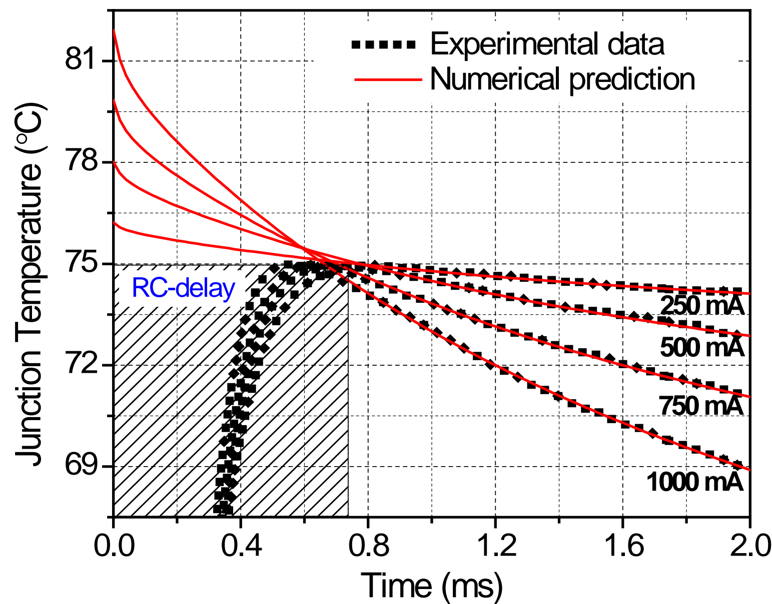

Figure 2.17. Predicted transient behavior of AuSn and Ag paste die-attach at different forward currents is compared with experimental data, where the DTI resistance obtained from the 1000 mA case is used in the numerical simulation

2.6. Conclusion

An inverse approach was proposed to determine the resistance of the DTI in high power LEDs. The transient time domain governed predominantly by the resistance of the DTI was selected first using the hybrid analytical/numerical solution. Then, the resistance of the DTI was determined inversely from the experimental data over the predetermined transient time domain using numerical modeling.

Supplementary experiments at various forward currents were conducted to verify the validity of the proposed method. The validity was further confirmed by measuring the actual voids in the die-attach layer. The same procedure was implemented for a different die-attach material. The results confirmed that the proposed approach offered a measurement accuracy of 0.01 K/W for various types of die-attach materials.

Chapter 3: Effect of Junction Temperature on Heat Dissipation of High Power Light Emitting Diodes

3.1. Introduction

Thermal management is essential for the design of light emitting diode (LED) based luminaires because a higher junction temperature reduces light output, luminous efficacy, and reliability [77-82]. Numerous analytical, experimental, and/or numerical analyses have been conducted to address various thermal issues of high power LEDs [39-43].

The temperature-dependent heat dissipation of an LED operated at a given forward current is defined as [44]:

$$P_h\left(T_j\right)\Big|_{I=I_f} = P_e\left(T_j\right)\Big|_{I=I_f} - P_o\left(T_j\right)\Big|_{I=I_f} = I_f \cdot V_f\left(T_j\right)\Big|_{I=I_f} - \Phi\left(T_j\right)\Big|_{I=I_f} \tag{7}$$

where I_f is the forward current [A]; T_j is the junction temperature [°C]; P_h is the heat dissipation [W]; P_e is the electrical input power [W]; P_o is the optical output power [W]; V_f is the forward voltage [V]; and Φ is the radiant flux [W]. The electrical input power is the product of the forward current and the forward voltage. The optical output power is the radiant flux.

The electrical input power, the optical output power, and thus the heat dissipation are altered by the junction temperature. It has been well-known that the forward voltage decreases as the junction temperature increases because of the

reduction of band gap energy at higher junction temperatures [4, 45-47]. Consequently, the electrical input power will decrease as the junction temperature increases, which helps reduce the heat dissipation.

It has also been well-known that the radiant flux decreases as the junction temperature increases because the non-radiative recombination increases with higher junction temperatures [48, 49]. As a result, the optical output power will also decrease as the junction temperature increases, which gives rise to the heat dissipation. To the best of authors' knowledge, the net results of this opposite effect on the final heat dissipation have not been clearly understood.

The objective of this chapter is, thus, to investigate quantitatively the effect of junction temperature on the heat dissipation. The theoretical aspect of junction temperature dependency of two major parameters – the forward voltage and the radian flux – is reviewed first. Actual measurements of heat dissipation over a wide range of the junction temperatures are followed to quantify the opposite effect of the two parameters using commercially available LEDs. The results are presented and the practical implications are discussed.

3.2. Background: Junction Temperature Dependent Forward Voltage and Radiant Flux

The theoretical aspect of junction temperature dependency of the forward voltage and the radiant flux is reviewed.

3.2.1. Forward Voltage

By considering the intrinsic carrier concentration, the band-gap energy, and the effective density of states, Xi *et al.* developed a theoretical model for the junction temperature dependency of the forward voltage, which was expressed as [46]:

$$\frac{dV_f}{dT_j} \approx \frac{k}{e} \ln\left(\frac{N_D N_A}{N_C N_V}\right) - \frac{\alpha_V T_j \left(T_j + 2\beta_V\right)}{e\left(T_j + \beta_V\right)^2} - \frac{3k}{e} \tag{8}$$

where *k* is the Boltzmann constant [J/K]; *e* is the elementary charge [C]; N_A and N_D are the acceptor and donor concentrations [m^{-3}]; N_C and N_V are the effective density of states at the conduction band and valence band edges [m^{-3}]; α_V [eV/K] and β_V [K] are the Varshni parameters. Using the parameters for the GaN blue LED, they obtained $dV_f / dT_j = -1.76$ mV/K. This negative linear relationship between the forward voltage and the junction temperature has been widely used to measure the junction temperature of high power LEDs, which has been known as the forward voltage method [46, 47, 58].

Keppens *et al.* studied the issue further to derive a more extensive forward voltage equation as a function of forward current and junction temperature, which was expressed as [47]:

$$V_f\left(I_f, T_j\right) = \left[\frac{n_{\text{ideal}} k}{e} \ln\left(\frac{I_f}{C_S}\right) - \frac{\alpha'}{e}\right] T_j + \frac{E_{g,300} + 300\alpha'}{e} \tag{9}$$

where n_{ideal} is the diode ideality factor; C_s is the combined temperature independent parameter; α' is the fitting parameters for the bad gap energy [eV/K]; and $E_{g,300}$ is the bandgap at 300 K [eV].

Equation (9) is valid for the junction temperature range from 295 K to 400 K, over which the relationship between the bandgap energy and the junction temperature is virtually linear [47]. As a result, the forward voltage and the junction temperature also has a linear relationship over the temperature range. The linear slope can be estimated from the parameters for the GaN blue LED available in the literatures. Using the values of $n_{\text{ideal}} = 1.52$, $k = 8.617 \times 10^{-5}$ eV/K, $e = 1.602 \times 10^{-19}$ C, $C_s = 255$, $\alpha' =$ 0.0003 eV/K, and $E_{g,300} = 2.926$ eV [47], the slope can be expressed in terms of the forward current as $1.31\times10^{-4}\ln(I_f) - 1.026\times10^{-3}$, which is negative for any operating current.

It should be noted that the bandgap energy cannot be approximated as a linear function of junction temperature at junction temperatures higher than 400 K. Consequently, a non-linear relationship between the junction temperature and the forward voltage should be established if the LED behavior at junction temperatures higher than 400 K is considered.

3.2.2. Radiant Flux

Reduction of the radiant flux is attributed to various temperature-dependent factors including non-radiative recombination, surface recombination, and carrier loss over heterostrucuture barriers [4, 12, 83, 84]. At the constant forward current, the radiant flux (Φ) is proportional to the external quantum efficiency (EQE), η_{ext}, [4, 85]; i.e.,

$$\Phi \propto \eta_{ex} = \eta_i \eta_{extraction} \tag{10}$$

where η_i is the internal quantum efficiency (IQE) and $\eta_{extraction}$ is the extraction efficiency. The extraction efficiency is affected largely by the LED chip configuration and refractive index [86, 87], and thus it is reasonable to assume that the temperature dependency of the radiant flux is caused mainly by IQE. The internal quantum efficiency has been described by the ABC model [88, 89], which is expressed as:

$$\eta_i = \frac{B_e n}{A_e + B_e n + C_e n^2} \tag{11}$$

where n is the carrier concentration [m^{-3}]; A_e is the Shockley-Read-Hall [s^{-1}]; B_e is the radiative coefficients [m^3/s]; and C_e is the Auger coefficients [m^6/s].

Due to this extreme complexity, the temperature dependence of the radiant flux has been often described by an empirical equation that describes the experimental results without a strong theoretical framework. The empirical equation can be expressed as [4, 84]:

$$\Phi \propto \exp\left(-\frac{T_j - T_{ref}}{T_{ch}}\right) = \exp\left(-\frac{1}{T_{ch}}T_j + \frac{T_{ref}}{T_{ch}}\right) \tag{12}$$

where T_{ref} is the reference temperature [K]; and T_{ch} is the characteristic temperature [K], which determine the characteristic of the temperature dependency. It has been known from the previous studies [4, 49, 84, 85, 90] that the characteristic temperature of GaN LEDs ranges from 79 K to 1639 K at the reference temperature of 300 K. Relative radiant flux changes as a function of junction temperature at the characteristic temperature at 79 K and 1639 K are shown in Figure 3.1. The radiant flux decreases as the junction temperature increases and has stronger temperature dependency with the lower characteristic temperature.

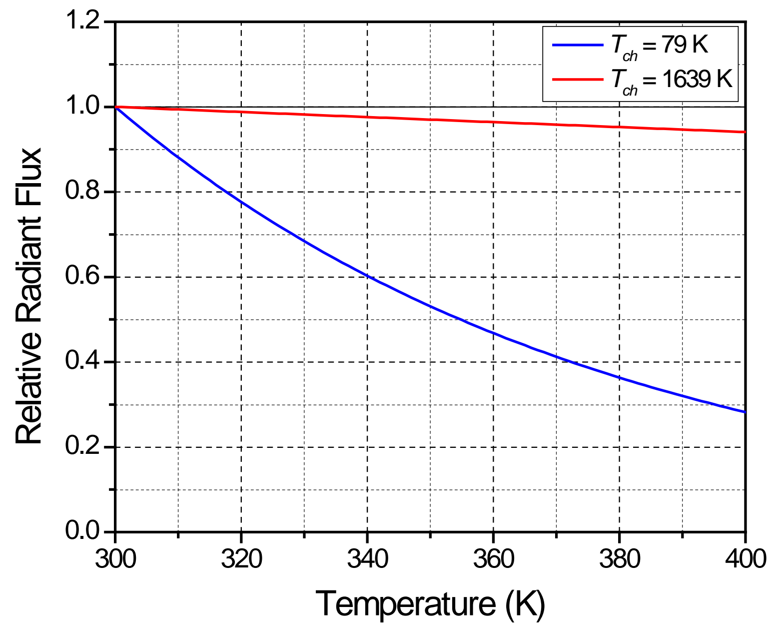

Figure 3.1. Relative radiant flux changes as a function of temperature at the characteristic temperatures of 79 K and 1639 K

3.3. Measurement of Heat Dissipation

The forward voltage and the radiant flux have to be measured as a function of junction temperature in order to quantify the opposite effect of the forward voltage and the radiant flux on heat dissipation. The heat dissipation is measured using two commercially available blue LEDs.

3.3.1. Specimen and Test Procedure

The cross-section image of high power blue LEDs tested in this study is shown in Figure 3.2. It is a typical high power blue LED for lighting applications, which has an internal thermal resistance of 9 - 10 K/W. The GaN blue chip is mounted on a

ceramic substrate to form a package, which is subsequently mounted on a metal core printed circuit board (MCPCB) using solder connections. Two LEDs from different manufactures were tested (will be referred to as LED1 and LED2).

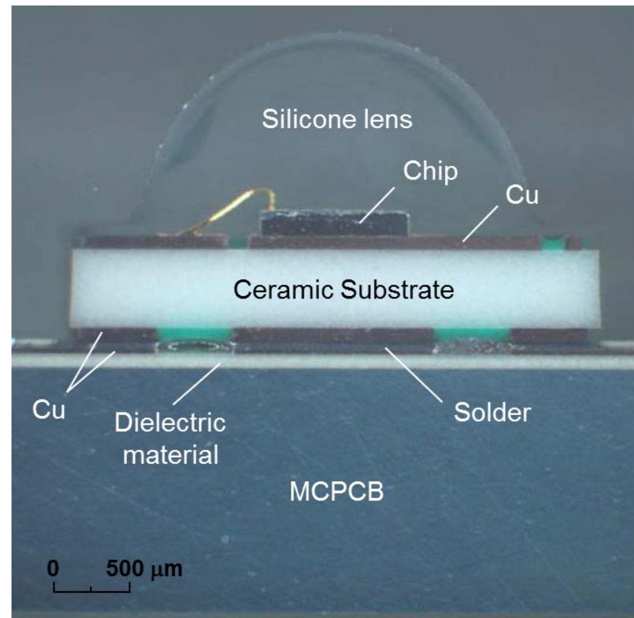

Figure 3.2. Cross-section image of a high power blue LED

A measurement setup is shown schematically in Figure 3.3. The junction temperature of the LED was controlled by a high precision hot plate (mk2000 and HCP304SC: ISTEC); it provided a temperature resolution of ±0.05 °C. The junction temperature at the operating current was measured using the forward voltage method [46, 47, 58]. The LED was operated by a sourcemeter (2420: Keithley Instruments); it provided the current source accuracy of ±(0.067% + 900 μA). A data acquisition (DAQ) module (USB-6212: National Instruments) was utilized to measure the forward voltage of the LED with 16-bits resolution. When a desired junction temperature was reached,

the spectral power distribution (SPD) was measured by an integrating sphere equipped with 16-bits resolution of a spectrometer (SMS–500: SphereOptics).

The heat dissipation was measured over a wide range of junction temperatures (from 25 °C to 200 °C) at a low (250 mA) as well as high forward current (1000 mA) which was the maximum forward current suggested by the manufactures.

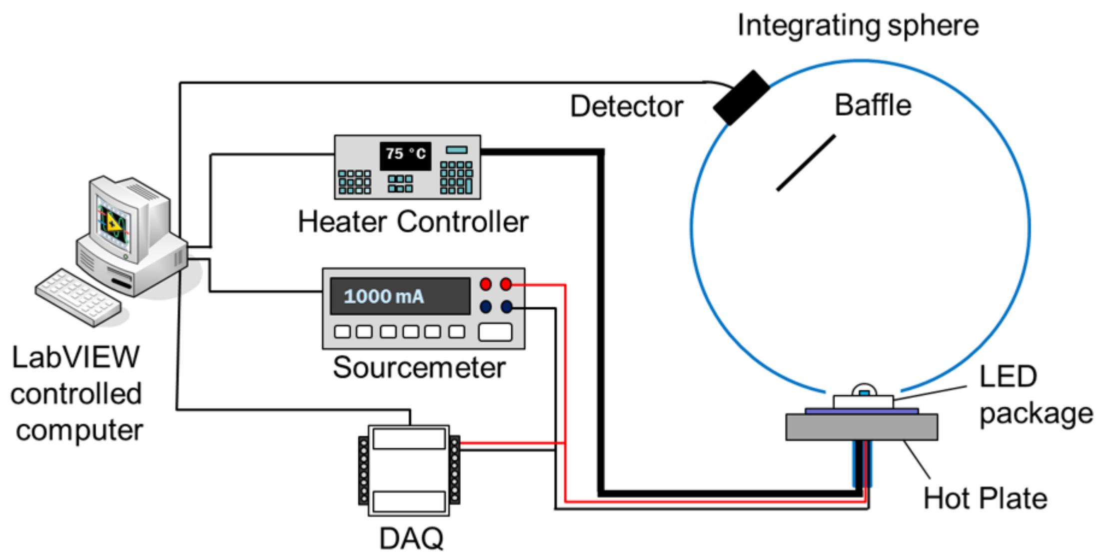

Figure 3.3. Schematic illustration of the measurement setup

3.3.2. Junction Temperature Measurement

The relationship between the junction temperature and the forward voltage (known as the calibration curve) can be obtained by measuring the forward voltage using a low probe current (5 mA) for a short period of time (10 ms). The calibration curve of LED1 and LED2 is shown in Figure 3.4, where a linear fit as well as a polynomial fit is given.

For the current study, the calibration data were obtained over a temperature range much wider than a typical LED operating temperature range, which exceeded the linear region (400 K) as discussed in Section 3.2.1. In Figure 3.4, deviation from the linearity is evident beyond 125 °C for the both LEDs. The error of the forward voltage at 200 °C between the linear fitting and the measured data is approximately 13 mV and 5 mV for LED1 and LED2, respectively, which corresponds to the junction temperature error of 10 °C and 2 °C. For the current study, a cubic polynomial was used, which produced an ideal fit with the experimental data.

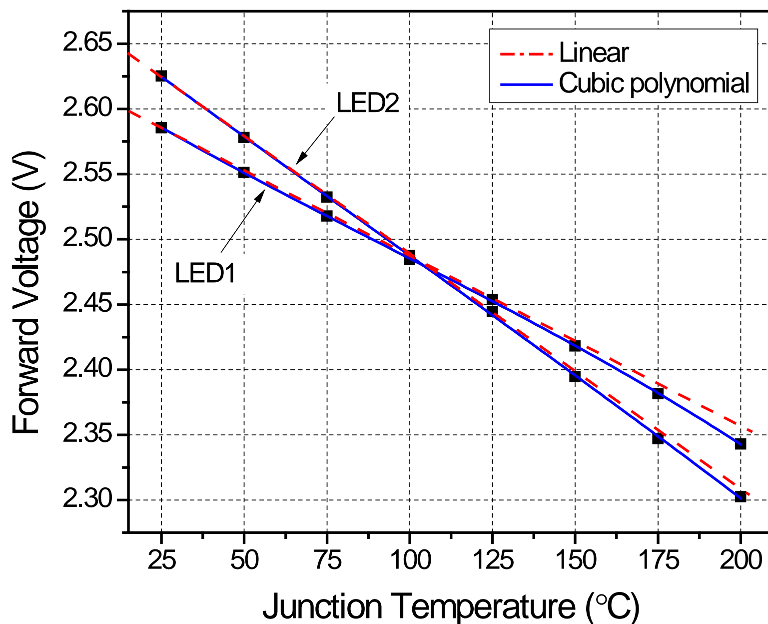

Figure 3.4. Calibration curve of LED1 and LED2

In the actual measurements, the probe current is applied after an LED reaches the steady state condition. As discussed extensively in Ref. [65], the forward voltage shows the combined behavior of RC delay and thermal delay. The forward voltage

decreases exponentially due to RC delay, which is caused by a resistance of an LED and a capacitance of a current source, while the forward voltage increases due to the thermal delay, which is caused by the exponential decrease of the junction temperature.

Figure 3.5a shows the transient voltage behavior of LED1 obtained after the probe current of 5 mA is applied. The enlarged view of the region marked by a dashed box is shown in Figure 3.5b. The RC delay dominates initially (Zone 1). The thermal delay begins to override the RC delay (Zone 2). Then the voltage behavior follows an exponential increase (Zone 3). This exponential voltage behavior only after the RC delay-affected period (Zones 1 and 2) represents the junction temperature accurately; i.e., this voltage is only valid for junction temperature estimation using the calibration curve.

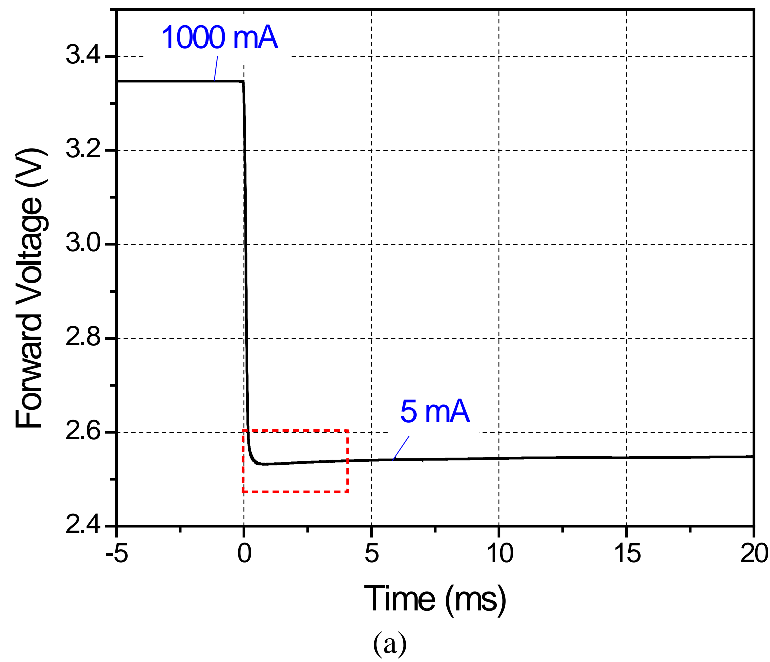

(a)

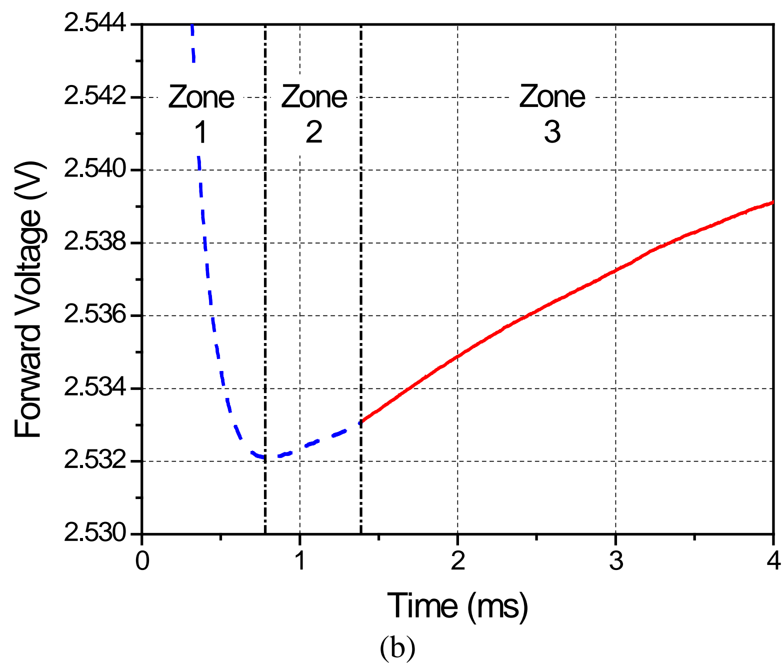

(b)

Figure 3.5. (a) Transient voltage behavior of LED1 after the probe current is applied and (b) enlarged view of the region marked by a dashed box.

The voltage of Zone 3 converted by the calibration curve is shown in Figure 3.6. The square root of the time scale is used in Figure 3.6, which is required to implement the linear extrapolation [91-93]. The extrapolation is based on the theory that a junction temperature changes linearly in a square root time scale if heat is dissipated in one direction (i.e., one-dimensional space) through a homogenous material [91-93]. The linear fitting is also shown in Figure 3.6 with the estimated junction temperature at the operating current. The repeatability of the junction temperature measurement was less than 0.1 °C, which was attributed to the current source accuracy.

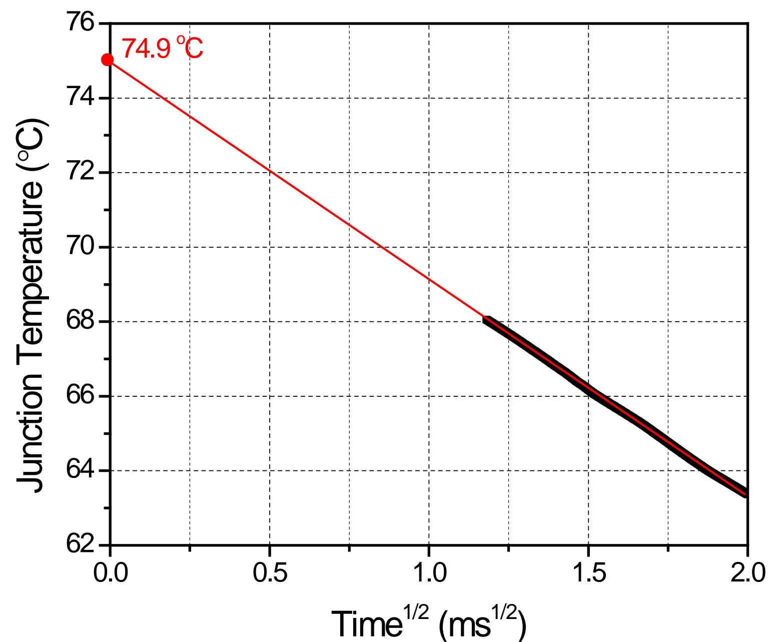

Figure 3.6. Junction temperatures obtained from the voltage of Zone 3 is plotted in the square root time scale; the linear extrapolation provides the estimated junction temperature at the operating current.

3.3.3. Heat Dissipation Measurement

The radiant flux can be calculated from SPDs. The SPDs of LED1 at the operating currents of 250 mA and 1000 mA are shown in Figure 3.7. It is worth noting that a significant center wavelength shift is observed as the bandgap energy is reduced significantly over the large temperature range [45]. The SPDs of LED2 are shown in Figure 3.8 and have a similar behavior.

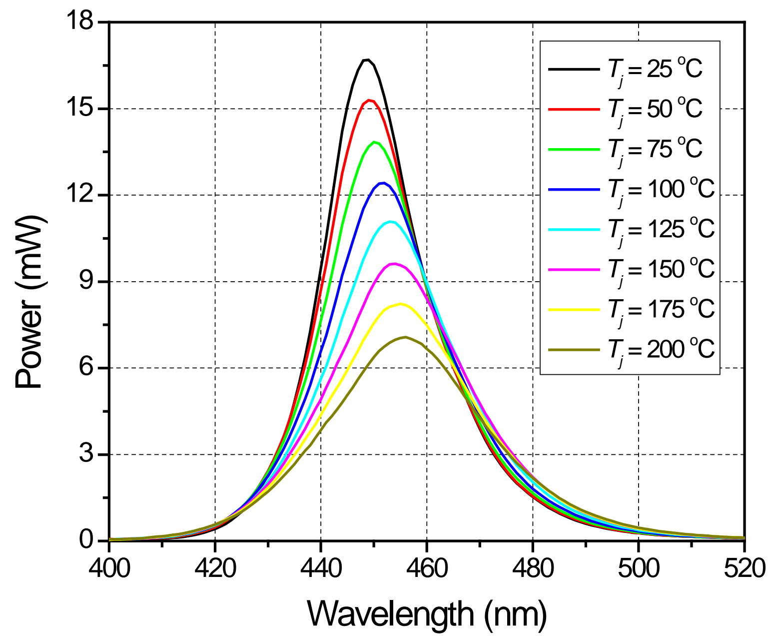

(a)

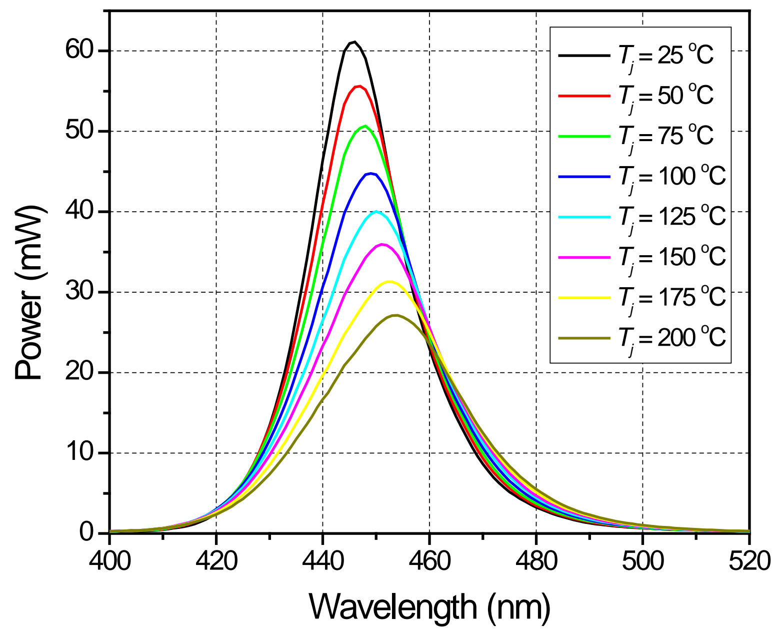

(b)

Figure 3.7. SPDs of LED1 at the forward current of (a) 250 mA and (b) 1000 mA

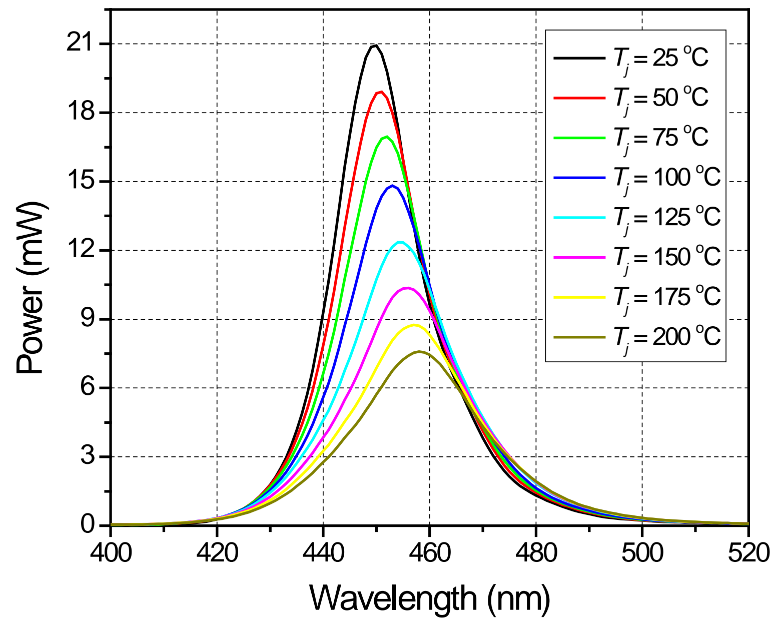

(a)

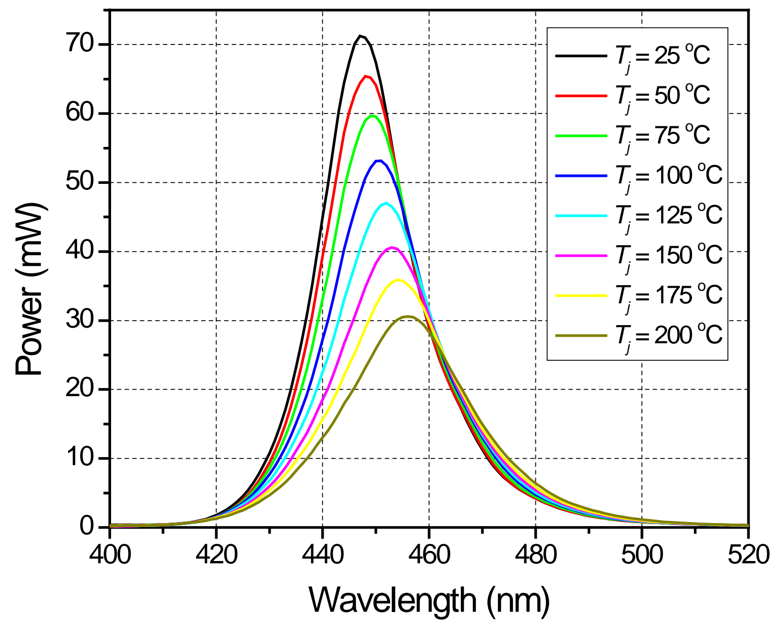

(b)

Figure 3.8. SPDs of LED2 at the forward current of (a) 250 mA and (b) 1000 mA

The junction temperature-dependent radiant flux of LED1 and LED2 (with an accuracy of 0.05 W) is shown in Figure 3.9. The radiant fluxes decrease at different rates as the junction temperature increases. As mentioned in Section 3.2.2, the different reduction rate is caused mainly by the IQE of LED chips.

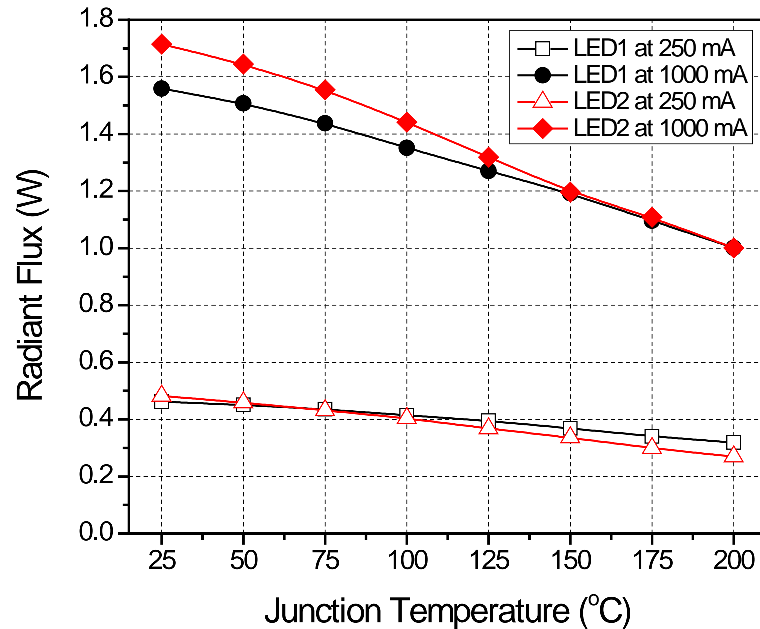

Figure 3.9. Radiant fluxes as a function of junction temperature

The junction temperature-dependent forward voltage is shown in Figure 3.10, from which the junction temperature-dependent electrical input power is determined. The reduction rates of two LEDs are virtually the same because materials used in the epitaxial layer dictate the temperature dependency of the forward voltage. The different absolute value at the same junction temperature is attributed to the difference in internal series resistances [47].

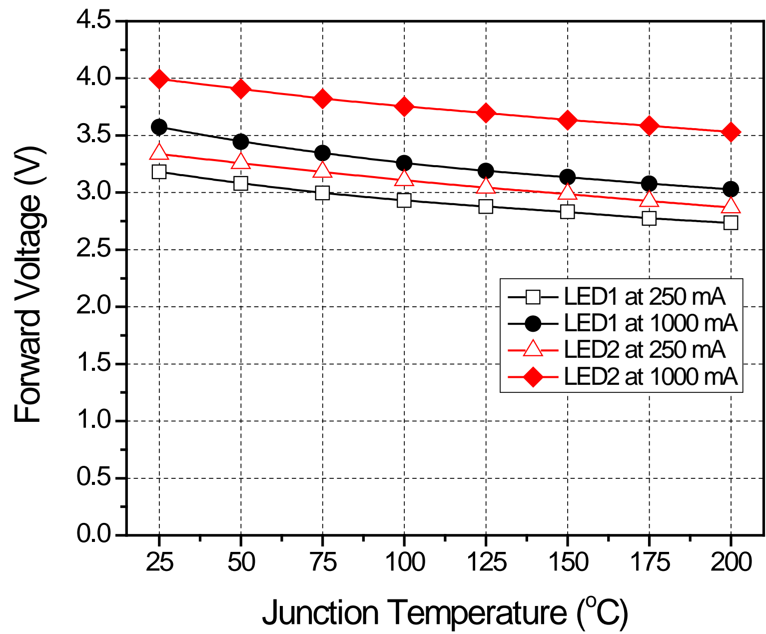

Figure 3.10. Forward voltage as a function of junction temperature

The heat dissipations were calculated by subtracting the optical output power (Figure 3.9) from the electrical input power. The results of LED1 and LED2 at the operating currents of 250 mA and 1000 mA are shown in Figure 3.11a and Figure 3.11b, respectively. The heat dissipation changes nonlinearly as a function of junction temperature.

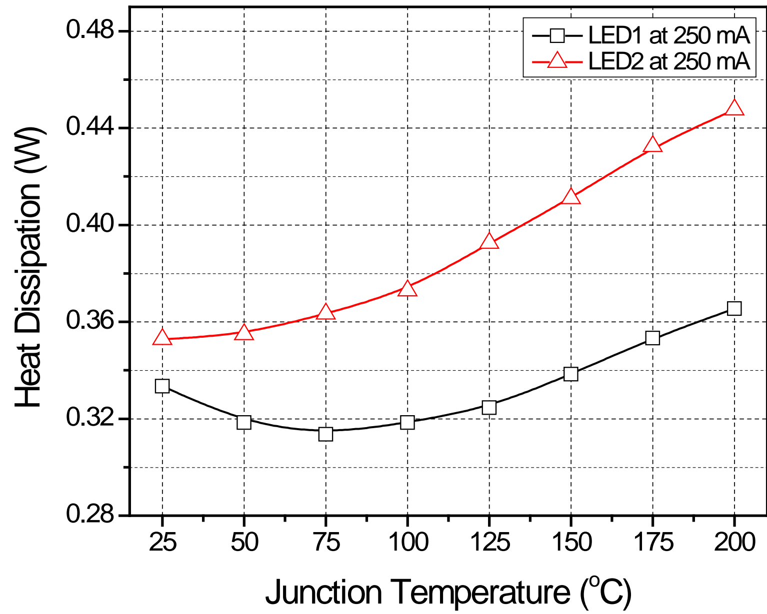

(a)

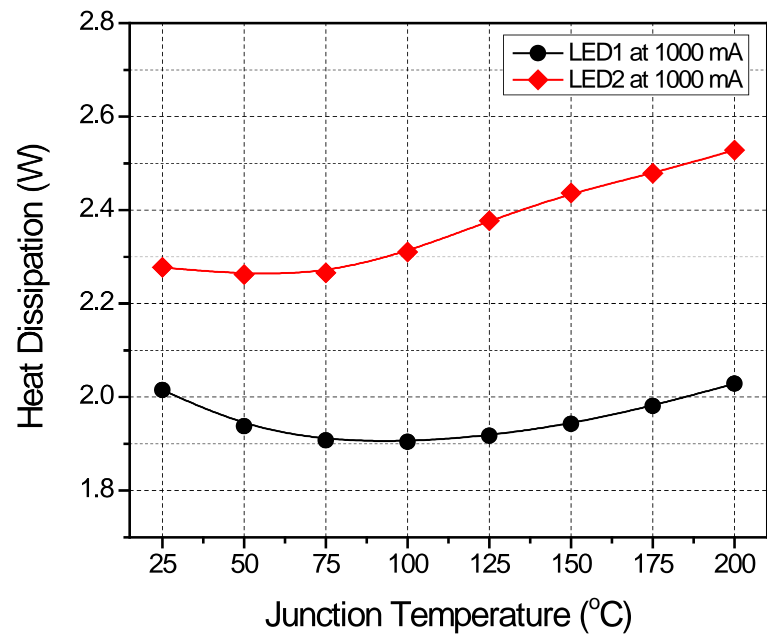

(b)

Figure 3.11. Heat dissipations as a function of junction temperature at (a) 250 mA and (b) 1000 mA

3.4. Junction Temperature Dependency

The changes of electrical input power, optical output power, and heat dissipation with respect to the reference temperature of 25 °C were calculated to quantify the effect of the junction temperature dependency. The percent changes are defined as:

$$\text{Electrical input power change in \%}\left(T_j\right)=\frac{I_f\cdot V_f\left(T_j\right)-I_f\cdot V_f\left(25\,^{\circ}\mathrm{C}\right)}{I_f\cdot V_f\left(25\,^{\circ}\mathrm{C}\right)}\times 100 \quad (13)$$

$$\text{Optical output power change in \%}\left(T_j\right)=\frac{\Phi\left(T_j\right)-\Phi\left(25\,^{\circ}\mathrm{C}\right)}{\Phi\left(25\,^{\circ}\mathrm{C}\right)}\times 100 \quad (14)$$

$$\text{Heat dissipation change in \%}\left(T_j\right)=\frac{P_h\left(T_j\right)-P_h\left(25\,^{\circ}\mathrm{C}\right)}{P_h\left(25\,^{\circ}\mathrm{C}\right)}\times 100 \quad (15)$$

The results are shown in Figure 3.12. The percent change of optical output power was much larger than that of electrical input power; 2.2 and 3.1 times larger for LED1 and LED2 at 250 mA and 2.3 and 3.6 times larger for LED1 and LED2 at 1000 mA. For LED1, the percent change of heat dissipation is 10% at 250 mA and 6% at 1000 mA. The percent change of heat dissipation of LED2, however, is much larger; 27% at 250 mA and 11% at 1000 mA.

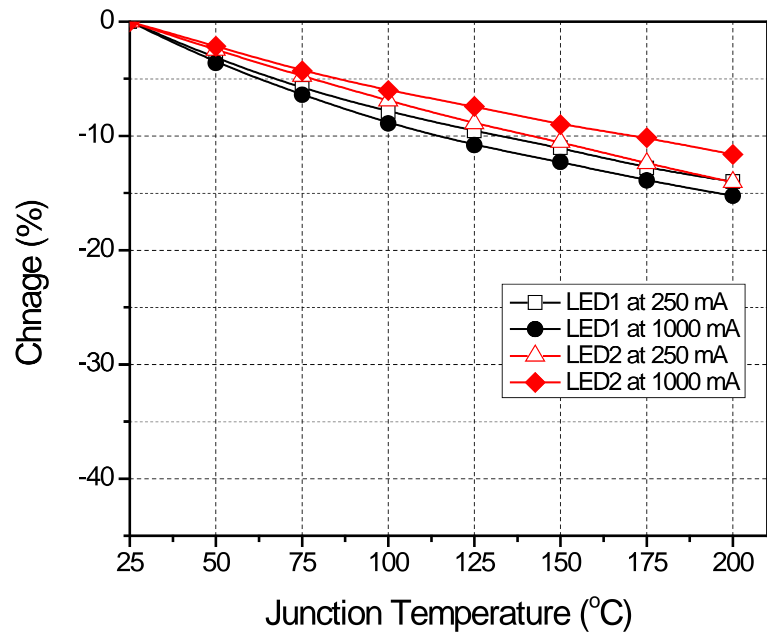

(a)

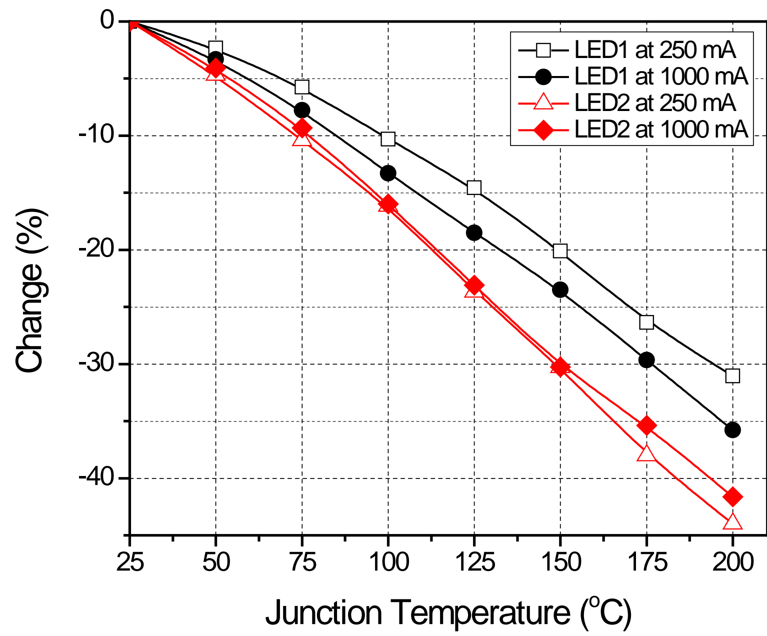

(b)

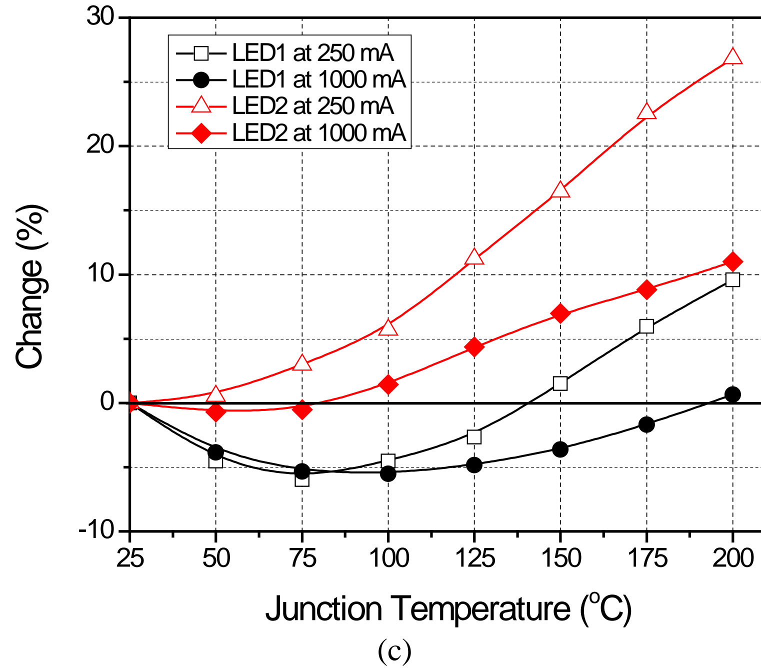

(c)

Figure 3.12. Percent changes of (a) electrical input powers, (b) optical output powers, and (c) heat dissipations as a function of junction temperature

The percent change difference of heat dissipation can be explained by the power efficiency of LEDs used in the study. The heat dissipation equation (Equation (7)) can be rewritten as:

$$P_h(T_j) = P_e(T_j) - P_e(T_j)\cdot\eta_p(T_j) = I_f\cdot V_f(T_j)\left[1-\eta_p(T_j)\right] \qquad (16)$$

where η_p is the power efficiency, which is defined as the optical output power divided by the electrical input power. It is clear from Equation (16) that the heat dissipation is governed by not only the forward voltage change but also the power efficiency change.

The power efficiency can be readily determined from the optical output power (Figure 3.9) and the electrical input power. The results are shown in Figure 3.13. At the forward current of 250 mA, the power efficiency at room temperature is 58%, and it drops to 47% and 38% at 200 °C for LED1 and LED2, respectively. At the forward

current of 1000 mA, the power efficiency at room temperature is 44% (LED1) and 43% (LED2), and it drops to 33% and 28% at 200 °C, respectively.

The larger power efficiency change of LED2 caused the effect of the optical power change to be stronger. As a result, the junction temperature dependency of LED2 is much higher than LED1. The junction temperature dependency of the heat dissipation can be different from the results obtained from the current study if an LED has power efficiency significantly different from the values shown in Figure 3.13.

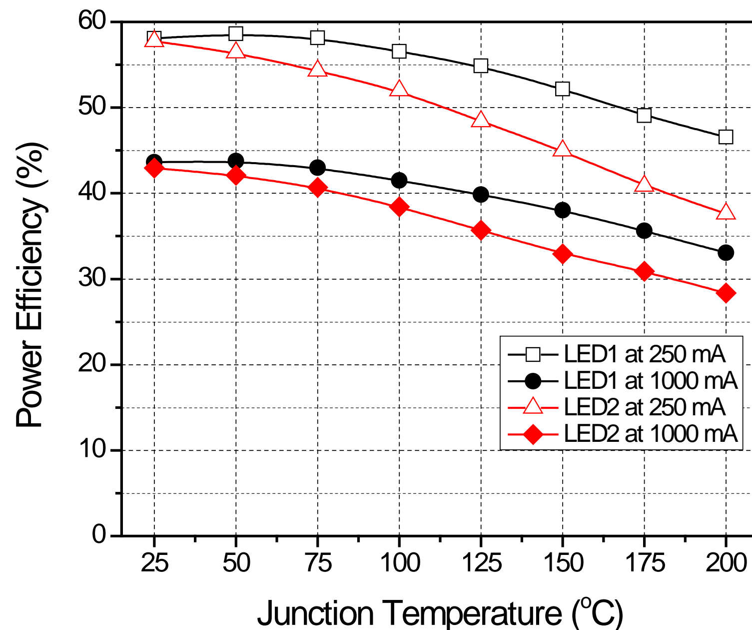

Figure 3.13. Power efficiency as a function of junction temperature

3.5. Empirical Heat Dissipation Model

This section is devoted to practical implications of the current study for the thermal management of LED-based luminaries.

3.5.1. Practical Consideration

Due to the compensation effect, the heat dissipation changes over the whole temperature range are only 0.11 W and 0.25 W for LED1 and LED2, respectively, (Figure 3.11). The corresponding junction temperature change is less than 2.5 °C assuming the thermal resistance of 10 K/W. Therefore, it is reasonable to assume in practice that the heat dissipation of blue LEDs is only a function of forward current over the typical operation temperature range (less than 125 °C).

In fact, the heat generation issue is more critical to LED-based luminaires using phosphor converted (pc-) white LEDs since thermal management is one of the most important tasks in the design [82]. In pc-LEDs, extra heat is generated due to the energy loss known as Stokes' shift [94]. It has been known that the total phosphor heat generation can vary from 5% to 40% of the blue input power, depending upon the concentration, thickness, particle size, and quantum efficiency of phosphors [95, 96]. The phosphor heat generation has some temperature dependency due to the phenomenon known as thermal quenching [94, 97, 98], but its effect is not significant (less than 10%) over the typical luminaire operating temperature range [97, 98]. This implies that the junction temperature dependency of heat dissipation is also not significant for pc-white LEDs. Two pc-white LEDs using the similar blue chips were tested to investigate it experimentally.

Two white LEDs (one cool white and one warm white: will be referred to as CW-LED3 and WW-LED4, respectively) contain a conformal phosphor layer. They were tested over a junction temperature range from 50 to 125 °C. Higher forward

currents (1250 and 1500 mA) were included in the test considering the trend of increased operating currents.

The results of the heat dissipation of CW-LED3 and WW-LED4 are shown in Figure 3.14. The heat dissipation of CW LED3 at T_j = 50 °C and I_f = 1500 mA and WW LED4 at T_j = 50 °C and I_f = 1250 mA and 1500 mA could not be measured due to the limitation of the hot plate performance.

As expected, the maximum heat dissipation changes over the whole temperature range are only 0.11 W and 0.12 W for CW-LED3 and WW-LED4, respectively, which correspond to the junction temperature change of 1.1 °C and 1.2 °C assuming that the thermal resistance is 10 K/W.

The results confirm that the compensation effect on the junction temperature dependency of the heat dissipation is consistent for pc-white LEDs in the current market. The effect of the temperature dependent heat dissipation will be even smaller as the thermal resistance decreases in the future LEDs. Therefore, it is reasonable to assume that the heat dissipation is virtually the same regardless of the junction temperature. Then, the governing equation for the heat dissipation can be written in an approximated form as:

$$P_h\left(T_j\right)\Big|_{I=I_f} \approx P_h\big|_{I=I_f} = I_f \cdot V_f\left(T_j\right)\Big|_{I=I_f} - \Phi\left(T_j\right)\Big|_{I=I_f} \tag{17}$$

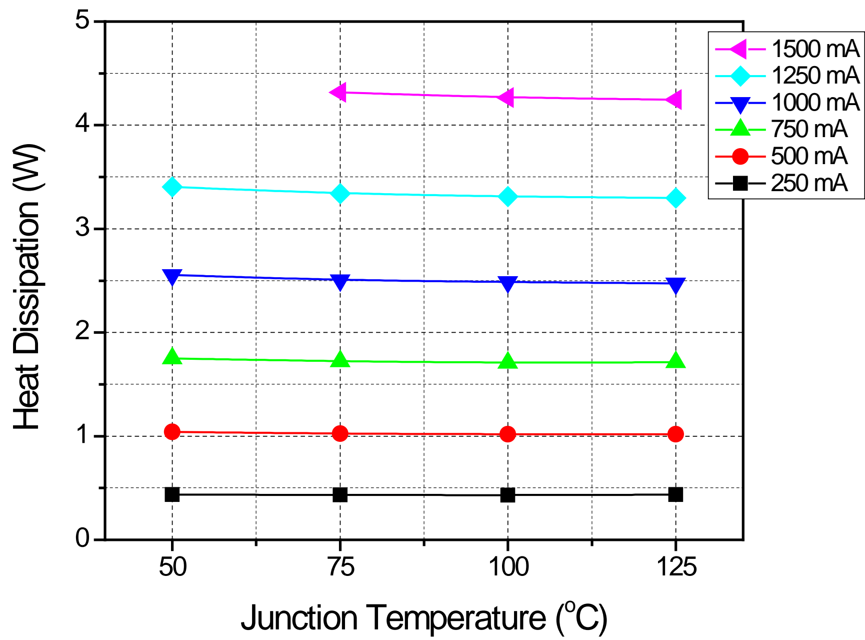

(a)

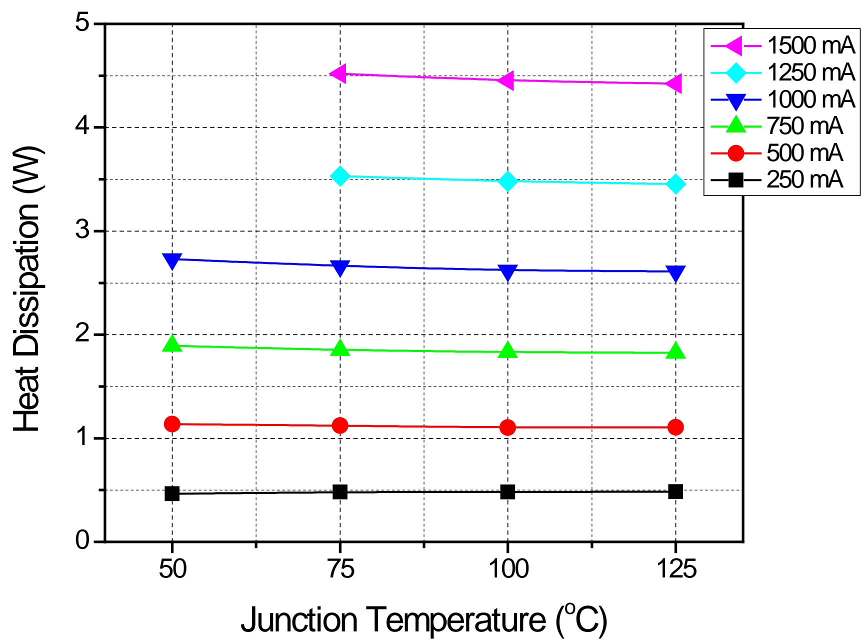

(b)

Figure 3.14. Heat dissipation of (a) CW-LED3 and (b) WW-LED4 as a function of junction temperature

3.5.2. Empirical Model

An empirical relationship between the heat dissipation and the forward current is proposed for applications in practice. It has been observed that the heat dissipation increases exponentially with the forward current. Considering the fact that the heat dissipation at the zero current should be zero, the relationship can be modeled as:

$$P_h = \mathrm{A_f} \exp\left(I_f / \mathrm{B_f} \right) - \mathrm{A_f} \tag{18}$$

where A_f and B_f are variables for the exponential function. Theoretically, any two current data are sufficient to obtain the constants, but, in practice, an extra data point is usually required to minimize the effect of the measurement uncertainty. Since the model is bound at the zero current, the middle and largest values in the current range of interest are recommended for the regression.

The heat dissipations of CW-LED3 and WW-LED4 obtained at T_j = 75 °C (Figure 3.14) was implemented using the proposed approach. The results are shown in Figure 3.15a. The heat dissipation obtained at different currents (Figure 3.14) is compared with the predicted value and the difference is plotted in Figure 3.15b. The maximum heat dissipation difference (calculated by subtracting the predicted values from the measured values) is smaller than 0.06 W. The results confirm that the heat dissipation can be estimated accurately at any current by using heat dissipation data obtained at two forward currents at any junction temperature.

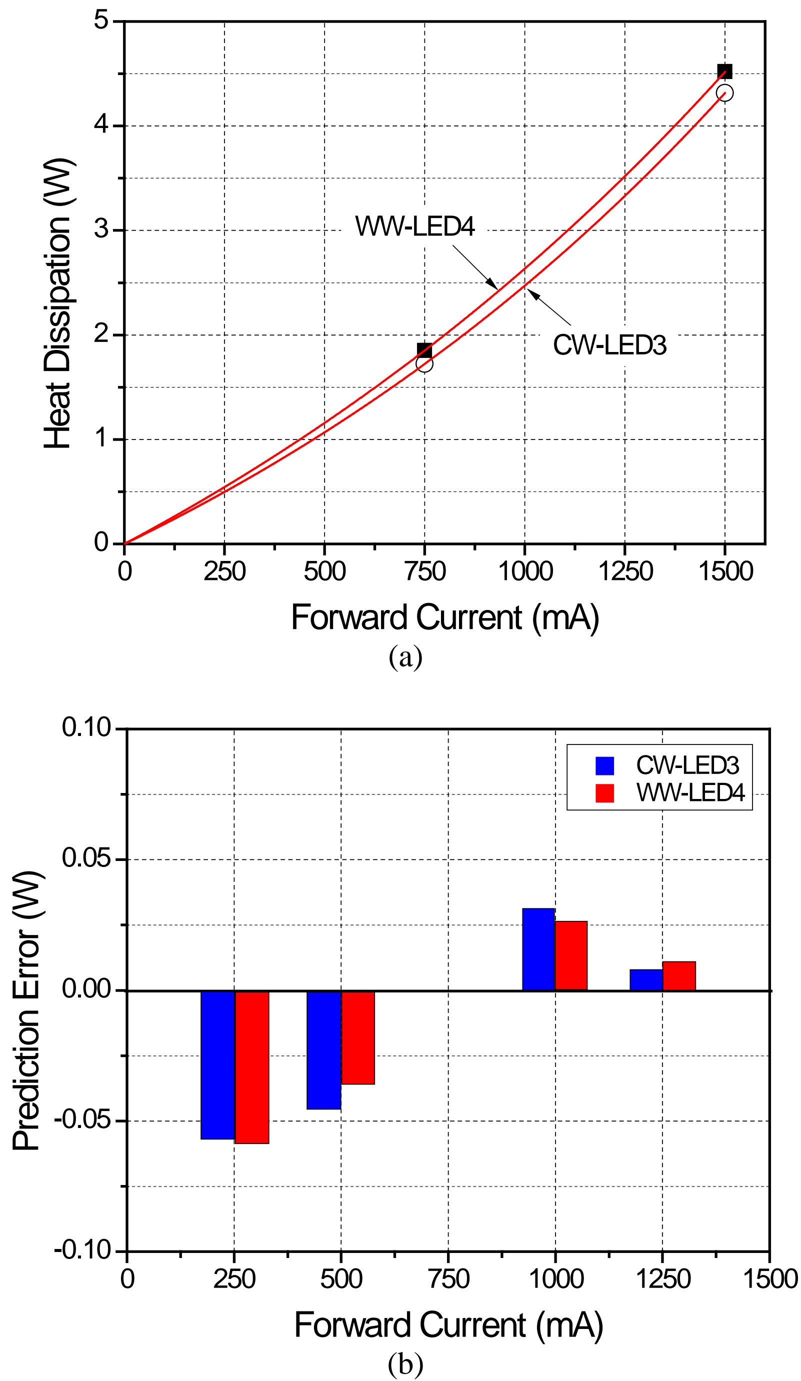

Figure 3.15. (a) Heat dissipation of CW-LED3 and WW-LED4 predicted by the empirical model and (b) difference between predicted values and measured values

3.6. Conclusion

The effect of the junction temperature dependency on the heat dissipation was investigated. The theoretical review confirmed that the forward voltage reduction at higher junction temperatures compensated the heat dissipation that was increased by the radiant flux reduction. Actual measurements of the heat dissipation over a wide range of the junction temperatures were performed to evaluate the compensation effect quantitatively. The results showed that (1) the effect of the junction temperature dependency on the heat dissipation was governed largely by the power efficiency and (2) the compensation effect was so strong that the absolute changes of the heat dissipation were not significant over the junction temperature range considered in the study (from 25 °C to 200 °C).

Supplementary experiments using phosphor-converted white LEDs were conducted over the typical operating temperatures of LED-based luminaires. Due to the small temperature dependency of phosphor heat generation, the heat dissipation of pc-LEDs was confirmed to be virtually the same regardless of the junction temperature.

Based on the results, the empirical heat dissipation model that was only a function of the forward current was proposed. The model requires the heat dissipation data only at two currents but can accurately estimate the heat dissipation at any forward current (and at any temperatures).

Chapter 4: Hybrid Experimental/Numerical Method to Predict Junction Temperature Distribution of High Power Laser Diode Bar

4.1. Introduction

High power laser diodes (LDs) have emerged as the most promising pumping sources for solid state lasers and fiber lasers and for a variety of applications in communication, cosmetic and medical applications, material surface treatment, joining technologies, cutting technologies, and defense applications [5-11]. The junction temperature is one of the most important parameters in achieving optimal performance of a high power LD bar, determining the center wavelength, spectrum distribution, wall-plug efficiency, and reliability [15-19]. Thus, experimental and analytical determination of the junction temperature is critical for the proper operation of the diode as well as the development of the packaging design.

As higher optical power is demanded for advanced applications, more closely-spaced emitters with higher forward current are used in LD bars. As a result, the junction temperatures of adjacent emitters may have large variations, which can lead to different center wavelength and wall-plug efficiency of each emitter, and result in low pumping efficiency and reliability, respectively.

Several junction temperature measurement methods for low power LDs or light emitting diodes (LEDs) have been proposed, including techniques based on measurement of the thermal resistance [50], wavelength-shift [51, 52], optical power

output [51], and forward-voltage [46, 47, 51, 53-58]. These methods are applicable only when the junction temperature is uniform. Micro-Raman spectroscopy [59-61] can be used to measure the junction temperature distribution by measuring multiple local temperatures. However, it has limited accuracy and requires a complicated experimental setup [59-61].

The objective of this chapter is, thus, to propose a hybrid experimental/numerical method to predict the junction temperature distribution of a high power LD bar. A commercial water-cooled LD bar with multiple emitters is investigated to illustrate the proposed method. After introducing the LD bar system, an experimental setup that is developed uniquely to measure the average junction temperatures of the LD bar is described. Two parameters critical to thermal analysis – heat dissipation and effective heat transfer coefficient – are determined and subsequently used to predict the junction temperature distribution over the LD bar under high operating currents.

4.2. Laser Diode System

This section is devoted to the description and the electrical characteristics of a commercial water-cooled LD bar tested in the study.

4.2.1. LD Bar Description

The commercial LD bar system (E11.4N-940.10-150C-SO13.1: DILAS) is shown in Figure 4.1a. The LD bar consists of 23 identical GaAs emitters. The fill-

factor is 50%; each emitter is 200 μm wide and has a pitch of 400 μm. The maximum optical power at 160 A is 160 W with a center wavelength of 930 nm.

The close-up view of the side of the LD bar is shown in Figure 4.1b. The GaAs chip (the epi-down configuration) is mounted on a CuW submount using AuSn die attach. The submount made of W90Cu10 (6.5 ppm/°C) is placed between the GaAs chip (6.4 ppm/°C) and the water-cooled microchannel made of Cu (16.6 ppm/°C) for the heat spreader and for the stress-relieving buffer layer to reduce the thermal stress attributed to the mismatch in the coefficients of thermal expansion (CTE) between them [99-101]. The specified thermal resistance from the junction to water inlet temperature is approximately 0.3 K/W from the vendor [102]. The internal structures of the commercial microchannel and the interfacial resistance are not available, and thus the effective water heat transfer coefficient for this commercial microcooler cannot be determined.

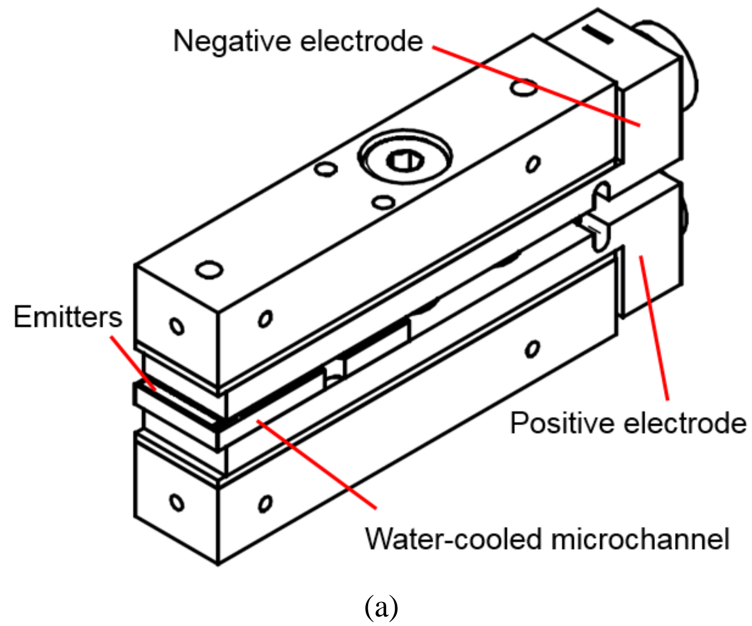

(a)

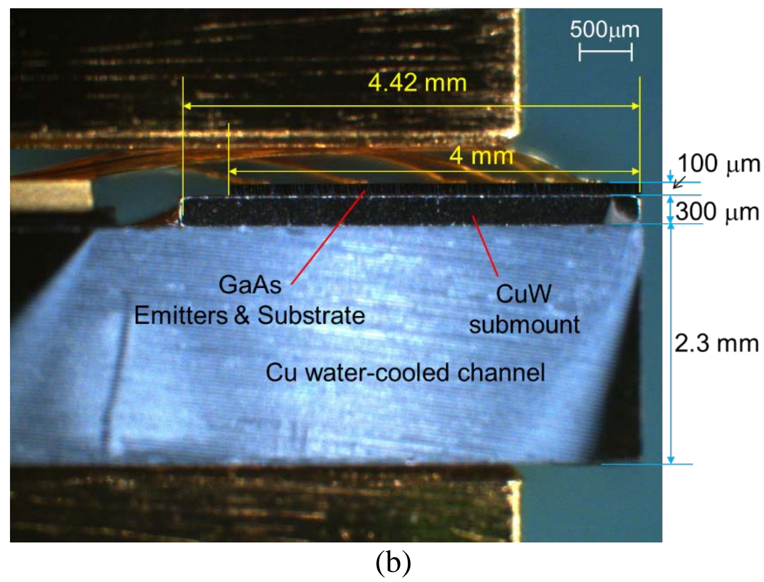

(b)

Figure 4.1. (a) LD bar with water-cooled microchannel [102] and (b) side view of the LD bar

4.2.2. Calibration Curve

It has been know that a negative linear relationship exists between the junction temperature and the forward voltage of a laser diode [46, 47, 53-58]. The junction temperature at the operating current can be measured using this relationship (known as the "calibration curve"), and it is called the forward voltage method [46, 47, 53-58].

The "calibration curve" is obtained using a probe current much lower than the operating current. If the probe current is too low, the forward voltage loses the negative linear relationship at high junction temperatures due to the leakage current effect [103]. On the other hand, if it is too high, the loss of linearity occurs at low junction temperatures due to the internal series resistance [104]. In addition, the probe current should be as low as possible to avoid any undesired junction temperature increase while obtaining the calibration curve. Every LD has somewhat different electrical characteristics. Thus, it is important to determine the lowest probe current that provides the desired linearity [47].

The LD bar was placed inside a convection oven (EC1A: Sun Electronics Systems) and the forward voltage was measured at 25, 35, 45, 55 and 65 °C (with an accuracy of ±0.1 °C) by a data acquisition module (DAQ: USB-6212: National Instruments) with a 16-bit resolution. The maximum operating junction temperature was estimated, based on the thermal resistance of 0.3 K/W, the inlet water temperature of 20 °C, and the maximum heat dissipation of 84.7 W, to be 45.4 °C. The calibration curve measurement was repeated at various probe current values (from 20 mA to 160 mA with an interval of 20 mA).

The results are shown in Figure 4.2, displaying the expected linear relationship between forward voltage and junction temperature. The small deviations from linearity in voltage and temperature at 65 °C are summarized in Table 4.1. The junction temperature error gradually decreased as the probe current increased, and remained virtually the same after 120 mA. The probe current of 120 mA generated a heat dissipation of only 142 mW (6.2 mW per emitter), which was negligible compared to the heat dissipation produced by the operating current. Thus, the calibration curve obtained at 120 mA was selected for junction temperature measurement. The slope and the y-intercept of the calibration curve were −1.21 mV/K and 1.2104 V, respectively.

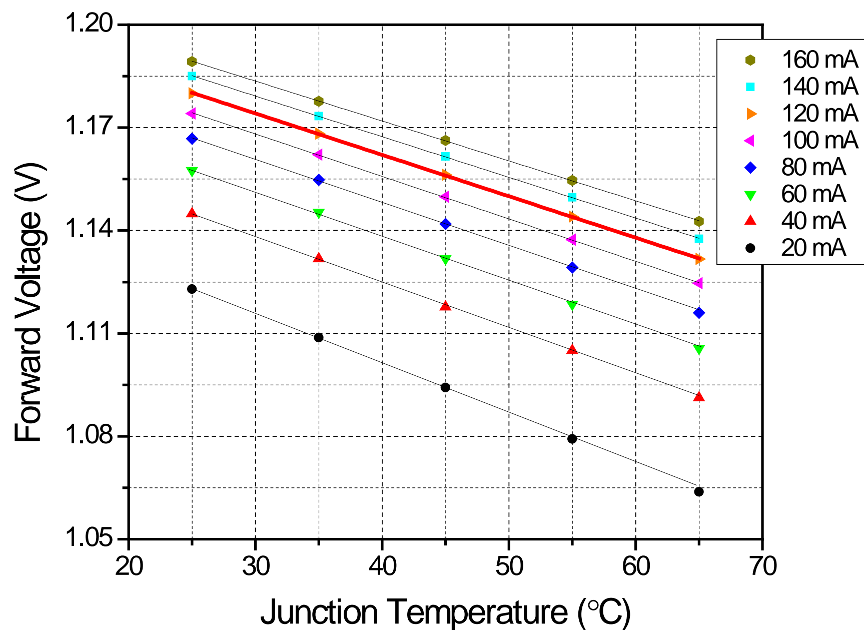

Figure 4.2. Forward voltage as a function of junction temperature

Table 4.1. Junction temperature error at different probe currents

I_f [mA]	Deviation of V_f (mV)	Error in T_j [°C]
160	0.17	0.1
140	0.16	0.1
120	0.18	0.1
100	0.41	0.3
80	0.78	0.6
60	0.80	0.7
40	0.80	0.7
20	1.60	1.3

4.2.3. Electrical Resistance of Single Emitter

The calibration curve is obtained when all the emitters have the same temperature. The emitters of the LD bar are connected in parallel, and thus the electrical resistance of a single emitter (assuming that all emitters are identical) can be determined simply by

$$R(T) = N \times \frac{V_f(T)}{I_{probe}} \tag{19}$$

where R is the electrical resistances of the single emitter [Ω]; V_f is the forward voltage of the LD bar [Ω] under the probe current, I_{probe}; and N is the number of the emitter (N = 23).

The results obtained for the LD bar under the current of $I_{probe} = 120$ mA are shown in Figure 4.3. The electrical resistance decreased with the temperature; the change in resistance was only 4% (from 226.2 Ω to 216.9 Ω) over the temperature range from 25 °C to 65 °C.

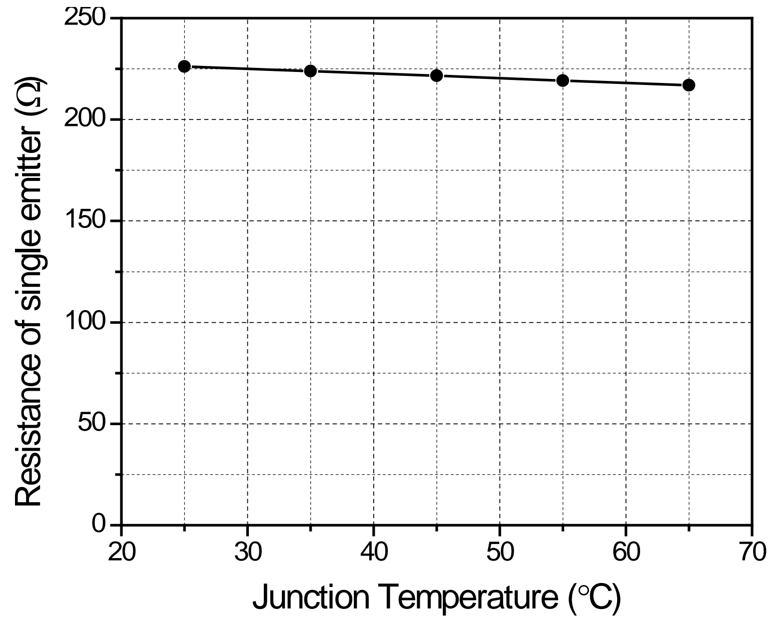

Figure 4.3. Electrical resistance of the single emitter as a function of junction temperature at $I_{probe} = 120$ mA.

4.3. Junction Temperature Measurement

The junction temperature at the operating current can be measured by switching the operating current to the probe current [46, 47, 53-58]. As discussed in Ref. [65], the forward voltage shows the combined behavior of RC delay and thermal delay during the switching time. The RC delay is attributed to the resistance of a LD and the capacitance of a current source.

The LD bar is operated at very high forward currents. A power supply that drives high currents typically has large capacitance, which can cause the large RC delay, and the transient junction temperature behavior of the CuW submount cannot be documented. Fast switching circuits with two separate power supplies have been utilized to reduce the delay [56, 57]. This scheme is adopted for the current study.

4.3.1. Test Setup

A test apparatus to minimize the RC delay is illustrated schematically in Figure 4.4. The operating current source (LDX-36125-12: ILX Lightwave) applies the operating current with a nominal accuracy of ±(0.1% + 120 mA). The probe current source (2401: Keithley Instruments) applies the probe current with a nominal accuracy of ±(0.066% + 20 μA). The two power supplies are connected in parallel.

An N-channel MOSFET (IRL7833PBF: International Rectifier Corporation) serves as a switch for the operating current source [56]. The probe current flows from the source (S) to the drain (D) of the N-channel MOSFET, even when the switch is off to block the operating current. A diode (150EBU02-ND: Vishay Intertechnology) is inserted between the operating current source and the MOSFET to prevent this undesired flow. The MOSFET and the diode are mounted on a heat sink to dissipate heat at high operating currents.

The chiller (ISOTEMP I 115V/60HZ PD-1: Fisher Scientific) regulates the water inlet temperature with a temperature stability of ±0.1 °C, and the flow regulator (FLDW3211G: OMEGA Engineering) controls the flow rate. The optical power sensor (USB-PM-150-50: Coherent Laser Group) measures the optical power with a nominal accuracy of ±2.7% in the operating range. The current sources, the DAQs, and the optical power sensor are integrated into a LabVIEW program.

In the actual measurements, the chiller is set to produce the inlet water temperature of 20 °C and the flow rate of 16 L/h. The pressure drop from the water-cooled microchannel cooler is 23 psi. The forward voltage measurement is conducted

only with the probe current applied to the LD bar. As an example, to apply an operating current of 80 A to the LD bar, the operating current source and the probe current source applies 79.88 A and 120 mA, respectively, with the MOSFET switch "on". When the optical power and the forward voltage of the LD reaches the steady-state condition, the switch is turned off to block the flow of the operating current. The data acquisition module 2 (DAQ2: USB-6212: National Instruments) supplies the gate voltage to the MOSFET switch and the data acquisition module 1 (DAQ1: USB-6212: National Instruments) measures the forward voltage of the LD with 16-bits resolution continuously during the transient period.

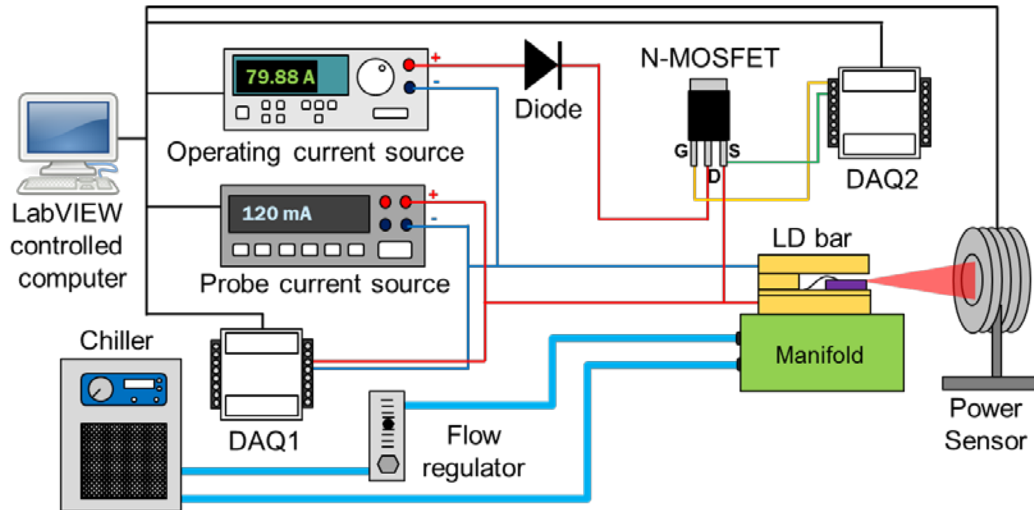

Figure 4.4. Schematic illustration of junction temperature measurement setup

4.3.2. Average Junction Temperature

As mentioned earlier, the junction temperatures of emitters can have large variations at high operating currents. However, only a single value for the entire LD

bar can be obtained from this setup. The following investigation is conducted to define the physical meaning of the measured value.

The emitters are connected in parallel, and thus the electrical resistance of the LD bar can be expressed as:

$$R_{\text{bar}}(T) = \frac{1}{\sum_{i=1}^{N} 1 / R_i(T_{j,i})} \tag{20}$$

where R_{bar} is the electrical resistance of the bar [Ω]; R_i and $T_{j,i}$ are the electrical resistance [Ω] and the temperature of the ith emitter [°C], respectively.

Let's consider a case where the junction temperature of the LD bar increases linearly from the edge to the center ($\Delta T = T_{center} - T_{edge}$). It is to be noted that the linear variation assumed in the analysis would be much worse than the actual temperature distribution over an LD bar. The average junction temperature of the LD bar can be expressed as $T_j^{ave} = \sum_{i=1}^{N} T_{j,i} \Big/ N$. Then, the measured forward voltage and the forward voltage estimated based on the average temperature can be expressed as:

$$V_f^{measured}(T) = R_{\text{bar}}(T) \times I_{prob} \;\; ; \;\; V_f^{ave}(T) = \frac{R(T_j^{ave}) \times I_{prob}}{N} \tag{21}$$

where $V_f^{measured}$ is the measured forward voltage of the LD bar [V]; V_f^{ave} and $R(T_j^{ave})$ are the forward voltage [V] and the electrical resistances [Ω] of the single emitter at the average temperature of the LD bar, respectively. The difference between these two values provides an estimate about how the measured junction temperature deviates from the average junction temperature of the bar. The deviation can be defined as:

$$\delta T_j = \frac{V_f^{measured} - V_f^{ave}}{1.21\times10^{-3}} \tag{22}$$

where δT_j is deviation of the measured junction temperature from the average junction temperature of LD bar [°C]; 1.21×10^{-3} is the slope of the calibration curve [V/K]. Figure 4.5 shows the deviation as a function of ΔT. The deviation is less 1 °C even for ΔT of 100 °C; the small change in resistance with the temperature (Figure 4.3) is attribute to this behavior. Consequently, the junction temperature determined from the forward voltage of the LD bar at the operating current can be considered as the average junction temperature of the LD bar if the junction temperature difference in the emitters is less than 100 °C in practice.

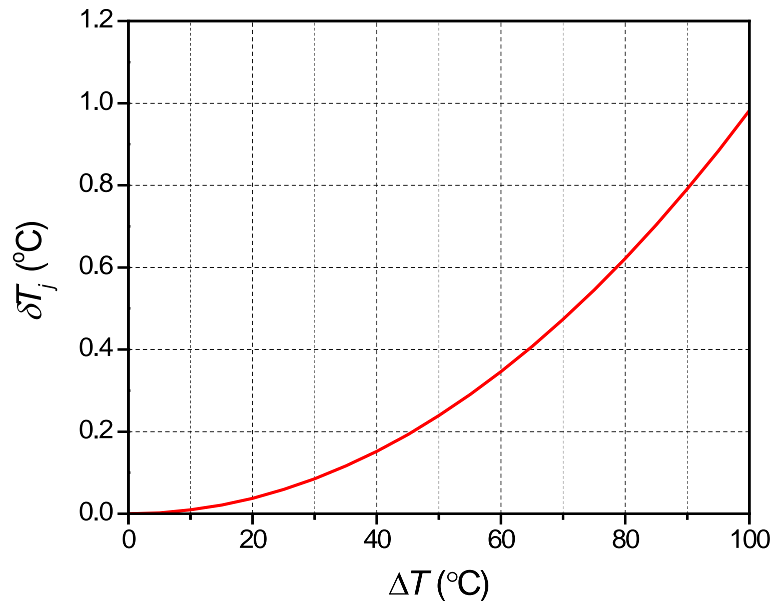

Figure 4.5. Deviation of the measured junction temperature of LD bar from the average junction temperature of LD bar with a linearly changing temperature of ΔT from the edge to the center

4.3.3. Average Junction Temperature Measurement

Figure 4.6 shows the transient voltage behavior of the LD bar obtained after blocking the operating current of 80 A. An extreme voltage peak at the beginning of transient behavior is clearly visible. It was produced by an inductor voltage attributed to the large rate of current change (79.88 A to zero) and the non-zero inductance of the LD [105, 106]. The peak was large but disappeared quickly after 200 μs.

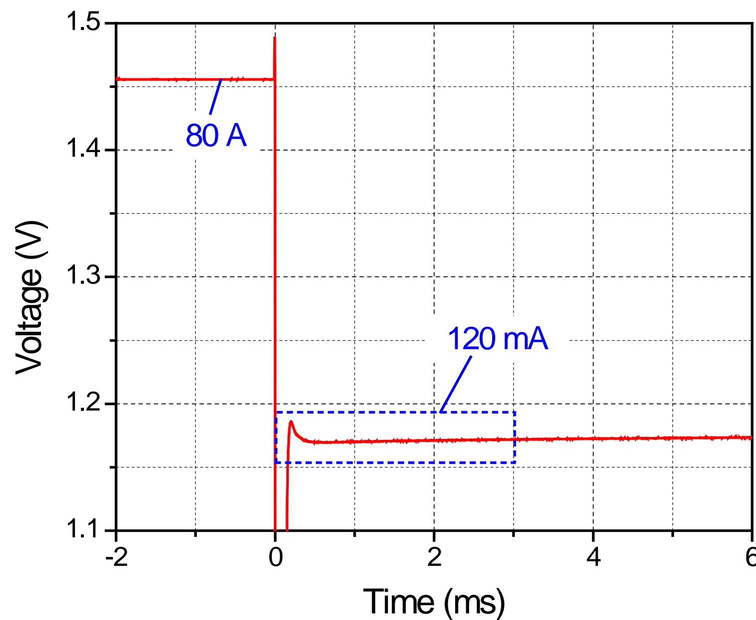

Figure 4.6. Transient voltage behavior of the LD bar obtained after blocking the operating current of 80 A

Based on theoretical analysis [30, 91-93], it is known that a junction temperature changes linearly in the square root of the time scale, if heat is dissipated in one direction through a homogenous material. In the case of this epi-down LD bar with the water-cooled microchannel cooler, the heat transfer through the GaAs substrate, and convection, as well as radiation, to the ambient surroundings is practically

negligible (less than 1% of the total) due to the extremely large heat transfer coefficient in the water-cooled microchannel cooler, which will be discussed in Section 4.4.1. Thus, the linear extrapolation in the square root time scale is applicable for the LD bar. The enlarged view of the region marked by a dashed box in Figure 4.6 is shown in Figure 4.7a. The voltage was converted into the temperature using the calibration curve (Figure 4.2) and it was plotted in the square root time scale (Figure 4.7b).

The transient junction temperature behavior can be divided into three zones. Zone 1 is the region dominated by the electrical delay. Zone 2 is the region where the linear junction temperature variation follows the square root time scale. When the propagating thermal wave reaches the microcooler interface, the transient junction temperature behavior of the submount vanishes and we enter Zone 3. It is estimated from Figure 4.7b that Zone 2 ends at t = 1.57 ms (= 1.25 $ms^{1/2}$). The following analytical analysis was conducted to confirm Zone 2.

The transient domain governed by the CuW submount can be calculated analytically using a time constant, which can be expressed as [31, 34]:

$$\tau_{th} = \frac{\rho c_p d^2}{K_s} \tag{23}$$

where τ_{th} is the thermal time constant [s]; d is the thickness along the heat transfer direction [m]; K_s is the thermal conductivity [W/m·K]; c_p is the specific heat [J/kg·K]; and ρ is the volumetric mass density [kg/m³]. Material properties, thickness, and the calculated thermal time constant of CuW are listed in Table 4.2. A thermal time constant value for the CuW is determined as 1.37 ms, which is defined as the heating or cooling time required to produce a temperature change at the heat source (junction)

equal to 63.2% of the total temperature difference between the initial and the final temperature. This value is reasonably close to the experimental observation, which confirms the validity of the experimental data.

The average junction temperature at the operating current was estimated from the linear extrapolation shown in Figure 4.7b; the estimated average junction temperature at 80 A was 35.6 °C. The discrepancy in the repeatability of the average junction temperature measurement was less than 0.1 °C, which is attributed to the probe current source inaccuracy.

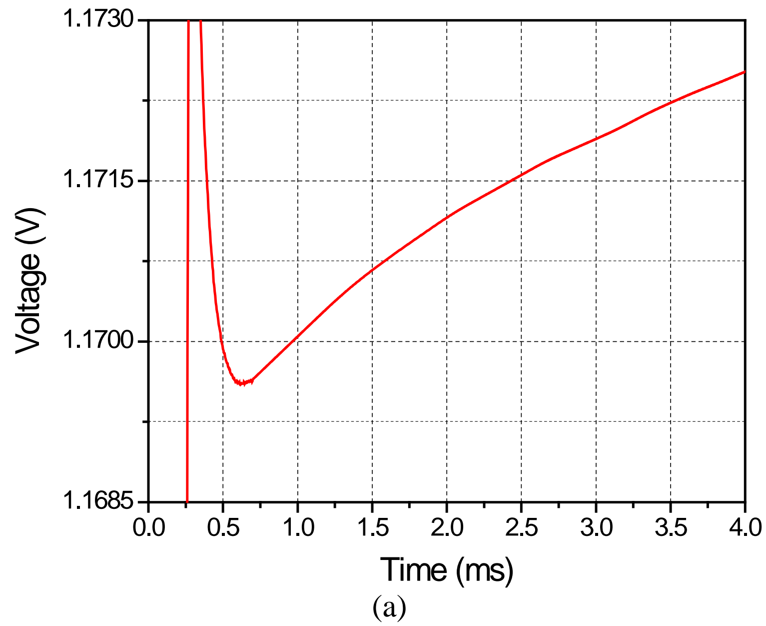

(a)

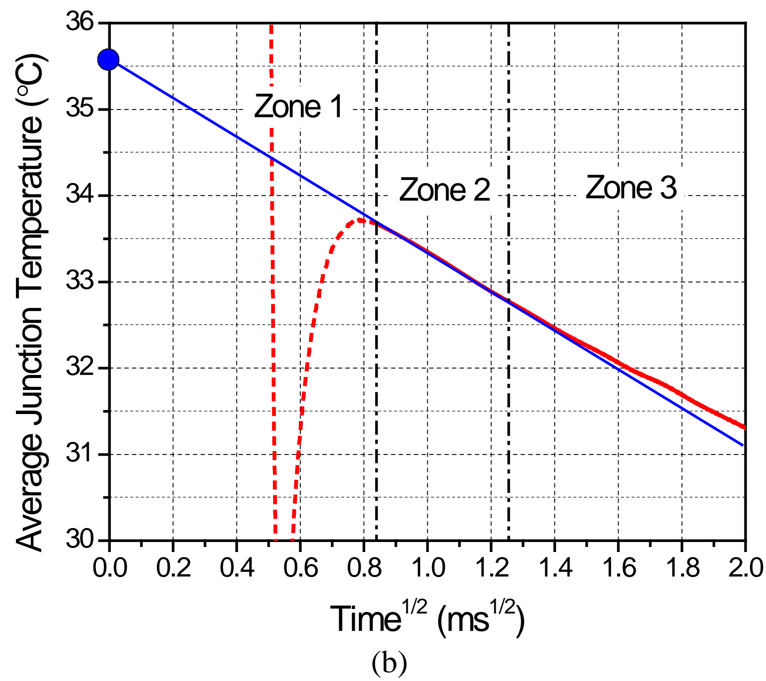

(b)

Figure 4.7. (a) Enlarged view of the region marked by a dashed box in Figure 4.6 and (b) Average junction temperature in the square root time scale; the linear extrapolation provides the estimated average junction temperature at the operating current

Table 4.2. Material properties, thickness, and calculated time constant used in the analytical solution [100, 101]

Material	Volumetric mass density (kg/m^3)	Specific heat (J/kg·K)	Conductivity (W/m·K)	Thickness (μm)	Time constant (ms)
W90Cu10	17300	160	200	300	1.37

The average junction temperatures were measured from 10 A to 80 A at an interval of 10 A. The results are shown in Figure 4.8. The connected lines between the measured data represent the trend of the results. As expected, the junction temperature increases with the current, but the rate starts to decrease around the threshold current (26 A), where the stimulated emission begins to occur; i.e., the higher wall-plug efficiency leads to the reduction of the heat dissipation as well as the junction temperature. The heat dissipation as a function of the forward current will be discussed further in Section 4.4.1.

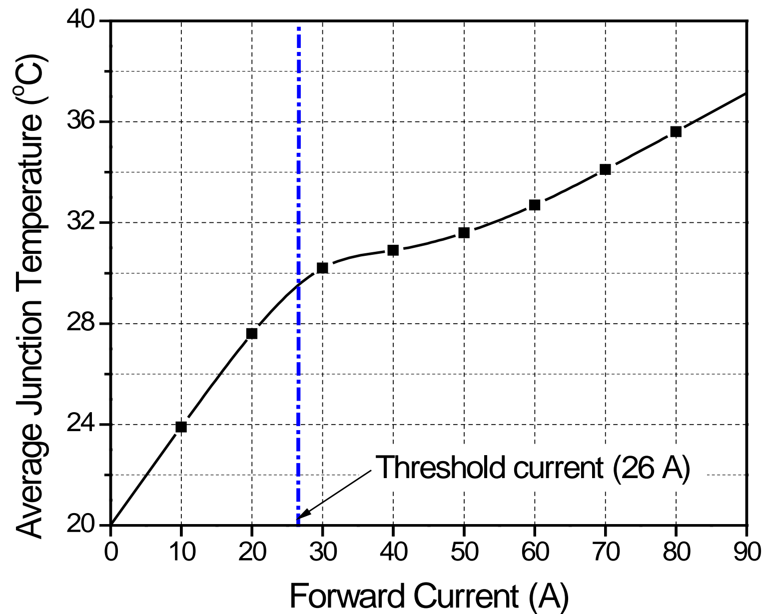

Figure 4.8. Average junction temperature at different forward currents

4.4. Heat Dissipation and Microcooler Effective heat transfer Coefficient

The forward voltage and the emitted radiant flux are measured to quantify the amount of heat dissipation, using the following relationship [44]:

$$P_h(T_j) = I_f \cdot V_f(T_j) - \Phi(T_j) \tag{24}$$

where P_h is the heat dissipation [W]; I_f is the forward current [A]; V_f is the forward voltage [V]; and Φ is the radiant flux [W]. After measuring the heat dissipation in Section 4.4.1, the effective heat transfer coefficient of the water-cooled microchannel is calculated inversely from the numerical simulation, using the measured average junction temperature and the heat dissipation in Section 4.4.2.

4.4.1. Measurement of Heat Dissipation

The DAQ1 measured the forward voltage of the LD bar and the optical power sensor measured the optical power (the radiant flux) continuously. When the optical power and the forward voltage of the LD reached the steady state condition, the values of forward voltage and optical power were recorded, from which the heat dissipation was calculated using Equation (24).

The forward voltages, electrical input power (product of the forward voltage and the forward current), optical powers, and heat dissipations were measured as a function of current with an interval of 10 A. The results are shown in Figure 4.9. The forward voltage and the electrical input power increases with the current. The optical power is virtually negligible before the threshold current (26 A) and increases linearly

with the operating current after the threshold current. Similar to the junction temperature, the heat dissipation increases with the current and the rate starts to decrease around the threshold current.

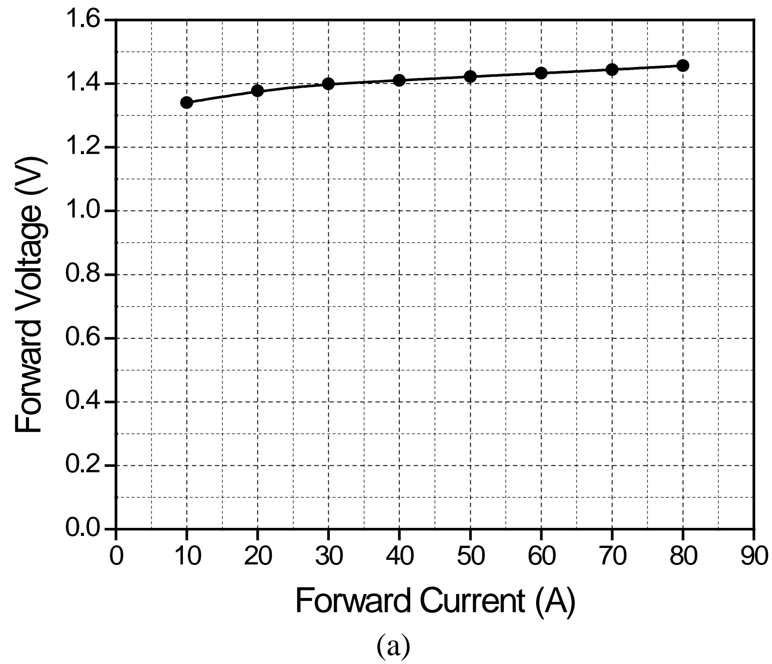

(a)

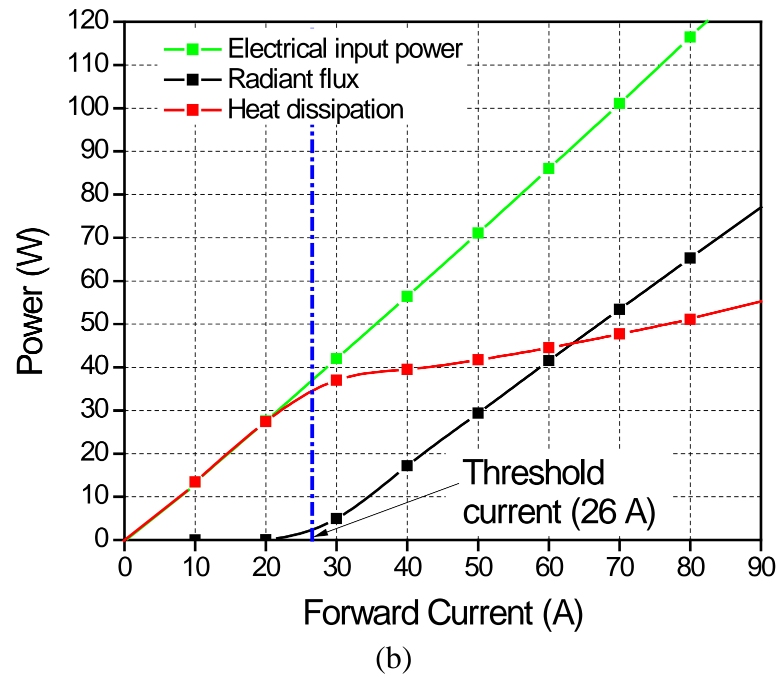

(b)

Figure 4.9. (a) Forward voltage and (b) electrical input power, radiant flux, and heat dissipation as a function of forward currents

The thermal resistances can be estimated by dividing the temperature difference between the average junction temperature (T_j^{ave}) and the inlet water temperature (T_{inlet} = 20 °C) by the heat dissipation. The average junction temperatures, the heat dissipations, and the calculated thermal resistances (R_{th}) are summarized in Table 4.3. The results showed a consistent thermal resistance of 0.295 K/W ±0.015 K/W for the all measured currents. The measurement uncertainty of the heat dissipation was mainly caused by the accuracy of the optical power sensor. The results confirm that the integrated commercial water-cooled microchannel is dominant in heat transfer regardless of the heat dissipation; i.e., the effect of the radiation and the natural convection (an approximated thermal resistance of 1134 K/W [22]) on heat transfer from the LD bar is negligible.

Table 4.3. Average junction temperature and thermal resistance estimations at different forward currents at 20 °C of the inlet water temperature

I_f [A]	10	20	30	40	50	60	70	80
P_h [W]	13.4 ± 0.3	27.4 ± 0.4	37.0 ± 0.7	39.2 ± 1.2	41.7 ± 1.6	44.5 ± 2.2	47.7 ± 2.7	51.1 ± 3.1
T_j^{ave} [°C]	23.8	27.6	30.2	30.9	31.6	32.7	34.1	35.6
T_j^{ave} - T_{inlet} [°C]	3.8	7.6	10.2	10.9	11.6	12.7	14.1	15.6
R_{th} [K/W]	0.28 ± 0.01	0.28 ± 0.01	0.28 ± 0.01	0.28 ± 0.01	0.28 ± 0.01	0.29 ± 0.01	0.30 ± 0.02	0.31 ± 0.02

4.4.2. Effective Heat Transfer Coefficient

The numerical model (ANSYS 16.1) used in the current analysis is shown in Figure 4.10. The model has the same geometry as the LD bar (23 emitters; emitter

width of 200 μm and the fill-factor of 50%, i.e., the pitch of 400 μm). A metallization layer (Ti/Pt/Au) layer between the emitter and the AuSn solder was not considered in the model due to the ignorable thermal resistance attributed to the thin (about 2 -3 μm) and the high thermal conductivity (315 W/m·K for Au) [10]. The values of thermal conductivity of GaAs, CuW submount, and AuSn solder taken around 300 K and used in the analysis are 54 W/m·K [107], 200 W/m·K [100, 101], and 58 W/m·K [108], respectively.

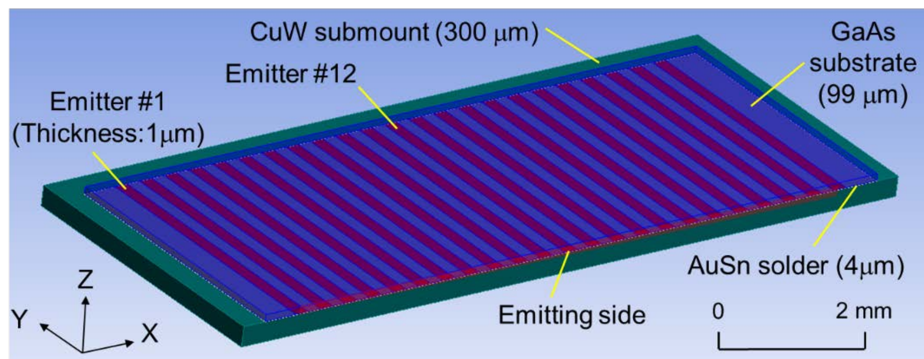

Figure 4.10. 3D model

The ambient temperature was set at 20 °C (the same as the inlet water temperature). The effective heat transfer coefficients for natural convection (5 W/m^2·K) and radiation (GaAs emissivity of 0.62 [109], yielding an effective heat transfer coefficient of 3.89 W/m^2·K [22]) were set on the top and the sides of the model, albeit with the expectation of negligible effects on the junction temperature. The effective heat transfer coefficient of the water-cooled microchannel cooler was assumed to be uniform on the bottom of the CuW submount.

It is important to note that Equation (24) is applicable only when the junction temperature is uniform. In addition, the uniform heat dissipation would be desired to determine the effective heat transfer coefficient most accurately. Thus, the lowest operating current (10 A) was used to calculate the effective heat transfer coefficient.

The heat dissipation obtained in the previous section was applied uniformly on the emitters, and then, the effective heat transfer coefficient was adjusted until the difference between the measured average junction temperature and the numerically calculated average junction temperature reached its minimum value. The average junction temperature difference, after typically 5 iterations, was less than 0.1 °C, and the resulting effective heat transfer coefficient was found to equal 98 kW/m^2K.

The junction temperature distribution at 20 A was also calculated to validate the effective heat dissipation. The difference between the average junction temperatures (experimental and numerical) was less than 0.1 °C, which confirmed the validity of the effective heat dissipation.

4.5. Numerical Prediction of Junction Temperature Distribution

It is important to understand the effect of the junction temperature on the heat dissipation before performing numerical analyses at high operating currents because Equation (24) is applicable only when the junction temperature is uniform. The heat dissipation at 80 A was measured with three inlet water temperatures (10, 15, and 20 °C). The junction temperature at each inlet temperature was also measured, and the results are summarized in Table 4.4.

Table 4.4. Heat dissipation at 80A under different inlet water temperatures

T_{inlet} [°C]	10	15	20
T_j^{ave} [°C]	25.6	29.2	35.6
V_f [V]	1.458	1.457	1.456
$I_f \cdot V_f$ [W]	116.66	116.58	116.46
Φ [W]	67.80	66.85	65.34
P_h [W]	48.9	49.7	51.1

As the average junction temperature increased from 25.6 to 35.6 °C, the forward voltage as well as the radiant flux decreased. The forward voltage reduction reduced the total electrical power consumption, while the radiant flux reduction increased the fraction of the input power converted to heat. It is worth noting that the net heat dissipation increased only by 2.2 W (or 4%) corresponding to the junction increase of 0.6 °C, as the two parameters compensated their effects on heat dissipation [66]. The results indicate that the junction temperature dependency on the heat generation, over a range of 10 °C, is not significant, which provides a technical rationale for the following numerical study.

4.5.1. Temperature Distribution in LD Bar

The junction temperature distribution of the LD bar at 80 A is shown in Figure 4.11a. The GaAs substrate is not present in order to clearly show the temperature distribution of the emitters. The highest temperature occurs at the emitting side of the center emitter and the lowest temperature is observed at the opposite side of the edge emitter. The junction temperature drop toward the edge emitter and the back end is attributed to the effect of the hear spreader. Because the edge emitter and the back end have cooling area enhancement from the CuW submount, the more heat could be

dissipated due to the extra heat spreading. The maximum temperature difference is 10.1 °C. This result confirms that the application of uniform heat dissipation across all the emitters in a multi-emitter LD bar can be expected to provide acceptable numerical results for input current of up to 80A.

The average junction temperature obtained from the numerical model for this 80A input current is 34.8 °C, which is smaller than the measured average junction temperature by 0.8 °C. The difference lies within the measurement uncertainty of the forward voltage methodology. The close agreement in average junction temperature between the numerical and experimental values corroborates the accuracy of the numerical analysis, even at this high operating current.

The junction temperature distribution was also calculated at the operating current of 160 A. Since the test apparatus was only capable of providing 125 A, an additional power supply (N5744A; Keysight Technologies) was connected to the operating current source in parallel to provide the additional current of 35 A. The forward voltage and the optical power at 160 A were 1.544 V and 162.4 W, respectively, and the heat dissipation was 84.7 W (65.7% of the wall-plug efficiency). It is to be noted that the average junction temperature could not be measured at 160 A because the threshold current of the MOSFET switch was around 90 A.

The junction temperature distribution of the LD bar at 160 A is shown in Figure 4.11b. The highest and lowest temperatures were 47.9 °C and 31.7 °C; the junction temperature difference was 16.2 °C.

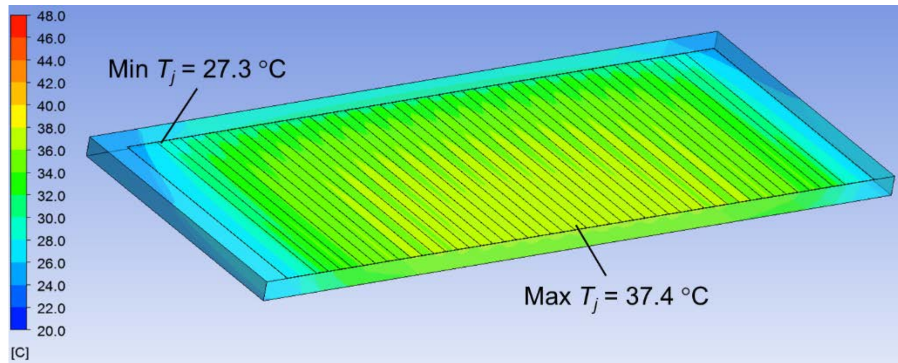

(a)

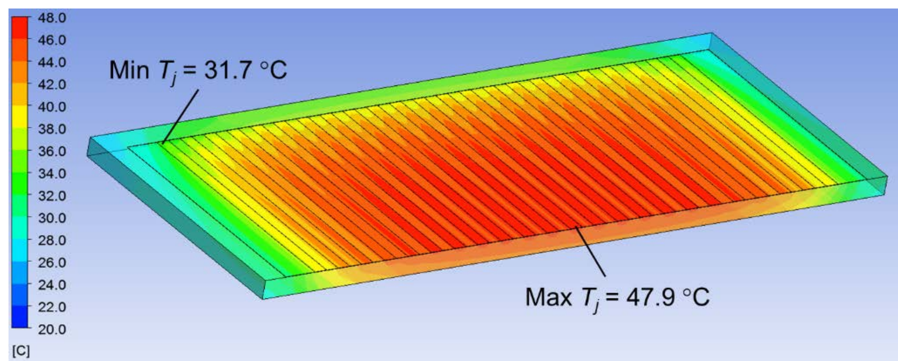

(b)

Figure 4.11. Temperature distribution of the LD bar at (a) 80 A and (b) 160 A

The average junction temperature of each emitter are compared in Figure 4.12, where the only left half is shown due to the symmetry. The average junction temperatures remained virtually unchanged over the center half of emitters (from #12 to #7) and then rapidly dropped toward the edge emitter. The maximum average junction temperature difference among the 12 emitters was 4.9 °C and 7.8 °C at 80 A and 160 A, respectively.

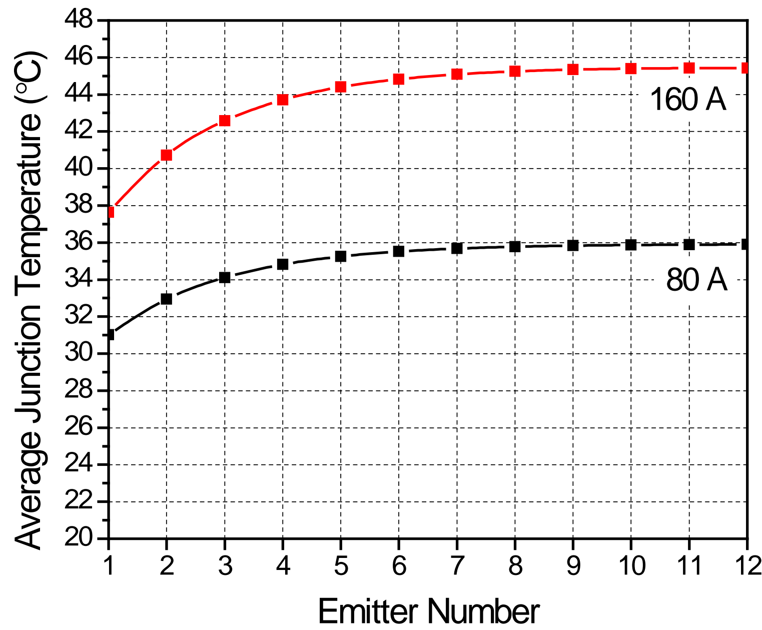

Figure 4.12. Average junction temperature of each emitter

The front-to-back junction temperature variations within the center (#12) and the edge (#1) emitter are plotted in Figure 4.13. The junction temperature decreased exponentially from the emitting side to the back end. The junction temperature variations within the emitter were largest at the center emitter and the magnitude increased as the operating current increased. The junction temperature variations of the center emitter were 5.4 °C and 8.7 °C for 80 A and 160 A, respectively.

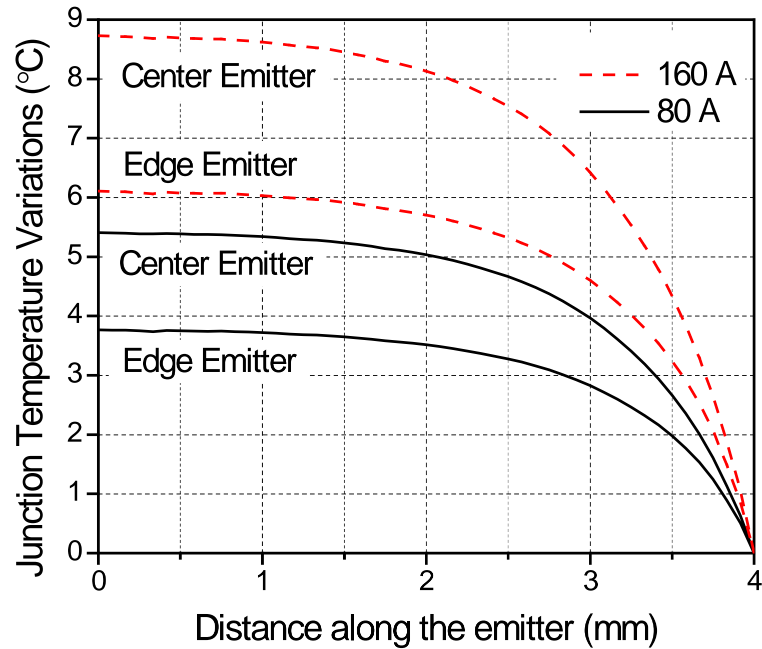

Figure 4.13. Junction temperature variations along the emitter

4.5.2. Wall-plug Efficiency and Center Wavelength Shift

The junction temperature change affects the wall-plug efficiency, which is defined as the optical output power divided by the electrical input power. Each emitter of the LD bar tested in the study produced about an optical power of 7.06 W at the operating current of 6.95 A (the LD bar with 23 emitters at the operating current of 160 A).

Based on Ref. [110], a single emitter producing 6 W at 6A with a center wavelength of 975 nm showed that the wall-plug efficiency increased only about 3% from 275 K (71%) to 260 K (74%). Thus, it is reasonable to assume that each emitter of the LD bar tested in the study has similar behavior to that of the single emitter

reported in Ref. [110], and consequently, the effect of the junction temperature distribution on the wall-plug efficiency is not significant.

Spectral power distribution (SPD) at 160 A is shown in Figure 4.14. It has a peak wavelength at 932.5 nm and full width at half maximum (FWHM) of 2 nm. LDs show the spectral red shift at higher junction temperatures due to the reduced band gap energy [45]. The spectral red shift caused by the junction temperature has been reported to be 0.28 nm/K [111] and 0.32 nm [112] for 808 nm and 980 nm LDs, respectively. The SPD shows the broadened spectrum to the lower wavelength (asymmetric) due to the junction temperature distribution.

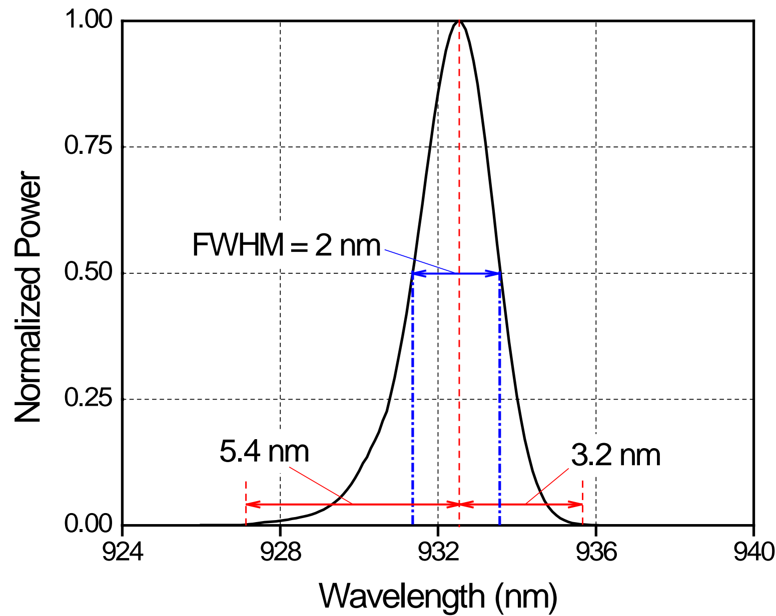

Figure 4.14. Normalized SPD at 160 A [102]

The analysis was based on a very large heat transfer coefficient. In practice, various thermal solutions can be employed for cooling the LD bar. In terms of the coefficient of performance (COP), the lower heat transfer coefficients can reduce the operating costs. However, the temperature rise and the temperature variation within the LD bar will increase with lower heat transfer coefficients. This will increase the asymmetry of the SPD and the peak wavelength shift, which can reduce the pumping efficiency [10].

A high heat transfer coefficient is desired to increase the pumping efficiency, which can be achieved with an extreme flow rate of a coolant. However, the higher flow rate reduce the COP, which increases the operating cost. In addition, it can accelerate the erosion process of the surface structures inside microchannels, which will increase the junction temperature and will eventually reduce the lifetime of the LD bar [113, 114].

Consequently, optimization of thermal solutions for high power LD bars should be sought while considering the operating cost as well as various thermal, mechanical, and optical aspects of the system. The future work will address a methodology to define the optimum design of LD bars considering the COP, performance, and reliability.

4.6. Conclusions

A hybrid experimental and numerical method was proposed for predicting the junction temperature distribution of a high power, multiple-emitter LD bar. A commercial water-cooled LD bar was utilized to illustrate and validate the proposed method. The average junction temperature and the heat dissipation were measured, and

the effective heat transfer coefficient of the cooling system was determined inversely using numerical simulation. The characterized properties were used to predict the junction temperature distributions of the LD bar at the extreme operating currents. The results showed significant junction temperature variations not only among emitters (7.8 °C) but also along each emitter (8.7 °C) at 160A, which increased the asymmetry of the SPD.

Chapter 5: Contributions and Future Works

5.1. Thesis Contributions

Thermal issues related to the high power LEDs and LDs were investigated in this dissertation. The most significant contributions are summarized below:

a) The advanced inverse approach was proposed and implemented to determine the resistance of the DTI in the high power LEDs. The proposed approach considered the spreading resistance from the numerical simulation and offered a measurement accuracy of 0.01 K/W for various types of die-attach materials. With the high accuracy offered by the proposed approach, the die bonding manufacturing process can be evaluated non-destructively.

b) The effect of the junction temperature dependency on the heat dissipation was investigated. The theoretical review confirmed that the forward voltage reduction at higher junction temperatures compensated the heat dissipation that was increased by the radiant flux reduction. Actual measurements of the heat dissipation over a wide range of the junction temperatures showed that (1) the effect of the junction temperature dependency on the heat dissipation was governed largely by the power efficiency and (2) the compensation effect was so strong that the absolute changes of the heat dissipation were not significant over the junction temperature range from 25 °C to 200 °C. Due to the small temperature dependency of phosphor heat generation, the heat dissipation of pc-LEDs was also confirmed to be virtually the same regardless of the junction temperature. Based on these

results, the empirical heat dissipation model that was only a function of the forward current was proposed. The model requires the heat dissipation data only at two currents but can accurately estimate the heat dissipation at any forward current (and at any temperatures).

c) The hybrid experimental and numerical method was proposed and implemented to predict the junction temperature distribution of the high power LD bar. The average junction temperature and the heat dissipation were measured, and the effective heat transfer coefficient of the cooling system was determined inversely using numerical simulation. The characterized properties were used to predict the junction temperature distributions of the LD bar at two extreme operating currents. The results showed significant junction temperature variations not only among emitters but also along each emitter. This is the first attempt to predict the junction temperature distribution of the high power LD bar. The proposed hybrid junction temperature distribution measurement of the high power LD bar can be utilized to optimize parameters for maximum efficiency and lifetime, to conduct quality control, and/or to incorporate diagnostics/prognostics.

5.2. Future Works

The thermal characterization and reliability issues of the high power LDs will become increasingly important to achieve optimal performance. The contributions by this dissertation can be extended in several directions. Some of them are described below:

Prediction and optimization of SPD of high power LD bar

The non-uniform junction temperature of emitters in the high power LD bar means that the SPD of each emitter has different center wavelengths as the bandgap energy is reduced at higher temperatures. Through the SPD deconvolution scheme [115], the SPD of each emitter can be predicted. This results can be used to predict the SPD of the LD bar at different conditions after predicting the temperature distribution through the proposed hybrid experimental/numerical method. This result can be also utilized to optimize spectrum by controlling the number, pitch, and fill-factor of emitters as well as considering thermal and mechanical aspects of the system for applications.

Reliability assessment of high power LD bar

As higher optical power is demanded for advanced applications, junction temperature increases and large variations of emitters become more significant. The packaging induced stress caused by the CTE mismatch between a chip, a substrate, and a heat sink as well as the junction temperature variations of emitters can lead to the different reliability of the emitters. Various photo-mechanics tools [116] can provide quantitative measurements of in-plane or out-of-plane displacement to evaluate the stress distributions. Thermal and mechanical models can be developed to predict thermo-mechanical stresses of the subassembly, and thus to assess reliability of high power LD bars.

Reference

[1] E. F. Schubert, J. K. Kim, H. Luo, and J. Q. Xi, "Solid-state lighting - a benevolent technology," *Reports on Progress in Physics,* vol. 69, pp. 3069-3099, 2006.

[2] S. Pimputkar, J. S. Speck, S. P. DenBaars, and S. Nakamura, "Prospects for LED lighting," *Nature Photonics,* vol. 3, pp. 180-182, 2009.

[3] R. V. Steele, "The story of a new light source," *Nature Photonics,* vol. 1, pp. 25-26, 2007.

[4] E. F. Schubert, *Light-Emitting Diodes*, 2nd ed. New York: Cambridge University Press, 2006.

[5] J.-L. Boulnois, "Photophysical processes in recent medical laser developments: a review," *Lasers in Medical Science,* vol. 1, pp. 47-66, 1986.

[6] F. Bachmann, P. Loosen, and R. Poprawe, *High Power Diode Lasers: Technology and Applications*: Springer New York, 2007.

[7] M. Montealegre, G. Castro, P. Rey, J. Arias, P. Vázquez, and M. González, "Surface treatments by laser technology," *Comtemporary Materials, I–1,* pp. 19-30, 2010.

[8] A. D. McAulay, *Military Laser Technology for Defense: Technology for Revolutionizing 21st Century Warfare*: Wiley, 2011.

[9] S. P. Najda, P. Perlin, T. Suski, L. Marona, M. Boćkowski, M. Leszczyński, P. Wisniewski, R. Czernecki, R. Kucharski, G. Targowski, S. Watson, and A. E. Kelly, "Advances in AlGaInN laser diode technology for defence applications," in *Proc. SPIE 8899, Emerging Technologies in Security and Defence; and Quantum Security II; and Unmanned Sensor Systems X,* , pp. 88990B-1-7, 2013.

[10] H. Liu, X. Liu, L. Xiong, and W. Zhao, *Packaging of High Power Semiconductor Lasers*: Springer, 2014.

[11] S. P. Najda, P. Perlin, T. Suski, L. Marona, M. Boćkowski, M. Leszczyński, P. Wisniewski, R. Czernecki, R. Kucharski, G. Targowski, S. Watson, and A. E. Kelly, "AlGaInN laser diode technology for defence, security and sensing applications," in *Proc. SPIE 9254, Emerging Technologies in Security and Defence II; and Quantum-Physics-based Information Security III*, pp. 92540Z-1-7, 2014.

[12] X. A. Cao, S. F. LeBoeuf, L. B. Rowland, C. H. Yan, and H. Liu, "Temperature-dependent emission intensity and energy shift in InGaN/GaN multiple-quantum-well light-emitting diodes," *Applied Physics Letters,* vol. 82, pp. 3614-3616, 2003.

[13] L. Trevisanello, M. Meneghini, G. Mura, M. Vanzi, M. Pavesi, G. Meneghesso, and E. Zanoni, "Accelerated life test of high brightness light emitting diodes," *IEEE Transactions on Device and Materials Reliability,* vol. 8, pp. 304-311, 2008.

[14] C.-P. Wang, T.-T. Chen, H.-K. Fu, T.-L. Chang, P.-T. Chou, and M.-T. Chu, "Analysis of thermal characteristics and mechanism of degradation of flip-chip high power LEDs," *Microelectronics Reliability,* vol. 52, pp. 698-703, 2012.

[15] H. J. Yi, J. Diaz, I. Eliashevich, M. Stanton, M. Erdtmann, X. He, L. J. Wang, and M. Razeghi, "Temperature dependence of threshold current density Jth and differential efficiency ηd of high-power InGaAsP/GaAs (λ=0.8 μm) lasers," *Applied Physics Letters,* vol. 66, pp. 253-255, 1995.

[16] H. J. Yoon, N. J. Chung, M. H. Choi, I. S. Park, and J. C. Jeong, "Reliability performance for InGaAsP/InP laser diodes mounted on different sizes of heat blocks in to packages," *Solid-State Electronics,* vol. 42, pp. 1969-1974, 1998.

[17] J. Wang, L. Bao, M. DeVito, D. Xu, D. Wise, M. Grimshaw, W. Dong, S. Zhang, C. Bai, P. Leisher, D. Li, H. Zhou, S. Patterson, R. Martinsen, and J. Haden, "Reliability and Performance of 808nm Single Emitter Multi-Mode Laser Diodes," *High-Power Diode Laser Technology and Applications Viii,* vol. 7583, 2010.

[18] K. Matin, Z. Yan, and A. Bar-Cohen, "Numerical modeling and simulation of laser diode diamond microcoolers," in *Thermal and Thermomechanical Phenomena in Electronic Systems (ITherm), 2014 IEEE Intersociety Conference on*, pp. 59-63, 2014.

[19] J. Zhu, T. Yang, C. Zhang, C. Lang, X. Jiang, R. Liu, Y. Gao, W. Guo, Y. Jiang, Y. Liu, L. Zhang, and L. Chen, "Reliability Study of High Brightness Multiple Single Emitter Diode Lasers," *High-Power Diode Laser Technology and Applications Xiii,* vol. 9348, pp. 93480J-1-12, 2015.

[20] H.-H. Kim, S.-H. Choi, S.-H. Shin, Y.-K. Lee, S.-M. Choi, and S. Yi, "Thermal transient characteristics of die attach in high power LED PKG," *Microelectronics Reliability,* vol. 48, pp. 445-454, 2008.

[21] B. Pardo, A. Gasse, A. Fargeix, J. Jakovenko, R. J. Werkhoven, X. Perpina, X. Jorda, M. Vellvehi, T. Van Weelden, and P. Bancken, "Thermal resistance

investigations on new leadframe-based LED packages and boards," *Microelectronics Reliability,* vol. 53, pp. 1084-1094, 2013.

[22] B. Han, C. Jang, A. Bar-Cohen, and B. Song, "Coupled Thermal and Thermo-Mechanical Design Assessment of High Power Light Emitting Diode," *IEEE Transactions on Components and Packaging Technologies,* vol. 33, pp. 688-697, 2010.

[23] D. Yang, Y. C. Chan, B. Y. Wu, and M. Pecht, "Electromigration and thermomigration behavior of flip chip solder joints in high current density packages," *Journal of Materials Research,* vol. 23, pp. 2333-2339, 2008.

[24] R. Prasher, "Thermal interface materials: Historical perspective, status, and future directions," *Proceedings of the Ieee,* vol. 94, pp. 1571-1586, 2006.

[25] M. Montano, J. Garcia, W. Shi, M. T. Reiter, U. Vadakkan, K. L. Phillippe, B. Clark, M. Valles, C. Deppisch, J. D. Ferrara-Brown, S. G. Jadhav, E. Bernal, M. K. Kuan, and Asme, "Novel process techniques to reduce voids in solder thermal interface materials used for flip-chip package applications," in *ASME 2005 Summer Heat Transfer Conference*, pp. 2369-2374, 2005.

[26] D.-S. Kim, Q. Yu, T. Shibutani, N. Sadakata, and T. Inoue, "Effect of void formation on thermal fatigue reliability of lead-free solder joints," in *Thermal and Thermomechanical Phenomena in Electronic Systems, 2004. ITHERM '04. The Ninth Intersociety Conference*, pp. 325-329 Vol.2, 2004.

[27] K. C. Otiaba, R. S. Bhatti, N. N. Ekere, S. Mallik, E. H. Amalu, and M. Ekpu, "Thermal effects of die-attach voids location and style on performance of chip level package," in *Adaptive Science and Technology (ICAST), 3rd IEEE International Conference*, pp. 231-236, 2011.

[28] R. O. Carlson, A. J. Yerman, J. F. Burgess, and C. A. Neugebauer, "Voids, Cracks, and Hot Spots in Die Attach," in *Reliability Physics Symposium, 21st Annual*, pp. 138-141, 1983.

[29] A. S. Fleischer, L.-h. Chang, and B. C. Johnson, "The effect of die attach voiding on the thermal resistance of chip level packages," *Microelectronics Reliability,* vol. 46, pp. 794-804, 2006.

[30] EIA/JEDEC, "Transient Dual Interface Test Method for the Measurement of the Thermal Resistance Junction to Case of Semiconductor Devices with Heat Flow Through a Single Path," *JESD51-14,* p. 46, 2010.

[31] Q. Shan, Q. Dai, S. Chhajed, J. Cho, and E. F. Schubert, "Analysis of thermal properties of GaInN light-emitting diodes and laser diodes," *Journal of Applied Physics,* vol. 108, pp. 084504-1-8, Oct 15 2010.

[32] P. Szabo, A. Poppe, and M. Rencz, "Studies on the Possibilities of In-Line Die Attach Characterization of Semiconductor Devices," in *Electronics Packaging Technology Conference, EPTC. 9th*, pp. 779-784, 2007.

[33] M. R. Rencz and V. Szekely, "Measuring partial thermal resistances in a heat-flow path," *IEEE Transactions on Components and Packaging Technologies,* vol. 25, pp. 547-553, 2002.

[34] V. Szekely, "A new evaluation method of thermal transient measurement results," *Microelectronics Journal,* vol. 28, pp. 277-292, 1997.

[35] V. Szekely, "Identification of RC networks by deconvolution: chances and limits," *IEEE Transactions on Circuits and Systems I: Fundamental Theory and Applications,* vol. 45, pp. 244-258, 1998.

[36] A. Vass-Varnai, J. Parry, G. Toth, S. Ress, G. Farkas, A. Poppe, and M. Rencz, "Comparison of JEDEC dynamic and static test methods for the thermal characterization of power LEDs," in *Electronics Packaging Technology Conference (EPTC), IEEE 14th*, pp. 594-597, 2012.

[37] M. Rencz and V. Szekely, "Structure function evaluation of stacked dies," presented at the 20th Annual IEEE Semiconductor Thermal Measurement and Management Symposium, pp. 50-54, 2004.

[38] D. L. Saums, *Advances in Thermal Interface Materials for Power LED Applications* vol. 2: Springer New York, 2014.

[39] M. Y. Tsai, C. H. Chen, and C. S. Kang, "Thermal measurements and analyses of low-cost high-power LED packages and their modules," *Microelectronics Reliability,* vol. 52, pp. 845-854, 2012.

[40] Y.-F. Su, S.-Y. Yang, T.-Y. Hung, C.-C. Lee, and K.-N. Chiang, "Light degradation test and design of thermal performance for high-power light-emitting diodes," *Microelectronics Reliability,* vol. 52, pp. 794-803, 2012.

[41] M. Ha and S. Graham, "Development of a thermal resistance model for chip-on-board packaging of high power LED arrays," *Microelectronics Reliability,* vol. 52, pp. 836-844, May 2012.

[42] H. H. Cheng, D.-S. Huang, and M.-T. Lin, "Heat dissipation design and analysis of high power LED array using the finite element method," *Microelectronics Reliability,* vol. 52, pp. 905-911, 2012.

[43] S.-J. Wu, H.-C. Hsu, S.-L. Fu, and J.-N. Yeh, "Numerical simulation of high power LED heat-dissipating system," *Electronic Materials Letters,* vol. 10, pp. 497-502, 2014.

[44] Y.-J. Lee, C.-J. Lee, and C.-H. Chen, "Determination of Junction Temperature in InGaN and AlGaInP Light-Emitting Diodes," *IEEE Journal of Quantum Electronics,* vol. 46, pp. 1450-1455, 2010.

[45] Y. P. Varshni, "Temperature dependence of the energy gap in semiconductors," *Physica,* vol. 34, pp. 149-154, 1967.

[46] Y. Xi and E. F. Schubert, "Junction-temperature measurement in GaN ultraviolet light-emitting diodes using diode forward voltage method," *Applied Physics Letters,* vol. 85, pp. 2163-2165, 2004.

[47] A. Keppens, W. R. Ryckaert, G. Deconinck, and P. Hanselaer, "High power light-emitting diode junction temperature determination from current-voltage characteristics," *Journal of Applied Physics,* vol. 104, pp. 093104-1-8, 2008.

[48] C. Huh, W. J. Schaff, L. F. Eastman, and P. Seong-Ju, "Temperature dependence of performance of InGaN/GaN MQW LEDs with different indium compositions," *Electron Device Letters, IEEE,* vol. 25, pp. 61-63, 2004.

[49] H. K. Lee, J. S. Yu, and Y. T. Lee, "Thermal analysis and characterization of the effect of substrate thinning on the peformances of GaN-based light emitting diodes," *physica status solidi (a),* vol. 207, pp. 1497-1504, 2010.

[50] S. Murata and H. Nakada, "Adding a heat bypass improves the thermal characteristics of a 50 μm spaced 8-beam laser diode array," *Journal of Applied Physics,* vol. 72, pp. 2514-2516, 1992.

[51] B. Siegal, "Practical Considerations in High Power LED Junction Temperature Measurements," in *Electronics Manufacturing and Technology, 31st International Conference on*, pp. 62-66, 2006.

[52] A. Kozlowska and A. Malag, "Investigations of transient thermal properties of conductively cooled diode laser arrays operating under quasicontinuous-wave conditions," *Microelectronics Reliability,* vol. 46, pp. 2079-2084, 2006.

[53] H. Y. Ryu, K. H. Ha, J. H. Chae, O. H. Nam, and Y. J. Park, "Measurement of junction temperature in GaN-based laser diodes using voltage-temperature characteristics," *Applied Physics Letters,* vol. 87, pp. 093506-1-3, 2005.

[54] J. Kim, H. Park, S. Kim, H. Jeong, K. Lee, J. H. Yi, Y. Choi, S. Jung, and M. Noh, "Temperature Dependent Thermal Properties of a GaN-based Laser Diode Analyzed by an Electrical Method," *AIP Conference Proceedings,* vol. 1399, pp. 99-100, 2011.

[55] M. X. Feng, S. M. Zhang, D. S. Jiang, J. P. Liu, H. Wang, C. Zeng, Z. C. Li, H. B. Wang, F. Wang, and H. Yang, "Thermal characterization of GaN-based laser

diodes by forward-voltage method," *Journal of Applied Physics,* vol. 111, pp. 094513-1-4, 2012.

[56] Y. Qiao, S. Feng, C. Xiong, X. Ma, H. Zhu, C. Guo, and G. Wei, "The thermal properties of AlGaAs/GaAs laser diode bars analyzed by the transient thermal technique," *Solid-State Electronics,* vol. 79, pp. 192-195, 2013.

[57] P. Wen, D. Li, S. Zhang, J. Liu, L. Zhang, K. Zhou, M. Feng, Z. Li, A. Tian, and H. Yang, "High accuracy thermal resistance measurement in GaN/InGaN laser diodes," *Solid-State Electronics,* vol. 106, pp. 50-53, 2015.

[58] Y. G. Xi, T. Gessmann, J. Q. Xi, J. K. Kim, J. M. Shah, E. F. Schubert, A. J. Fischer, M. H. Crawford, K. H. A. Bogart, and A. A. Allerman, "Junction temperature in ultraviolet light-emitting diodes," *Japanese Journal of Applied Physics Part 1-Regular Papers Brief Communications & Review Papers,* vol. 44, pp. 7260-7266, 2005.

[59] S. Todoroki, M. Sawai, and K. Aiki, "Temperature distribution along the striped active region in high-power GaAlAs visible lasers," *Journal of Applied Physics,* vol. 58, pp. 1124-1128, 1985.

[60] K. Takahashi, D. Matsuoka, H. Harima, K. Kisoda, Y. Tsuda, T. Yuasa, and M. Taneya, "Temperature measurement of GaN-based blue-violet laser diodes in operation by Raman microprobe," *physica status solidi (c),* vol. 4, pp. 2802-2805, 2007.

[61] M. Horiuchi, Y. Yamagata, S.-i. Tsutsumi, K. Tomita, and Y. Manabe, "Development of junction temperature estimation system for light-emitting LED using pulsed-laser Raman scattering," *Journal of Solid State Lighting,* vol. 2, pp. 1-7, 2015.

[62] Y. Xi and E. F. Schubert, "Junction temperature measurement in GaN ultraviolet light-emitting diodes using diode forward voltage method," *Applied Physics Letters,* vol. 85, pp. 2163-2165, 2004.

[63] Y. Xi, J. Q. Xi, T. Gessmann, J. M. Shah, J. K. Kim, E. F. Schubert, A. J. Fischer, M. H. Crawford, K. H. A. Bogart, and A. A. Allerman, "Junction and carrier temperature measurements in deep-ultraviolet light-emitting diodes using three different methods," *Applied Physics Letters,* vol. 86, pp. 031907-1-3, 2005.

[64] Q. Chen, X. Luo, S. Zhou, and S. Liu, "Dynamic junction temperature measurement for high power light emitting diodes," *The Review of scientific instruments,* vol. 82, pp. 084904-1-7, 2011.

[65] D.-S. Kim, B. Han, and A. Bar-Cohen, "Characterization of Die-Attach Thermal Interface of High-Power Light-Emitting Diodes: An Inverse Approach," *IEEE Transactions on Components, Packaging and Manufacturing Technology,* vol. 5, pp. 1635-1643, 2015.

[66] D.-S. Kim and B. Han, "Effect of junction temperature on heat dissipation of high power light emitting diodes," *Journal of Applied Physics,* vol. 119, pp. 125104-1-8, 2016.

[67] W. J. Hwang, T. H. Lee, J. H. Choi, H. K. Kim, O. H. Nam, Y. J. Park, and M. W. Shin, "Thermal investigation of GaN-Based laser diode package," *IEEE Transactions on Components and Packaging Technologies,* vol. 30, pp. 637-642, 2007.

[68] A. Poppe, "A step forward in multi-domain modeling of power LEDs," in *Semiconductor Thermal Measurement and Management Symposium (SEMI-THERM), 2012 28th Annual IEEE*, pp. 325-330, 2012.

[69] B.-M. Song, B. Han, A. Bar-Cohen, R. Sharma, and M. Arik, "Hierarchical Life Prediction Model for Actively Cooled LED-Based Luminaire," *IEEE Transactions on Components and Packaging Technologies,* vol. 33, pp. 728-737, 2010.

[70] Y. S. Muzychka, J. R. Culham, and M. M. Yovanovich, "Thermal Spreading Resistance of Eccentric Heat Sources on Rectangular Flux Channels," *Journal of Electronic Packaging,* vol. 125, pp. 178-185, 2003.

[71] R. B. Ross, *Metallic Materials Specification Handbook*, 4th ed. London: Chapman & Hall, 1992.

[72] M. W. Shin and J. P. Kim, *Introduction to LED Packaging Technology*. Seoul: Bookshill, 2008.

[73] J. R. Davis, *Metals Handbook*, 10th ed. vol. 2: ASM International, 1990.

[74] C. Qian, "Thermal Management of High-power White LED Package," in *Electronic Packaging Technology, ICEPT. 8th International Conference on*, pp. 1-5, 2007.

[75] A. Nayer, *The Metals Databook*. New York: McGraw-Hill, 1997.

[76] D. R. Lide, *CRC Handbook of Chemistry and Physics*, 80th ed. Boca Raton: CRC Press, 1999.

[77] J.-M. Kang, J.-W. Kim, J.-H. Choi, D.-H. Kim, and H.-K. Kwon, "Life-time estimation of high-power blue light-emitting diode chips," *Microelectronics Reliability,* vol. 49, pp. 1231-1235, 2009.

[78] M. Meneghini, A. Tazzoli, G. Mura, G. Meneghesso, and E. Zanoni, "A Review on the Physical Mechanisms That Limit the Reliability of GaN-Based LEDs," *IEEE Transactions on Electron Devices,* vol. 57, pp. 108-118, 2010.

[79] E. Jung, J. H. Ryu, C. H. Hong, and H. Kim, "Optical Degradation of Phosphor-Converted White GaN-Based Light-Emitting Diodes under Electro-Thermal Stress," *Journal of The Electrochemical Society,* vol. 158, pp. H132-H136, 2011.

[80] J.-S. Wang, C.-C. Tsai, J.-S. Liou, W.-C. Cheng, S.-Y. Huang, G.-H. Chang, and W.-H. Cheng, "Mean-time-to-failure evaluations of encapsulation materials for LED package in accelerated thermal tests," *Microelectronics Reliability,* vol. 52, pp. 813-817, 2012.

[81] M. Meneghini, M. Dal Lago, N. Trivellin, G. Mura, M. Vanzi, G. Meneghesso, and E. Zanoni, "Chip and package-related degradation of high power white LEDs," *Microelectronics Reliability,* vol. 52, pp. 804-812, 2012.

[82] B.-M. Song, B. Han, and J.-H. Lee, "Optimum design domain of LED-based solid state lighting considering cost, energy consumption and reliability," *Microelectronics Reliability,* vol. 53, pp. 435-442, 2013.

[83] J. Liu, W. S. Tam, H. Wong, and V. Filip, "Temperature-dependent light-emitting characteristics of InGaN/GaN diodes," *Microelectronics Reliability,* vol. 49, pp. 38-41, 2009.

[84] S. Chhajed, J. Cho, E. F. Schubert, J. K. Kim, D. D. Koleske, and M. H. Crawford, "Temperature-dependent light-output characteristics of GaInN light-emitting diodes with different dislocation densities," *Physica Status Solidi a-Applications and Materials Science,* vol. 208, pp. 947-950, 2011.

[85] A. Keppens, W. R. Ryckaert, G. Deconinck, and P. Hanselaer, "Modeling high power light-emitting diode spectra and their variation with junction temperature," *Journal of Applied Physics,* vol. 108, pp. 043104-1-7, 2010.

[86] J. Q. Xi, H. Luo, A. J. Pasquale, J. K. Kim, and E. F. Schubert, "Enhanced light extraction in GaInN light-emitting diode with pyramid reflector," *IEEE Photonics Technology Letters,* vol. 18, pp. 2347-2349, 2006.

[87] M. Ma, F. W. Mont, X. Yan, J. Cho, E. F. Schubert, G. B. Kim, and C. Sone, "Effects of the refractive index of the encapsulant on the light-extraction efficiency of light-emitting diodes," *Optics Express,* vol. 19, pp. A1135-A1140, 2011.

[88] Y. C. Shen, G. O. Mueller, S. Watanabe, N. F. Gardner, A. Munkholm, and M. R. Krames, "Auger recombination in InGaN measured by photoluminescence," *Applied Physics Letters,* vol. 91, pp. 141101-1-3, 2007.

[89] M. Zhang, P. Bhattacharya, J. Singh, and J. Hinckley, "Direct measurement of auger recombination in In0.1Ga0.9N/GaN quantum wells and its impact on the efficiency of In0.1Ga0.9N/GaN multiple quantum well light emitting diodes," *Applied Physics Letters,* vol. 95, pp. 201108-1-3, 2009.

[90] S. Chhajed, Y. Xi, Y. L. Li, T. Gessmann, and E. F. Schubert, "Influence of junction temperature on chromaticity and color-rendering properties of trichromatic white-light sources based on light-emitting diodes," *Journal of Applied Physics,* vol. 97, pp. 054506-1-8, 2005.

[91] M. Glavanovics and H. Zitta, "Thermal destruction testing: An indirect approach to a simple dynamic thermal model of smart power switches," in *Proceedings of the 27th European Solid-State Circuits Conference*, pp. 221-224, 2001.

[92] H. Pape, D. Schweitzer, L. Chen, R. Kutscherauer, and M. Walder, "Development of a standard for transient measurement of junction-to-case thermal resistance," *Microelectronics Reliability,* vol. 52, pp. 1272-1278, 2012.

[93] F. Daiminger, M. Gruber, C. Dendorfer, and T. Zahner, "Experimental investigations on the offset correction of transient cooling curves of light emitting diodes based on JESD51-14 and simple semi-empirical approximations," *Microelectronics Journal,* vol. 46, pp. 1208-1215, 2015.

[94] W. M. Yen, S. Shionoya, and H. Yamamoto, *Phosphor Handbook*, 2nd ed. Boca Raton: CRC/Taylor and Francis, 2006.

[95] R. Hu and X. Luo, "A Model for Calculating the Bidirectional Scattering Properties of Phosphor Layer in White Light-Emitting Diodes," *Lightwave Technology, Journal of,* vol. 30, pp. 3376-3380, 2012.

[96] X. Luo and R. Hu, "Calculation of the phosphor heat generation in phosphor-converted light-emitting diodes," *International Journal of Heat and Mass Transfer,* vol. 75, pp. 213-217, 2014.

[97] R. J. Xie, N. Hirosaki, N. Kimura, K. Sakuma, and M. Mitomo, "2-phosphor-converted white light-emitting diodes using oxynitride/nitride phosphors," *Applied Physics Letters,* vol. 90, pp. 191101-1-3, 2007.

[98] V. Bachmann, C. Ronda, and A. Meijerink, "Temperature Quenching of Yellow Ce3+ Luminescence in YAG:Ce," *Chemistry of Materials,* vol. 21, pp. 2077-2084, 2009.

[99] D. Lisak, D. T. Cassidy, and A. H. Moore, "Bonding stress and reliability of high power GaAs-based lasers," *IEEE Transactions on Components and Packaging Technologies,* vol. 24, pp. 92-98, 2001.

[100] G. Jiang, L. Diao, and K. Kuang, *Advanced Thermal Management Materials*. New York: Springer, 2013.

[101] R. J. Quagan, "Laser Diode Heat Spreaders," Ion Beam Milling, Inc.

[102] http://www.dilas.com/.

[103] P. Perlin, M. Osiński, P. G. Eliseev, V. A. Smagley, J. Mu, M. Banas, and P. Sartori, "Low-temperature study of current and electroluminescence in InGaN/AlGaN/GaN double-heterostructure blue light-emitting diodes," *Applied Physics Letters,* vol. 69, pp. 1680-1682, 1996.

[104] S. Chhajed, Y. Xi, T. Gessmann, J.-Q. Xi, J. M. Shah, J. K. Kim, and E. F. Schubert, "Junction temperature in light-emitting diodes assessed by different methods," in *Proc. SPIE*, pp. 16-24, 2005.

[105] J. Bird, *Electrical Circuit Theory and Technology*. New York: Routledge, 2010.

[106] K. S. S. Kumar, *Electric Circuit Analysis*. New Delhi: Pearson, 2013.

[107] R. O. Carlson, G. A. Slack, and S. J. Silverman, "Thermal Conductivity of GaAs and GaAs1−xPx Laser Semiconductors," *Journal of Applied Physics,* vol. 36, pp. 505-507, 1965.

[108] E. Suhir, Y. C. Lee, and C. P. Wong, *Micro- and Opto-Electronic Materials and Structures: Physics, Mechanics, Design, Reliability, Packaging: Volume I Materials Physics - Materials Mechanics. Volume II Physical Design - Reliability and Packaging*: Springer US, 2007.

[109] J. W. Orton and T. Foxon, *Molecular Beam Epitaxy: A Short History*: Oxford University Press, 2015.

[110] P. A. Crump, M. Grimshaw, J. Wang, W. Dong, S. Zhang, S. Das, J. Farmer, M. DeVito, L. S. Meng, and J. K. Brasseur, "85% Power Conversion Efficiency 975-nm Broad Area Diode Lasers at - 50°C, 76 % at 10°C," in *Conference on Lasers and Electro-Optics/Quantum Electronics and Laser Science Conference and Photonic Applications Systems Technologies*, Long Beach, California, p. JWB24, 2006.

[111] L. Fan, C. Cao, G. Thaler, D. Nonnemacher, F. Lapinski, I. Ai, B. Caliva, S. Das, R. Walker, L. Zeng, M. McElhinney, and P. Thiagarajan, "Reliable high-power long-pulse 8XX-nm diode laser bars and arrays operating at high temperature," pp. 791805-1-7, 2011.

[112] M. H. Hu, X. Liu, and C.-E. Zah, "Transient and static thermal behavior of high-power single-mode semiconductor lasers," pp. 32-36, 2002.

[113] G. Treusch, R. Srinivasan, D. Brown, R. Miller, and J. Harrison, "Reliability of water-cooled high-power diode laser modules," in *Proc. SPIE 5711, High-Power Diode Laser Technology and Applications III*, San Jose, CA, pp. 132-141, 2005.

[114] R. Feeler, J. Junghans, G. Kemner, and E. Stephens, "Next-generation microchannel coolers," in *Proc. SPIE 6876, High-Power Diode Laser Technology and Applications VI*, San Jose, CA, pp. 687608-1-8, 2008.

[115] B.-M. Song and B. Han, "Spectral power distribution deconvolution scheme for phosphor-converted white light-emitting diode using multiple Gaussian functions," *Applied Optics,* vol. 52, pp. 1016-1024, 2013.

[116] B. Han, Y. Guo, C. K. Lim, and D. Caletka, "Verification of numerical models used in microelectronics packaging design by interferometric displacement measurement methods," *Journal of Electronic Packaging,* vol. 118, pp. 157-163, 1996.